

CFD Modeling of the Solar Two Central Tower System Receiver

BY

SIMONE PASTURA

Bachelor degree in Energy Engineering, Politecnico di Torino, Turin, Italy, 2015

Master of Science in Energy and Nuclear Engineering, Politecnico di Torino, Turin, Italy, 2017

THESIS

Submitted as partial fulfillment of the requirements for
the degree of Master of Science in Mechanical Engineering
in the Graduate College of the University of Illinois at Chicago, 2018

Chicago, Illinois

Defense Committee:

Roberto Paoli, Chair and Advisor

William Ryan

Michael Scott

Roberto Zanino, Politecnico di Torino

DEDICATION

*To my father, my mother and my brother,
for always loving, supporting and believing in
me.*

*To my love, Ludovica, for always being my
strength and making my life unbelievably
beautiful.*

ACKNOWLEDGEMENTS

Here I am, at the end of this thesis and of these beautiful five years within the Politecnico di Torino, during which I believe to be grown both in my academic path and, above all, as a person.

I think it is deserved to thank all the people who have been both physically and mentally by my side throughout this entire experience, contributing to who I am today, recognizing that this is not an end point, but only a new start for something bigger.

First of all, I want to thank God, for every single moment of this wonderful life.

This entire work would have not been possible without my supervisors, professors Roberto Zanino and Laura Savoldi, which gave me the possibility to deepen my CFD knowledge and to improve soft skills, such as critical observation and problem solving, fundamental for the career after university. I want to thank them for their availability and patience shown to me during this year, both from Chicago and from Turin.

Likewise, I want to thank professor Paoli, visiting research assistant professor at University of Illinois at Chicago, which intently followed me during my stay at Chicago, this year. He gave me the chance to work by his side, not only because of this thesis, allowing me to learn more than expected.

I cannot forget to thank the PhD students of NEMO group, Roberto, Andrea B., Andrea Z., Mattia, which have been a fundamental help for me and for the conclusion of the thesis.

Now it is the moment that I thank my parents, which have done so much for me, above all allowing me the experience to study in Turin during these years, and to study abroad, in Chicago. This can be only a little acknowledgment towards them.

I want to thank my father, because he has always been present following me step by step in these years, becoming for me a life example.

I want to thank my mother, because she always showed a blind and without uncertainties trust, driving me along my path and making me believing in myself.

I thank my brother, my little adventures companion since I was child, because he always showed his concern and attention towards me, and because I know that I can always count on him.

I want to thank my grandmother, Maria, because she always had me in his mind, praying for me and because she has been like a second mother.

A special thought to the other grandmother Pastura that, even if she is not here, she is in my heart anyway.

General thanks go to my entire family, for his support and for always being close to me however.

I thank my girlfriend, Ludovica, for being by my side from many years sharing both success and failures and, above all, for having sustained me in this last stressful period, with love, patience and trust. I want to thank her for being here, today, to celebrate this important goal, this victory... which is not only mine, but ours!

How to forget all my classmates, which unburdened me from university pains, and have given me wonderful memories that I will always bring within: special thanks go to Carla, Vincenzo, Alberto e Francesco, friends first of all. I hope these friendships will last.

I have always lived at the merit-based university college “R. Einaudi”, in Turin, and there I found a second family: I spent days and nights with the house mates of my floor, creating such a beautiful atmosphere and sharing every kind of experience. I found a treasure, a treasure that I will take care of. Personal thanks go to Umberto, Martina A., Martina D., and Elvira, with which I started my life within the college.

Every time that I come back home, in Sicily, I had a lot of friends which were always ready to welcome me with open arms and to make me feel like I never went away: I want to thank all of them for this, and for their continuous support. In a special way, Giancarlo and Andrearosa.

During the time spent in Chicago, I have been surrounded by friends that shared with me this incredible experience and made me feel less the distance from my country. For this I want to thank the Italian group, made up of Antonio, Alfredo, Marco, Enrico, Chiara M., Chiara F. and Martina, then I want thank Unmeelan, who joined us, revealing himself an awesome friend, such as Naveen and Glenn, which welcome me in the UIC dorm, sharing with them a lot of activities and dreams. I hope our paths will cross each other again.

SP

TABLE OF CONTENTS

<u>CHAPTER</u>	<u>PAGE</u>
1. INTRODUCTION.....	1
1.1 Concentrated Solar Power (CSP)	1
1.2 Central tower systems	3
1.2.1 Heliostat field	3
1.2.2 Receiver technology	7
1.3 The Solar Two case	10
1.3.1 Receiver.....	11
1.4 Aim of the thesis	15
2. MODEL DESCRIPTION.....	18
2.1 Physics of the problem	20
2.1.1 Flow regime	20
2.2 The STARCCM+ code.....	23
2.3 Discretization scheme and solver	24
3. TWO-DIMENSIONAL STUDY	28
3.1 Computational domain	28
3.2 Initial conditions and boundary conditions	29
3.3 Mesh.....	29
3.4 Circular cylinder.....	32
3.4.1 Verification	32
3.5 Polygonal cylinder.....	40
3.6 Benchmark	42
3.7 Validation.....	43
4. THREE-DIMENSIONAL STUDY	45
4.1 Computational domain	45
4.2 Initial conditions and boundary conditions	46
4.2.1 Air	46
4.2.2 Receiver.....	47
4.3 Mesh.....	47
4.3.1 Air	47
4.3.2 Receiver.....	48
4.4 Air.....	50

TABLE OF CONTENTS (continued)

<u>CHAPTER</u>	<u>PAGE</u>
4.4.1 Verification	50
4.4.2 Benchmark and validation.....	55
4.5 Receiver.....	57
4.5.1 Verification	57
4.6 Case study	59
4.6.1 Scenario #1	61
4.6.2 Scenario #2.....	64
4.7 Results.....	66
5. CONCLUSIONS AND PERSPECTIVE.....	70
APPENDICES	71
REFERENCES	84

LIST OF TABLES

<u>TABLE</u>	<u>PAGE</u>
I. TECHNICAL FEATURES OF THE SOLAR TWO RECEIVER [2]	13
II. SELECTED SCENARIOS FOR CFD MODELLING	15
III. INITIAL SPECIFICATIONS FOR THE EXTERNAL FLOW (WITH CIRCULAR CYLINDER) 2-D MESH.....	32
IV. FINAL SPECIFICATIONS FOR THE EXTERNAL FLOW (WITH CIRCULAR CYLINDER) 2-D MESH.....	38
V. SPECIFICATIONS FOR THE EXTERNAL FLOW (WITH POLYGONAL CYLINDER) 2-D MESH	40
VI. INITIAL SPECIFICATIONS FOR THE EXTERNAL FLOW (WITH POLYGONAL CYLINDER) 3-D MESH.....	48
VII. INITIAL SPECIFICATIONS FOR THE INTERNAL FLOW 3-D MESH.....	48
VIII.FINAL SPECIFICATIONS FOR THE EXTERNAL FLOW (WITH POLYGONAL CYLINDER) 3-D MESH.....	54
IX. INCIDENT RADIATIVE POWER ON RECEIVER SURFACE.....	59
X. RADIATIVE PROPERTIES OF BLACK PYROMARK, EXTERNAL RECEIVER PAINT	61

LIST OF FIGURES

<u>FIGURE</u>	<u>PAGE</u>
1. CSP technologies	2
2. Example of canted-glass mirror heliostat [25]	3
3. Example of stretched-membrane focused and non-focused heliostat [26]	4
4. Example of flat, multiple mirror heliostat [27]	4
5. Example of hexagonal-shaped mirrors heliostat [28]	5
6. Example of solar field on the polar side of the tower [29].....	6
7. Example of surround solar field [30]	6
8. Example of direct absorption receiver – falling particle [31]	7
9. Example of external tube receiver [32]	8
10. Example of cavity receiver [33]	8
11. Example of pressured, volumetric air receiver [34].....	9
12. Photograph of Solar Two plant in operation [2].....	10
13. Sketch of a molten salt power plant [2]	11
14. (a) Solar Two receiver, (b) Detail of one of the 24 panels of Solar Two receiver with 32 tubes. [4].....	12
15. CFD model of the Solar Two receiver	18
16. Simplified geometry of the receiver, with labels about orientation [4]	19
17. Thermal circuits map of the receiver.....	19
18. Regimes of fluid flow across a smooth cylinder [35]	21
19. (a) Boundary layer and its separation location (b) typical boundary layer velocity profiles at various locations on the cylinder [6].....	22
20. Comparison of residuals' plot, where 'Sdr' is the Specific dissipation rate and 'Tke' is the Total kinetic energy. (a) Steady-state simulation (b) Unsteady-state simulation.....	24
21. Comparison of drag coefficient profiles. (a) Steady-state simulation (b) Unsteady-state simulation	25
22. Screenshots of 2-dimensional, converged flow field. (a) Steady state, pressure field (at 18000 th iteration) (b) Unsteady state, pressure field (at 1.6 s) (c) Steady state, velocity field (at 18000 th iteration) (d) Unsteady state, velocity field (at 1.6 s)	26
23. Computational domain	28
24. Air, 2-dimensional, initial mesh. (a) Whole domain, (b) Zoom on the two volumetric control regions, (c) Zoom on the prism layers region	30
25. Detail of the 2-dimensional turbulent viscosity field within the prism layer region.....	31
26. Wall- y^+	31
27. Air, 2-dimensional mesh quality measurements. (a) Skewness angle (b) Face validity (c) Volume change (d) Chevron quality indicator	34
28. 2-dimensional, hydraulic simulation's monitors. (a) Residuals (b) Drag coefficient	35
29. Air, 2-dimensional grid independence study (a) # of layers (b) base size	36
30. 2-dimensional, external flow, time independence study	37
31. 2-dimensional, circular receiver flow field. (a) (Gauge) pressure field at last time-step, (b) Velocity field at last time-step, (c) Drag coefficient	39

LIST OF FIGURES (continued)

<u>FIGURE</u>	<u>PAGE</u>
32. 2-dimensional, circular receiver, time-step independence studies for different Re. (a) Re = 1.05E+06 (b) Re = 4.4E+05 (c) Re = 1.0E+05	40
33. 2-dimensional, polygonal receiver flow field. (a) (Gauge) pressure field at last time-step, (b) Velocity field at last time-step, (c) Drag coefficient	41
34. Drag coefficient as function of Reynolds number, for circular and different n-sided polygonal cylinder (adapted from [11])	42
35. Benchmark of 2-dimensional, circular cylinder results (adapted from [16])	43
36. Validation of 2-dimensional results (adapted from [16])	44
37. Air, 3-dimensional, computational domain. (a) xy plane (b) xz plane	45
38. How pressure is adjusted on the faces of pressure outlet boundary [12]	46
39. Initial receiver mesh. (a) Whole receiver, (b) Zoom on a single panel, (c) Zoom on the inlet/outlet of the panel	49
40. Air, 3-dimensional mesh quality measurements. (a) Skewness angle, (b) Face validity, (c) Volume change, (d) Chevron quality indicator (e) Cell quality	51
41. Air, 3-dimensional grid independence study – # of prism layers	52
42. External flow field details (a) Wall- y^+ (b) Detail of the turbulent viscosity field within the prism layer region	53
43. 3-dimensional velocity field of converged external flow. (a) xy plane (b) xz plane	55
44. Benchmark of 3-dimensional results – only hydraulic, external flow (adapted from [15])	56
45. Validation of 3-dimensional results – only hydraulic, external flow (adapted from [38])	56
46. Receiver mesh quality measurements. (a) Skewness angle, (b) Face validity, (c) Volume change, (d) Chevron quality indicator (e) Cell quality	58
47. Receiver grid independence study – base size. (a) x-direction (b) y-direction (c) z-direction	59
48. Distribution of the radiative load (kW/m^2) on the receiver panels. (a) SCENARIO #1 (b) SCENARIO #2	60
49. SCENARIO #1, air velocity flow field. (a) equatorial plane (b) vertical west-east plane, passing through the receiver center	61
50. SCENARIO #1, air temperature map. (a) equatorial plane (b) vertical west-east plane, passing through the receiver center	62
51. SCENARIO #1, receiver temperature map	63
52. SCENARIO #2, air velocity flow field. (a) equatorial plane (b) vertical west-east plane, passing through the receiver center	64
53. SCENARIO #2, air temperature map. (a) equatorial plane (b) vertical west-east plane, passing through the receiver center	65
54. SCENARIO #2, receiver temperature map	66
55. SCENARIO #1. (a) Experimental total heat loss, compared to total heat loss computed (b) Computed convective heat loss compared to prediction from correlations SCENARIO #2. (c) Experimental total heat loss, compared to total heat loss computed (d) Computed convective heat loss compared to prediction from correlations	68

LIST OF FIGURES (continued)

<u>FIGURE</u>	<u>PAGE</u>
56. (a) Drag coefficient as a function of Reynolds number for a 2-dimensional, smooth circular cylinder (adapted from [6]), (b) Experimental references for drag coefficient in the turbulent region (adapted from [16]).....	73
57. Interactions of radiation with semitransparent medium [37]	76
58. View factor associated with radiation exchange between elemental surfaces of area dA_i and dA_j [36]	77

LIST OF SYMBOLS AND ACRONYMS

δ	Boundary layer thickness
μ	Dynamic viscosity
ν	Kinematic viscosity
ρ	Density
c_p	Specific heat at constant pressure
h	Enthalpy (per unit mass)
k	Thermal conductivity
m	Mass
\dot{m}	Mass flow rate
τ	Shear stress
τ_{ij}	Stress tensor
ε_{ij}	Strain rate tensor
\vec{g}	Acceleration of gravity
\vec{F}	Force vector
\vec{V}	Velocity vector
C_D	Drag coefficient
F_D	Drag force
D	Diameter of the cylinder
dp/dx	Pressure gradient
l	Characteristic length
A	Characteristic area
Re	Reynolds number
Gr	Grashof number
Nu	Nusselt number
Ma	Mach number
u	Velocity component in X-direction

LIST OF SYMBOLS AND ACRONYMS (continued)

u_*	Friction velocity
U_∞	Free-stream velocity
p_∞	Reference pressure
v	Velocity component in Y-direction
δ_{ij}	Kronecker delta
S_{ij}	Shear stress of the flow
T	Absolute temperature
CAD	Computer-Aided Design
CFD	Computational Fluid Dynamics
DNS	Direct Numerical Simulation
LES	Large-Eddy Simulation
RANS	Reynolds-Averaged Navier-Stokes
URANS	Unsteady Reynolds-Averaged Navier-Stokes
CSP	Concentrated Solar Power
SGS	Steam Generation System
DAPS	Dynamic Aim Processing System
DoE	Department of Energy

SUMMARY

Nowadays, CSP technologies cannot compete on price, for example, with photovoltaics (solar panels), which have been subjected to a huge growth in these last years because of the falling prices of the panels and a much smaller operating cost, as well as exceptionally subsidized, especially in our Country. Concentrated Solar Power system requires cost reduction and increased efficiency to make a breakthrough in the energy market. Paying attention to central tower systems, these ones allow higher concentrations than parabolic troughs and therefore show high potential in that perspective for future deployment. CFD modelling is a strong work tool to study geometrically complex engineering problems and, in this case, it can help in the optimization of the design of the receiver.

The development and validation of a computational fluid dynamic model of the ‘Solar Two’ central tower system receiver at Sandia National Laboratory (SNL), in Albuquerque (NM) USA, by means of the general purpose CFD software STAR-CCM+, is considered.

The verification, benchmark and validation of a purely hydraulic, external flow (air) sub-problem have been approached first (both in 2- and in 3-dimensional analysis), as well as the verification of 3-dimensional, thermal-hydraulic, internal flow (molten salts within the receiver) sub-problem, separately in two different scenarios experimentally studied at SNL.

Once the separated analyses have been completed, the coupled external/internal flow simulations of both cited scenarios have been performed: the CFD results are in agreement with those available from employed correlations for smooth cylinders (by Churchill and Achenbach) and from on-site measurements, within the corresponding error bars. The computed convective heat loss (equal to the surface integral of the heat flux from the receiver to the air, subtracted of the radiative part) at statistically stationary state are $\approx 1.5 \%$ (2.2%) of the incident power on the receiver surface, for scenario #1 (#2).

CHAPTER 1

INTRODUCTION

1.1 Concentrated Solar Power (CSP)

CSP is a technology able to generate electricity by concentrating direct solar beams through mirrors or lenses (with tracking system) onto a small area, converting this light in heat through a working fluid and coupling the latter with a conventional thermal process, by means of a heat engine (usually a steam turbine), connected to an electric power generator. Because of the use of direct solar radiation, it has one tight constrain: it has to be placed in regions with excellent solar resources, such as in the so-called world's Sun Belt; therefore, the selection of suitable sites to build CSP plants is an important aspect.

Initially introduced in large scale in the early 1980's consequently to the oil crisis in 1970's, this technology has been employed for large scale electricity production to partially replace fossil power plants, long before global warming was highlighted. The decreasing availability of fossil fuels and the increasing concern of the rising energy prices encouraged many countries to fund research and development on renewable energy, particularly on CSP.

CSP is, above all, able to provide base-load electricity even if the solar radiation is not available 24h/day: this is possible thanks to the presence of one or more heat storages. This remarkable feature allows the special renewable technology to gain importance in the current change of the energy market more and more ruled by other renewable source, for instance by photovoltaics and wind energy, whose output is yet more weather dependent.

Power plants exploiting this technology differ mainly on how sunlight is concentrated (see Fig. 1):

1. Point concentration: solar radiation concentrated on a point, with biaxial tracking system (more expensive, but more precise and effective)

- (a) Solar towers

These systems are made by a field of heliostats, which follow the Sun through a tracking system, aspiring to focus the Sun beams to the top of a tower, where a receiver is placed. This technology is the most promising for the future;

(b) Stirling dishes

These systems are made by a paraboloid surface, which reflects the Sun beams towards its geometrical focus, where a Stirling engine is placed. This technology is strongly used for relatively low power in remote places;

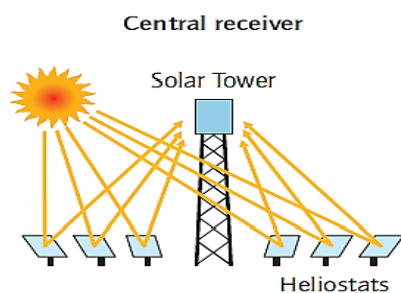
2. Line concentration: solar radiation concentrated on a line, with uniaxial tracking system (cheaper, but less accurate and effective)

(c) Parabolic troughs

These systems are made by parabolic-shape mirrors, reflecting the Sun rays onto an absorber, that is a pipe placed in the geometrical focus of the parabola, containing the heat transfer fluid. Thus, the tracking system makes the absorber and the mirrors move compactly;

(d) Linear Fresnel

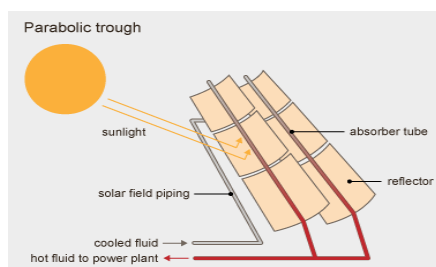
These systems are made by a set of flat mirrors pointing at one or more receivers. With respect to the previous scheme, in linear Fresnel systems only the mirrors move to track the Sun, while the absorber stays fixed.



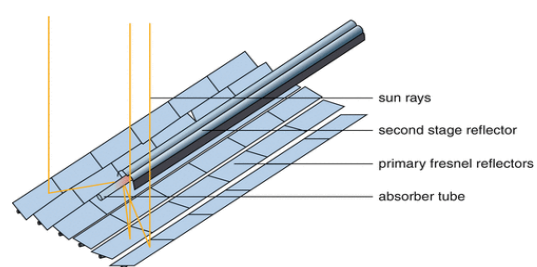
(a) Solar tower [21]



(b) Stirling dish [22]



(c) Parabolic troughs [23]



(d) Linear Fresnel [24]

Figure 1: CSP technologies

1.2 Central tower systems

A central tower system is an energy production plant made up of a considerable number of sun-tracking mirrors, whose goal is to focus highly concentrated solar irradiation on the absorber surface, i.e. the receiver surface. The receiver, located at the top of a tower, transforms the absorbed radiation into heat and transfers the heat to a working fluid, flowing within itself. Then, the thermal vector goes in a heat exchanger (that is, a boiler), making the water vaporized; soon after, the steam proceeds into the turbine, producing electricity.

Two big differentiation can be made within this class of energy production plant, considering:

- The heliostat (or solar) field
- The receiver technology

1.2.1 Heliostat field

The heliostat field is the totality of mirrors (can be many hundreds or thousands) equipped with a two-axes tracking system, useful to follow the path of the Sun over the course of the day. There are several different types of heliostat mirrors on commercial scale, changing about the shape, such as:

1. Canted-glass mirror heliostat (see Fig. 2);



Figure 2: Example of canted-glass mirror heliostat [25]

2. Stretched-membrane focused and non-focused heliostat (see Fig. 3);

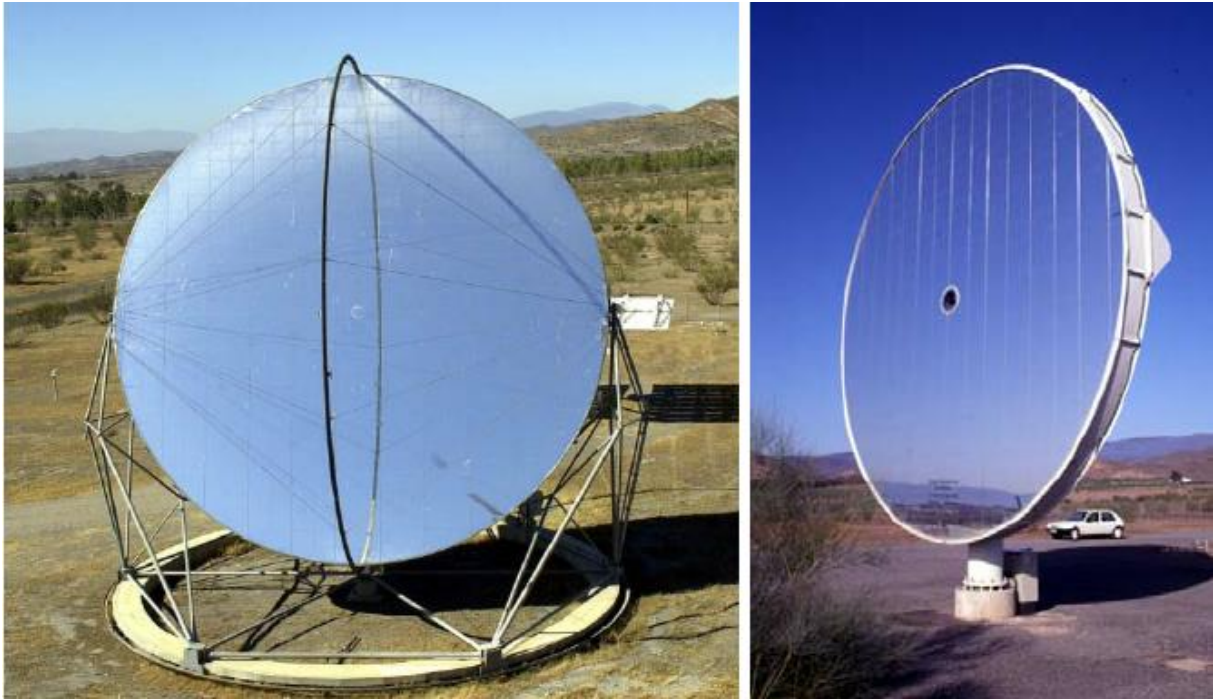


Figure 3: Example of stretched-membrane focused and non-focused heliostat [26]

3. Flat or nearly flat single or multiple mirror heliostat (see Fig. 4);



Figure 4: Example of flat, multiple mirror heliostat [27]

4. Hexagonal-shaped mirrors heliostat (see Fig. 5);



Figure 5: Example of hexagonal-shaped mirrors heliostat [28]

or about size (varying between 1 m² and 150 m²), or design tracking system, or even composition of the mirror material.

Moreover, other important difference can be made considering the heliostat field design: indeed, according to the location of the power plant on the earth, various solar field design are available to reliably produce the required power whilst keeping land usage and total costs to a minimum. Considering:

1. The southern/northern hemisphere (see Fig. 6) → the solar field must be placed to the north of the tower;
2. Latitudes close to equator (see Fig. 7) → a two-field arrangement (“surrounding field”) can be taken into account, due to the high elevation angles of the sun.



Figure 6: Example of solar field on the polar side of the tower [29]

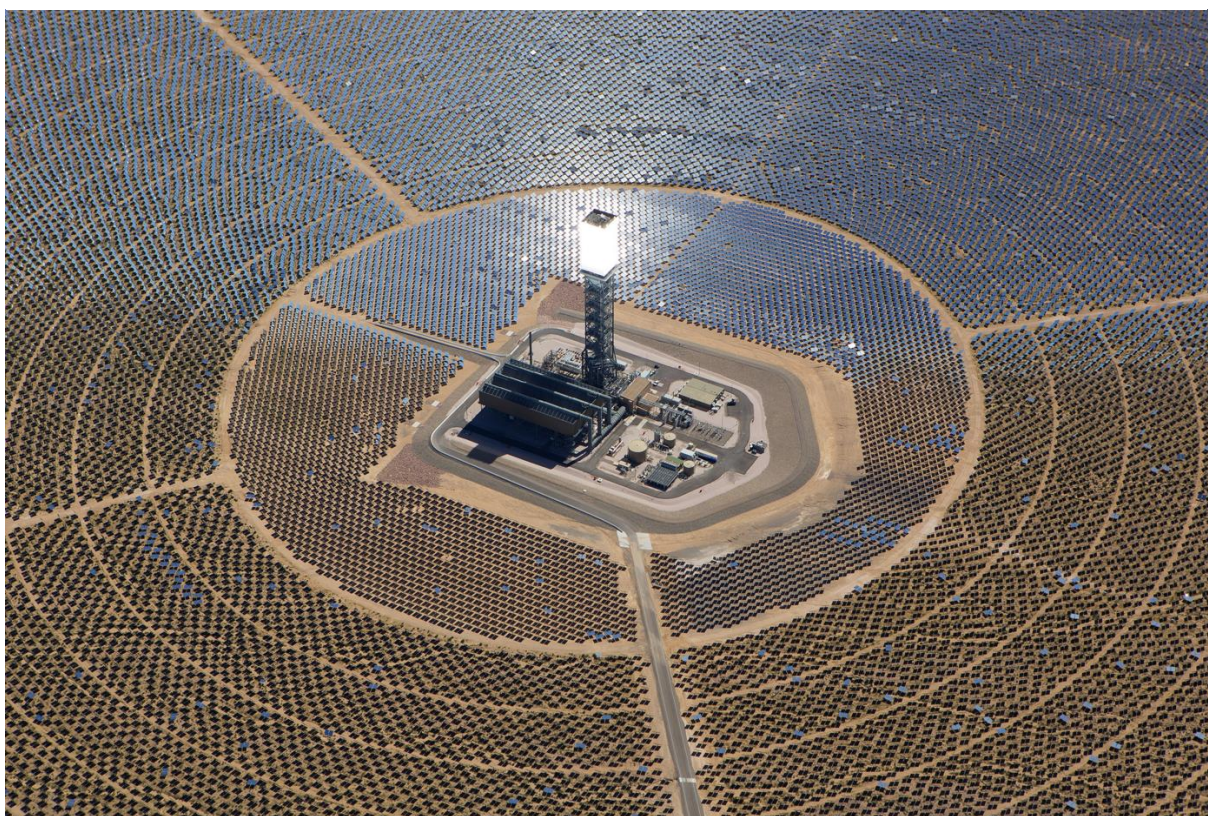


Figure 7: Example of surround solar field [30]

1.2.2 Receiver technology

A lot of kinds of receiver are found on commercial scale, but they can be summed up into 4 main classes:

1. Direct absorption receiver (see Fig. 8): the heat transfer medium (which can be falling particles or molten salt liquid film) is directly exposed to and heated by the concentrated solar irradiation;

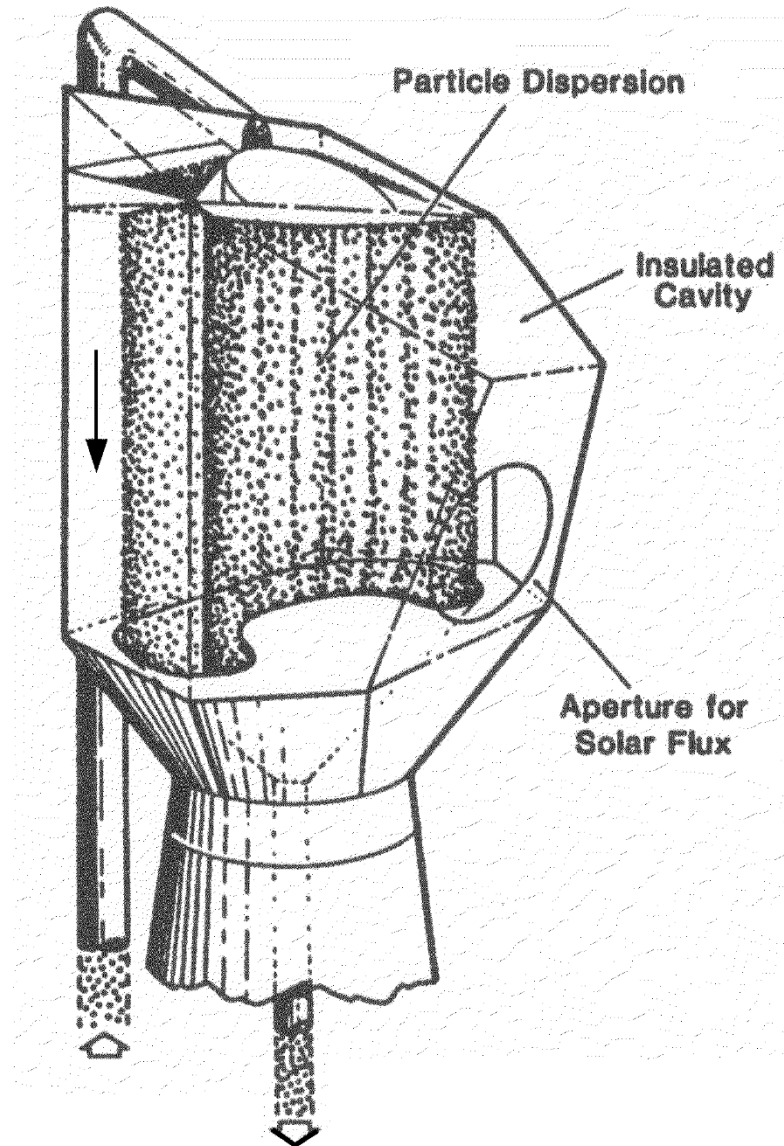


Figure 8: Example of direct absorption receiver – falling particle [31]

2. External tube receiver (see Fig. 9): the heat transfer medium (which can be molten salts, or metallic sodium, or water for direct steam generation) proceeds upwards within vertical arranged pipes;

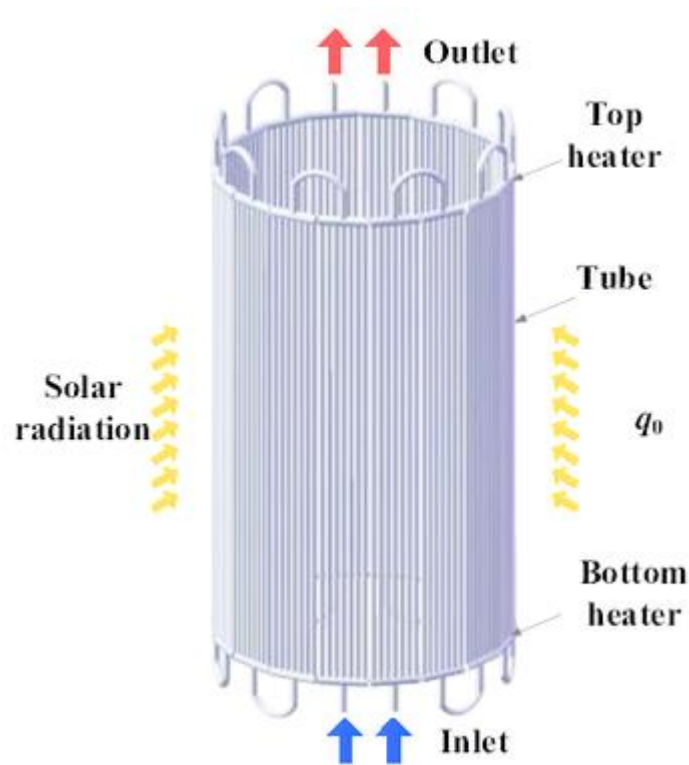


Figure 9: Example of external tube receiver [32]

3. Cavity receiver (see Fig. 10): with the idea to minimize the radiation losses, a cavity with a small opening is present within the receiver, letting the concentrated solar irradiation enter and impinge on tubes carrying the working fluid (which can be gas or molten salts);

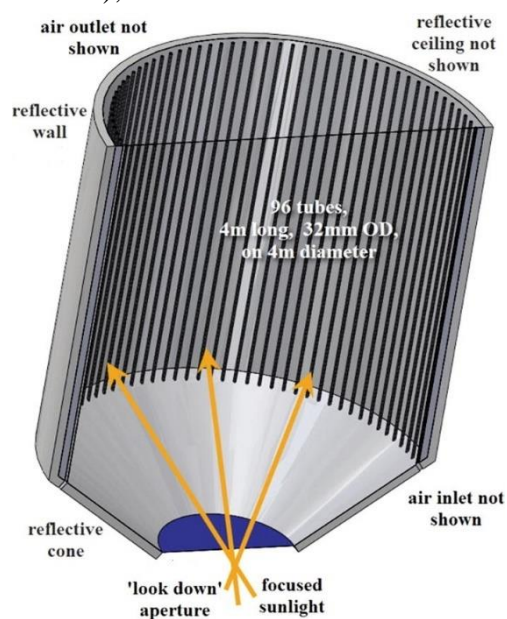


Figure 10: Example of cavity receiver [33]

4. Air receiver (see Fig. 11): it can be an open volumetric receiver, where a porous absorber material absorbs the radiation within the volume of the structure, transferring the heat to the working fluid passing through the structure itself; or it can be a pressured volumetric receiver, where a quartz window separates the absorber modules (that is a wire mesh) from the external environment, sucking in, pressurizing and heating up the air. Already enough hot, the air can be directly expanded in gas turbine.

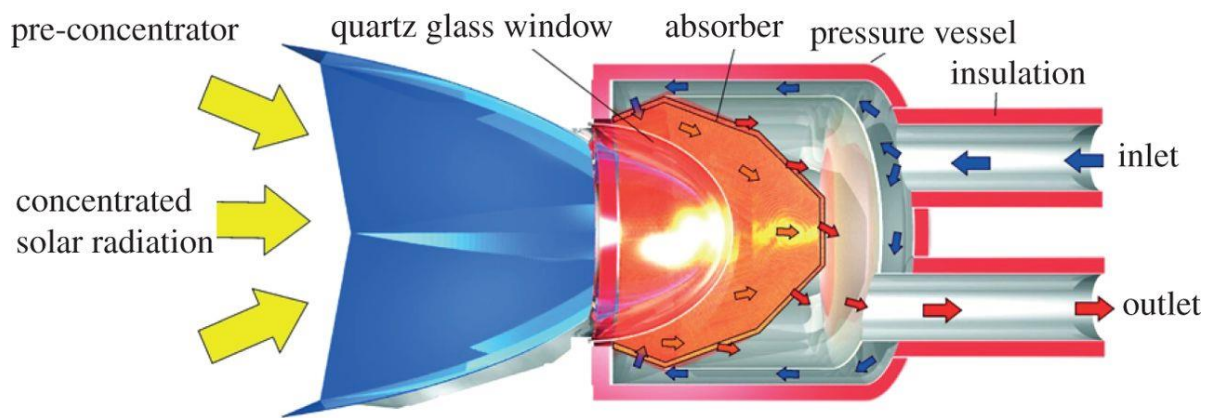


Figure 11: Example of pressured, volumetric air receiver [34]

1.3 The Solar Two case

Solar Two arose as a joined, cost-shared project between U.S. DoE few U.S. industry and utility partners: the major aim was to validate the potential of molten-salt solar tower technology on the energy market.

The Solar Two plant is located east of Barstow, California, built on a previous solar tower plant (called Solar One Pilot) through few modifications, operating from June 1996 to April 1999. Figure 12 displays a picture of the Solar Two plant.



Figure 12: Photograph of Solar Two plant in operation [2]

It was mainly made of:

- a surround solar field, with 1926 heliostats, provided of tracking systems;
- an external receiver, arranged at the top of the central tower;
- a thermal storage system, made up of two tanks (a hot one and a cold one);
- a SGS (steam generation system), made up of a U-tube, straight-shell preheater and superheater, and a kettle evaporator;
- a steam-turbine power block.

Molten nitrate salts (consisting of 60 wt% NaNO_3 and 40 wt% KNO_3) were used as primary fluid (that is directly heated) and storage media, whereas water/vapor was used as secondary fluid to produce 10 MWe by means of an ordinary Rankine turbine-generator. All power plant's parts in contact with the hot molten salts (such as pipes, vessels and valves) are

made of stainless steel, due to its strong resistance to the corrosion produced by the hot molten salts.

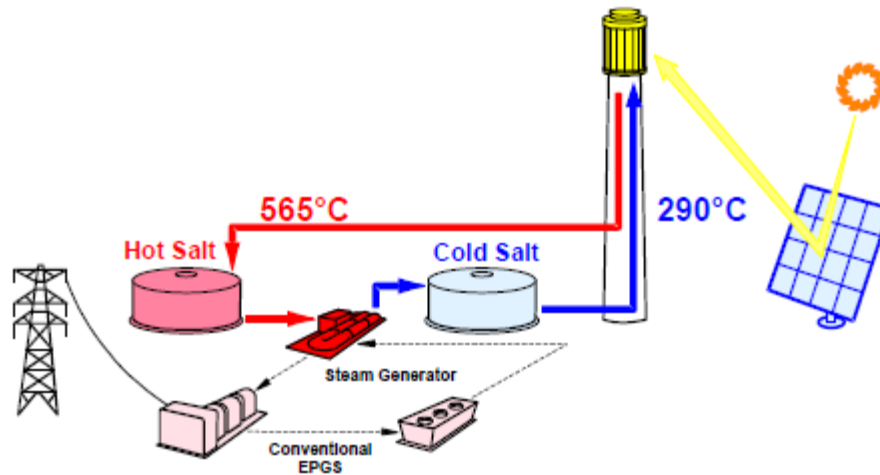


Figure 13: Sketch of a molten salt power plant [2]

It is possible to observe a schematic of the plant in the Figure 13: molten salt at 290 °C is drawn out from the cold storage to the receiver (that is, a heat exchanger) while sunlight is reflected and concentrated from the field of heliostats into the receiver. Thus, molten salt is heated up until 565 °C and, flowing back down to ground level, is kept in the hot storage. To generate electricity, molten salt is pumped from the hot storage into the SGS (so producing superheated high-pressure steam), returning to the cold storage finally; a traditional Rankine turbine-generator is then powered by the steam.

1.3.1 Receiver

The Solar Two receiver was an external cylinder. Its design absorbed power and rated average capability were 42.2 MWt and 430 kW/m², respectively. As previously mentioned, molten salt was set to be heated up from 290 °C to 565 °C by means of a specific flux distribution on the receiver surface, maintaining corrosion and strain in the receiver structures within admissible limits [1].

The structure of the receiver was made of 24 panels (see Figure 14):

- every panel was composed of 32 thin-walled tubes (316H stainless steel), with end-bends connected to manifolds on each end of the panel;
- the diameter and the wall thickness of each tube was 2.1 cm and 1.2 mm, respectively;

- each tube was externally coated with a black Pyromark® paint because of its optimal performance about robustness, thermal cycling, resistance to high temperature and absorbed percentage of the incident sunlight (around 95%);
- every end-bend and manifold were surrounded by an insulated, electrically-heated oven covers.

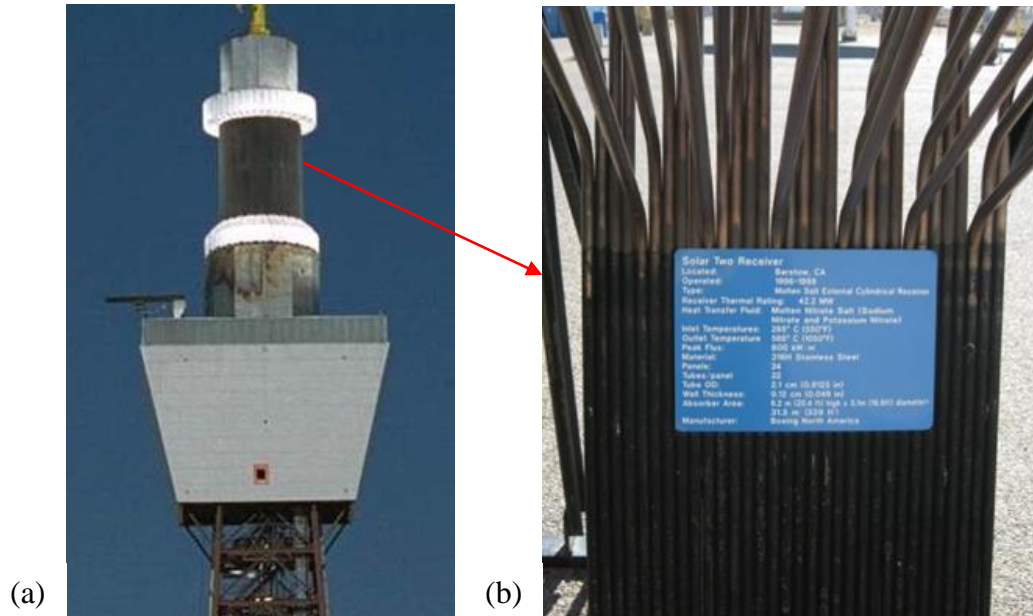


Figure 14: (a) Solar Two receiver, (b) Detail of one of the 24 panels of Solar Two receiver with 32 tubes. [4]

The characteristics of the Solar Two receiver are displayed in the Table I.

TABLE I: TECHNICAL FEATURES OF THE SOLAR TWO RECEIVER [2]

Configuration	External cylindrical receiver
Receiver thermal rating	42.2 MW
Heat transfer fluid	Molten Nitrate Salt (60% NaNO_3 AND 40 % KNO_3)
Inlet temperature	290 °C
Outlet temperature	565 °C
Peak flux	800 kW/m ²
Average flux	430 kW/m ²
Material	316H Stainless Steel
Panels	24
Flow circuits	2 (12 panels each)
Tubes/Panels	32
Tube OD	2.1 cm
Wall thickness	1.2 mm
Absorber height	6.2 m
Absorber diameter	5.1 m
Absorber area	99.3 m ²
Absorber material	Black Pyromark® Paint
Elevation above ground	76.2 m to receiver centerline
Manufacturer	Boeing North American
Dates operated	Feb 28, 1996 to April 8, 1999
Hours of operation (approximate)	1800 hours
Receiver pump type	Two 50% capacity, six-stage, vertical turbines
Receiver pump head	244 m at 1.64 m ³ /min
Receiver pump manufacturer	BW/ (IP) International, Inc.

During the design phase of the receiver, specific attention was placed on the rapidly change temperature without receiving damages: an example of this situation was a cloud passage, during which the receiver could safely vary its temperature from 565 °C to 290 °C in less than one minute [3].

Moreover, other important issue faced during the design phase was to prevent molten salt from freezing:

- during night-time and few hours prior to daily startup: electric heaters placed all along the piping, inlet/outlet vessel and valves were energized;
- during daily startup: with the sun few degrees above the horizon, a group of heliostats was designated to distribute a uniform heat flux on the surface of the receiver, preheating its surface above 230 °C, in order to fill it soon after;
- during daylight hours: having all the available heliostats focused on the receiver and the outlet temperature set to the desired one, normally 565 °C, flow control valves automatically acted modulating the flow rate;
- during daily shutdown: the heliostats were defocused from the receiver and its surface temperature fell. However, a group of heliostats was designated to maintain that temperature above 260 °C, while the receiver was drained

By means of back-wall thermocouples giving a feedback about the strength of the wind and the level of cloudiness, the Dynamic Aim Processing System (DAPS) controlled the number and aiming of the heliostats focused on the receiver, modifying the flux density consequently. During daylight hours, whereas, eight photometers, mounted around the perimeter of the receiver, recognized variations in the incident power due to cloud cover; thus, the control algorithm received those signals as inputs, modulating the control valves consequently.

1.4 Aim of the thesis

Two cases have been selected from data provided by Sandia National Laboratory (Albuquerque, NM), to analyze the receiver system and to build the CFD model. The scenarios have the following features:

TABLE II: SELECTED SCENARIOS FOR CFD MODELLING

	SCENARIO #1 (05/03/1999)	SCENARIO #2 (23/03/1999)
Free-stream air speed, [m/s]	3.0	7.9
Free-stream air temperature, [°C]	16	16
Reynolds number, [-]	~ 1.05E+06	~ 2.76E+06
External fluid-dynamic regime	Turbulent, supercritical	Turbulent, supercritical
Grashof number, [-]	8.92E12 – 2.32E13	8.92E12 – 2.32E13
Convection	8.09 – 21.04 (Natural)	1.17 – 3.05 (Mixed)
Salt flow rate, [kg/s]	40.25	31.5
Salt inlet temperature, [°C]	308	302

where the Grashof number is the dimensionless physical quantity which approximates the ratio of the buoyancy to viscous force acting on a fluid and the Reynolds number is a dimensionless group which measures the ratio of the inertial forces on an element of fluid to the viscous force on that element: if the Reynolds number is really small ($Re \ll 1$), viscous forces are dominant in the problem and it may be possible to neglect inertial forces; on the other hand, for large Reynolds numbers, viscous effects are small with respect to inertial effects and it may be possible to neglect the effect of viscosity.

They are defined as:

$$Gr_H = \frac{g\beta(T_F - T_\infty)H^3}{\nu^2} \quad (1)$$

$$Re_D = \frac{\rho V D}{\mu} = \frac{V D}{\nu} \quad (2)$$

where

- β , [1/K] is the coefficient of thermal expansion
- T_F is the film temperature of the air
- T_∞ is the bulk temperature of the air

The receiver surface temperature has been guessed a priori (a minimum of 260 °C, due to preventing salt from freezing within the receiver, and a maximum of 650 °C, around 100 °C hotter than the design output salt temperature) to have an idea about the convection type around the receiver.

Thus, considering the ratio $\frac{Gr}{Re^2}$, if:

- $\frac{Gr}{Re^2} \gg 1$: natural convection
- $\frac{Gr}{Re^2} \approx 1$: mixed convection
- $\frac{Gr}{Re^2} \ll 1$: forced convection

The Solar Two central tower system receiver was previously studied, among other authors, in [4], where the consequence of the selection of RANS type turbulence closure on the CFD estimation of convective heat losses towards the atmosphere was investigated using the commercial CFD code ANSYS FLUENT, then comparing the results with correlations and on-site measurements.

In comparison with that work, in this thesis the following new items are considered:

- unsteady analysis
- different commercial CFD code employed: STAR-CCM+ (v11.04)
- polynomial thermo-physical properties considered for both air and molten salts
- external flow assessed considering first the purely hydraulic behavior
- solar heat load applied as surface heat flux on each panel

The aim of the thesis is to develop and validate a computational fluid dynamic model (two-dimensional and three-dimensional) of the ‘Solar Two’ central tower receiver. The model will include internal flow of the salt in the external receiver piping.

The main purpose of the model is to study the fluid dynamic and thermal features of the flow with special reference to the external flow (for both scenarios), responsible for the convective losses from the receiver; in the end, a benchmark will be conducted comparing this

work with the previous cited work [4], and validation of the results about total and convective heat losses will be carried out through comparison with experimental on-site measurements [2], and experimentally based correlations found in [5] (only for scenario #1, because of lack of time).

CHAPTER 2

MODEL DESCRIPTION

For the purpose of CFD simulations, only the receiver was taken into account, neglecting all the other structures above and below it. The real receiver was approximated by an empty polyhedron with 24 sides (see Fig. 15): each panel was considered as a single flat channel of rectangular cross section approximately, thus neglecting the individual tubes since $D_{\text{tube}} \ll D_{\text{receiver}}$.

The followed criterion for the approximation was to maintain constant the molten salts flow rate:

$$(\text{Area})_{\text{tot. tubes}} = (\text{Area})_{\text{channel}} \rightarrow 32 \text{ tubes} \cdot \pi/4 \cdot D_{\text{tube ID}}^2 = \text{width}_{\text{channel}} * \text{depth}_{\text{channel}}$$
$$\rightarrow \text{depth}_{\text{channel}} \approx 1.3 \text{ cm}$$

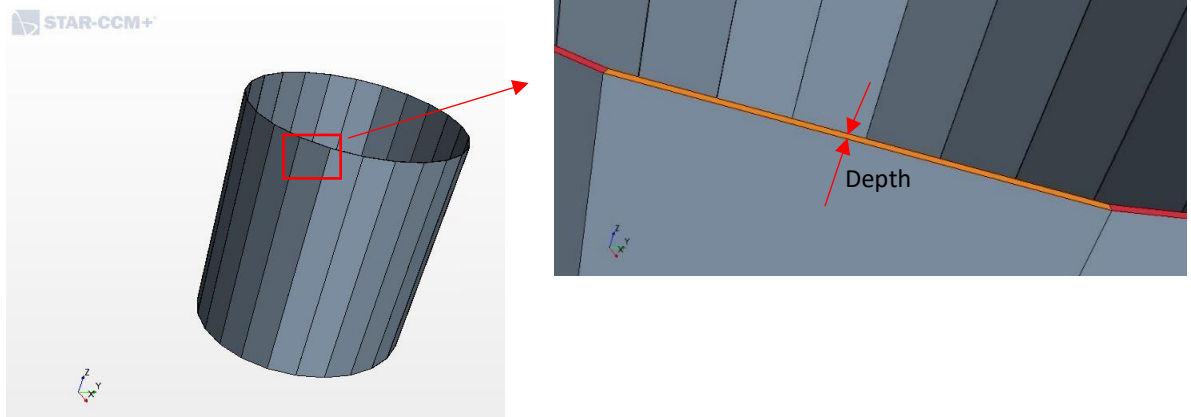


Figure 15: CFD model of the Solar Two receiver

Each panel is modeled as zero-thickness, impermeable surface, thus without thermal capacity and conducting only along the direction normal to itself.

The salt provided to the receiver was split into two circuits (each including 12 panels, see Figure 16 and Figure 17): the first stream started from the northern-most panel (W1) on the west side and proceeded west in a serpentine path from panel to panel. The second one started from the northern-most panel on the east side (E1) and proceeded east, in the same previous way. After flowing through the first six panels, both streams crossed over (W1-W6/E7-E12 and E1-E6/W7-W12) to balance energy collection variations that occurred from east to west as a function of the time of day.

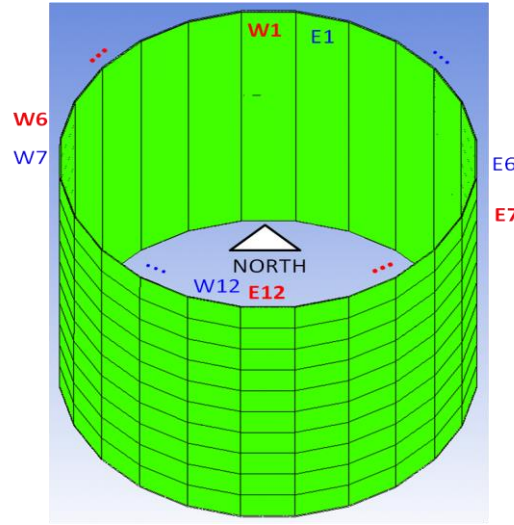


Figure 16: Simplified geometry of the receiver, with labels about orientation [4]

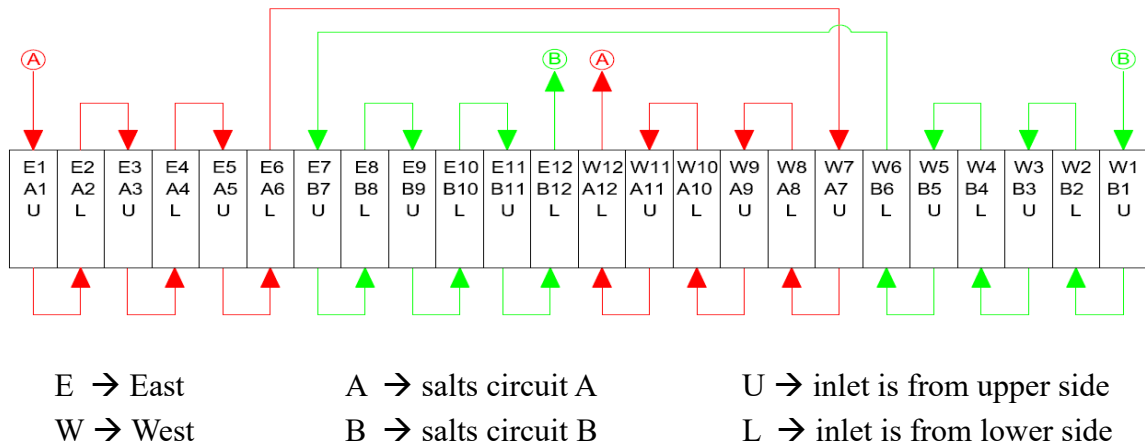


Figure 17: Thermal circuits map of the receiver

The two fluid of interest have been modelled as follow:

- Air {
- ideal gas
 - polynomial thermos-physical properties:
 - T , [K]
 - ρ , [kg/m³] = $p_{\text{atm}}/(R \cdot T)$
 - c_p , [J/kg/K] = $1042.50 - 36.60E-2 \cdot T + 9.70E-4 \cdot T^2 - 65.95E-08 \cdot T^3 + 1.67E-11 \cdot T^4$
 - k , [W/m/K] = $1.30E-2 + 9.28E-05 \cdot T - 33.01E-09 \cdot T^2 + 6.52E-12 \cdot T^3$
 - μ , [kg/m/s] = $3.83E-06 - 5.578E-08 \cdot T - 2.294E-11 \cdot T^2 - 4.935E-15 \cdot T^3$

Molten salts	{	liquid
		polynomial thermo-physical properties:
		<ul style="list-style-type: none"> • $T, [K]$ • $\rho, [kg/m^3] = 2263.70 - 63.60E-2*T$ • $c_p, [J/kg/K] = 1396 + 17.20E-2*T$ • $k, [W/m/K] = 39.11E-2 + 1.90E-4*T$ • $\mu, [kg/m/s] = 7551.48E-5 - 27.76E-5*T + 348.89E-9*T^2 - 14.74E-11*T^3$

2.1 Physics of the problem

The flow around a circular cylinder is one of the classical and well known problems in fluid dynamics: it is of considerable interest in engineering applications such as our case or, for example, in a more broadly way, a moving ship in a harbour, a bridge piers in slow currents, an island where the distribution of phytoplankton is affected by a planar vortex dynamics. The intricacy of this phenomena which follow from our study is of large interest for a lot of topics, like boundary layer instability, transition from laminar to turbulent flows strictly related to the Reynolds number, dynamics of vortex shedding and drag crisis. A fundamental aspect is to recognize which are the most important phenomena that takes place in each flow regime before approaching a CFD study. An extensive literature has been produced about this during the last century, like a general one on [6] or a more detailed one on [7].

Our study concerns turbulent flows, which exhibit the following features:

- Three-dimensional;
- Highly unsteady (even with constant imposed boundary condition);
- Highly diffusive and dissipative (i.e., ability to transport and mix fluid much more effectively than a comparable laminar flow);
- Chaotic;
- Wide range of length and time scale.

2.1.1 Flow regime

In these study cases, like a flow normal to the axis of a circular cylinder, the fluid is the air, the characteristic length is represented by the diameter of the cylinder, D , and $V=U_\infty$ is the velocity far upstream the cylinder.

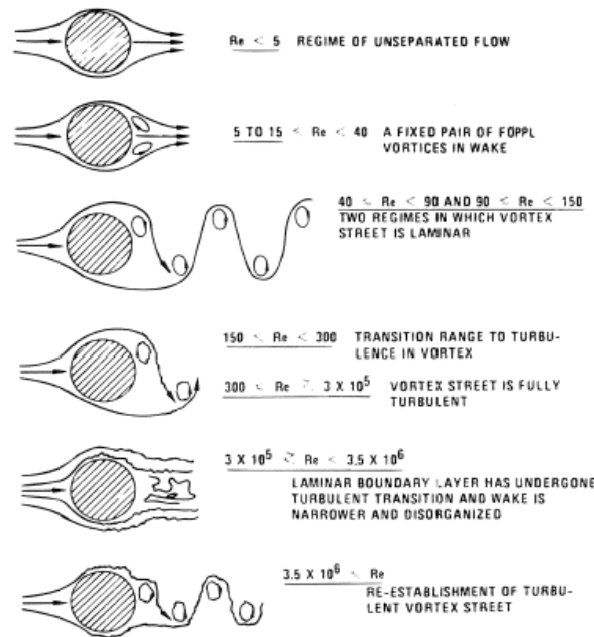
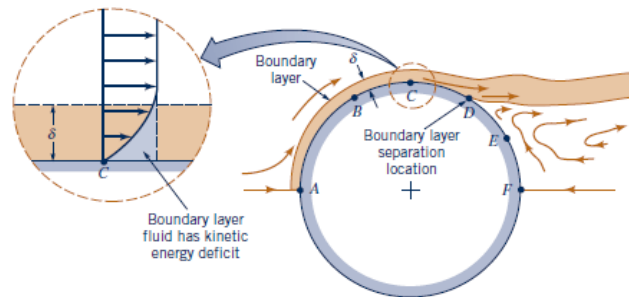


Figure 18: Regimes of fluid flow across a smooth cylinder [35]

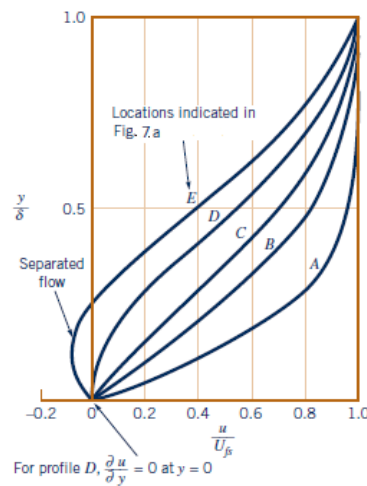
A description of flow regimes and related occurring phenomena is provided by Figure 18. Focusing the attention in the turbulent range of Re , we have:

- $150 < Re < 300$ (transition): periodic and irregular disturbances are found in the wake. Transition to turbulence occurs in the wake region and vortex shedding becomes three-dimensional;
- $300 < Re < 3 \cdot 10^5$ (laminar boundary layer): this regime is called *subcritical*, and a thin ($\delta \ll D$, see Fig. 19) boundary layer over the front portion of the cylinder remains laminar. Because of the large velocity gradients, shear stresses (and hence viscous effects) are important in this portion and in the wake. On the other hand, the fluid in the region outside of the boundary layer and the wake behaves as inviscid;
- $3 \cdot 10^5 < Re < 3.5 \cdot 10^6$: in the range of $3 \cdot 10^5 < Re < 3.5 \cdot 10^5$, the flow regime is called *critical* (or *lower transition*) flow regime, and the boundary layer becomes turbulent at the separation point (described as the location on the cylinder wall ($y=0$) where $u = v = 0$ and $\frac{\partial u}{\partial y} = 0$), but only at one side of the cylinder; whereas, it is laminar on the other side of the cylinder. In the range of $3.5 \cdot 10^5 < Re < 1.5 \cdot 10^6$, the flow regime is called *supercritical* flow regime, and the boundary layer is turbulent on both sides of the cylinder, with the transition to turbulence located somewhere between the stagnation point and the separation point. At $Re = 1.5 \cdot 10^6$, the boundary layer is completely

turbulent on one side of the cylinder and partially laminar and partially turbulent on the other side. From this point on, the flow regime is called *upper transition* flow regime, until $Re = 3.5 \cdot 10^6$;



(a)



(b)

Figure 19: (a) Boundary layer and its separation location
(b) typical boundary layer velocity profiles at various locations on the cylinder [6]

- $Re > 3.5 \cdot 10^6$ (transcritical): flow regime is called *transcritical*, and the boundary layer over the cylinder is turbulent everywhere.

2.2 The STARCCM+ code

STARCCM+ (CD-Adapco, Siemens) is a Computational tool for solving multidisciplinary problems for fluid and solid continuum mechanics. For this thesis, it will be used for computational thermo-fluid dynamic simulations of complex external and internal flow of different fluids exchanging heat.

Many flows encountered in engineering field are turbulent, and thus modeling requires careful treatment.

In the past, the first approach was to study these phenomena by means of experiments: with time, the level of needed details and accuracy increased, as did the cost, the expenses and the difficulty of making measurements. In this context, numerical methods had and (nowadays) have an important role to play. Three important categories must be cited:

1. Direct Numerical Simulation (DNS): this method solves Navier-Stokes equations, resolving all the scales of motion of the flow field. The computed flow field is equivalent to a single realization of a flow or a short-duration laboratory experiment. It is the simplest approach and, once applied, it is unrivalled in the level of detail and accuracy provided. On the other hand, it is computationally high-costly (this cost increases rapidly with the Reynolds number, approximately as Re_l^3), thus it is limited to flows of low or moderate Reynolds numbers and to geometrically simple domains;
2. Large-Eddy Simulation (LES): this method solves Navier-Stokes equations, resolving only the largest scale motions of the flow field, while modeling the small-scale motions: consequently, it is feasible to access higher Re numbers, compared to DNS. Thus, there is a smoothing with respect to the real physics, applying a filtering (a sort of convolution with weights) on the velocity field: the attention is focused on the largest vortices because they contain the highest energy, and their strength makes them more effective transporters of the conserved properties. This is an approach that is gaining interest, but not so much in industrial application;
3. Unsteady Reynolds-averaged Navier-Stokes equations: this approach consists in averaging the Navier-Stokes equations, over an ensemble of realizations, or over a coordinate in which the mean flow does not vary. These equations form a set of partial differential equations, but not a closed one: later, will be demonstrated the

need of other additional models. In this approach, turbulent scales are not solved, unlike DNS and LES, but only statistics.

For this thesis, URANS have been chosen: in particular, SST Menter $k-\omega$ and Spalart-Allmaras turbulence models have been employed. For a detailed explanation on these numerical models, see Appendix A.

2.3 Discretization scheme and solver

In most situations, the physics being simulated dictates the choice between steady and unsteady models: in this case study (i.e., flow past a cylinder at high Reynolds number, with a following thermic study), a time-dependent simulation seems more suited even if much more computationally expensive.

The reason why the unsteady analysis has been chosen relies on few observations: the first concerns the simulation's residuals, which have higher value in the steady-state condition than in the unsteady one (except for sdr, see Fig. 20).

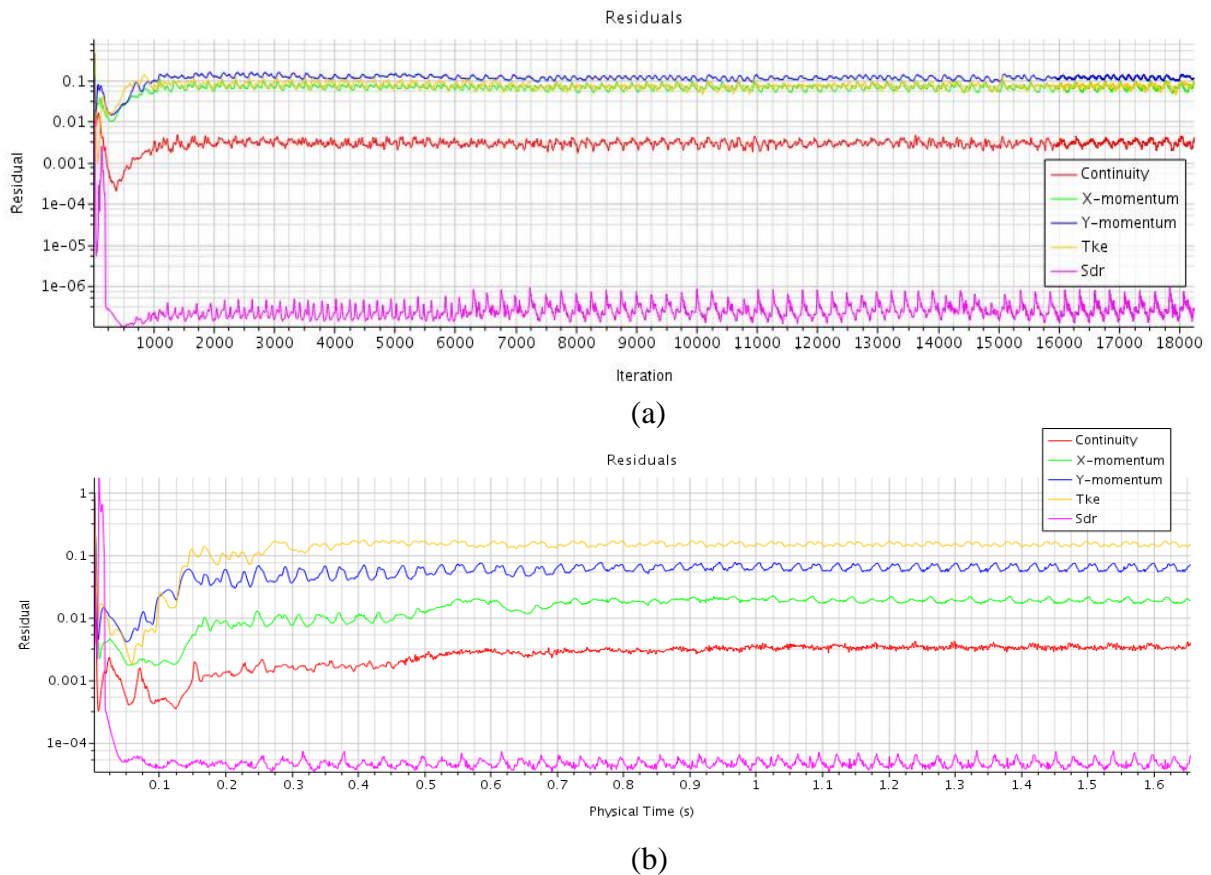
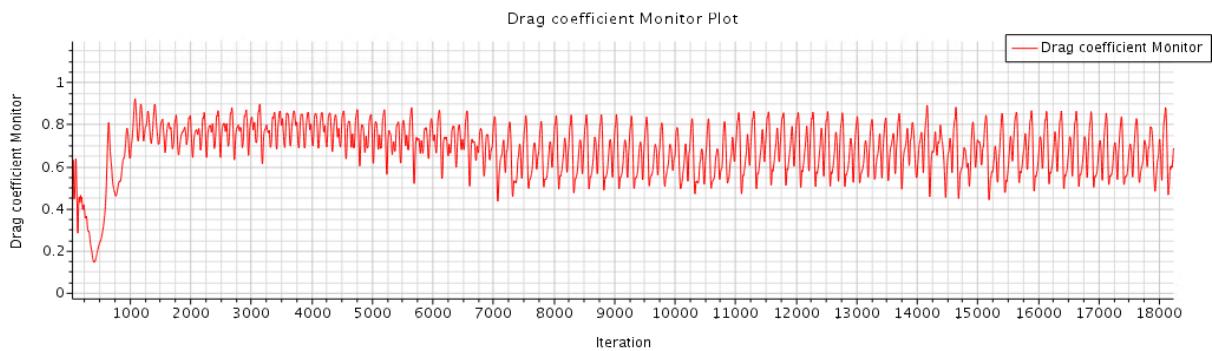
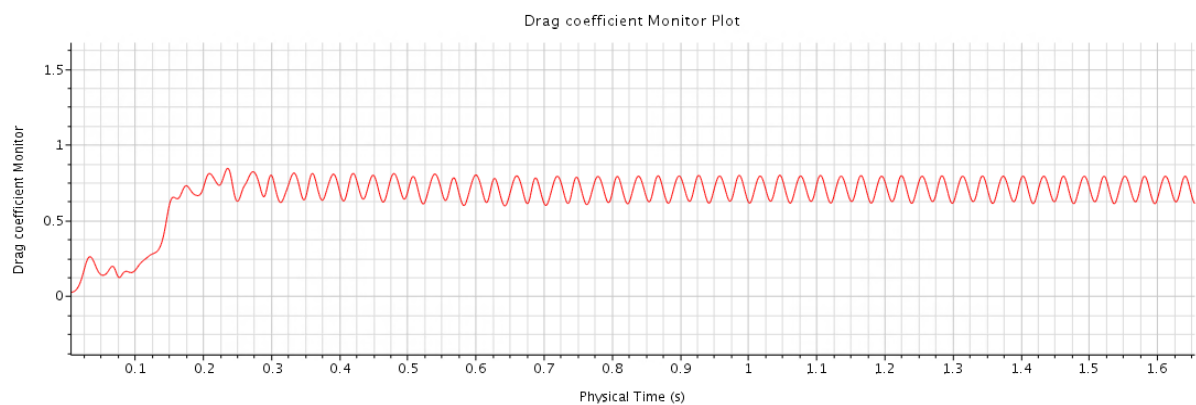


Figure 20: Comparison of residuals' plot, where 'Sdr' is the Specific dissipation rate and 'Tke' is the Total kinetic energy. (a) Steady-state simulation (b) Unsteady-state simulation

The second observation concerns the drag coefficient profile: indeed, looking at Fig. 21, the drag coefficient oscillations are non-periodic and irregular in the steady simulation, whereas clearly periodic and regular in the unsteady one. This let me guess that the physics of the problem is better caught by an unsteady analysis.



(a)



(b)

Figure 21: Comparison of drag coefficient profiles. (a) Steady-state simulation (b) Unsteady-state simulation

As last evidence of this choice, movie clips have been exported from STAR-CCM+ to look at the whole evolution of pressure and velocity field: obviously, they cannot be shown here, but pictures of pressure and velocity field have been extracted and shown below to make the reader understand the difference (see Fig. 22).

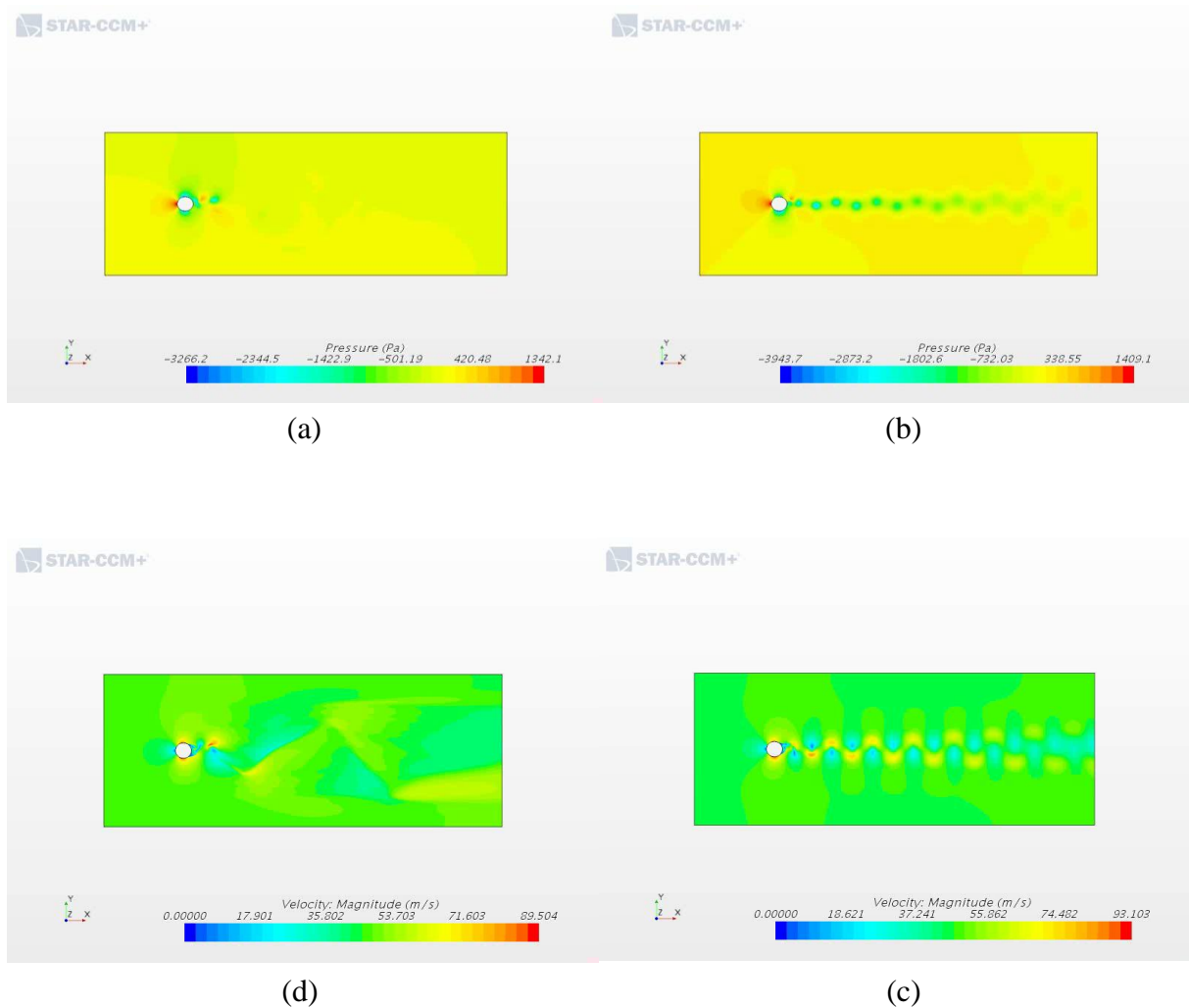


Figure 22: Screenshots of 2-dimensional, converged flow field. (a) Steady state, pressure field (at 18000th iteration) (b) Unsteady state, pressure field (at 1.6 s) (c) Steady state, velocity field (at 18000th iteration) (d) Unsteady state, velocity field (at 1.6 s)

Regarding the flow model, it is possible to choose between coupled and segregated flow: as suggested by [9], for incompressible external flow with $Ma < 0.2$, the segregated solver is normally preferred because is faster and uses less memory. A second-order upwind scheme has been selected for the spatial discretization, being nominally second-order accurate.

This solver is a solution iterative algorithm used by STAR-CCM+ that solves the governing equations sequentially (i.e., segregated from one another), treating each equation as if it has a single variable, whereas treating temporarily the other unknowns as known. This is called inner iteration.

Because of their non-linearity, numerous iterations of the solution loop are required before reaching the convergence: these are called outer iterations. Therefore, resuming, each outer iteration is made up by few steps both outlined below:

1. fluid properties are updated, based on the current solution;
2. momentum equations (one for each velocity component) are solved using current values for pressure and mass fluxes, updating the flow field;
3. since the flow field obtained at the previous step may not satisfy the continuity equation, the Poisson equation is solved (forcing the divergence of velocity field to be zero) obtaining the necessary corrections to the face mass fluxes, pressure and velocity field in order to comply with the continuity equation;
4. equations for scalars such as energy or turbulence are solved using the previously updated values of the other variables
5. A convergence test at the end of each of this procedure is made.

The convergence of the outer iterations is not guaranteed a priori, thus it requires careful choice about the number of inner iterations. Moreover, the delicacy of this convergence requires to take the results of the old and new outer iteration into consideration by means of weight factors, so under-relaxing the code: this is called convex combination. The selection of these under-relaxation parameters is mainly empirical.

CHAPTER 3

TWO-DIMENSIONAL STUDY

In the two-dimensional study, only the fluid-dynamic aspect of the physics is investigated, leaving the thermic one to the three-dimensional analysis. So, only the air is considered.

All the preprocessing is performed using STAR-CCM+. In this CFD software, the procedure follows a precise path: build the geometry, generate the mesh, define the physics and set all the proper scenes/plots useful to postprocess the case study, then start the simulation and, at the end, establish the validity of the simulation by the verification and validation (V&V) process.

3.1 Computational domain

The computational domain is created in such a way that the fluid flow around the cylinder is not disturbed by any of the boundaries, i.e., the boundaries should not affect the fluid flow in any way.

A sufficient extended analysis region has been employed, based on recommendations of [7]:

- $\geq 5D$ upstream
- $\geq 15D$ downstream
- $\geq 5D$ aside

So, considering the origin coincident with the center of the cylinder, the chosen domain size is: $5D$ upstream and on both sides, $20D$ downstream (see Fig. 23).

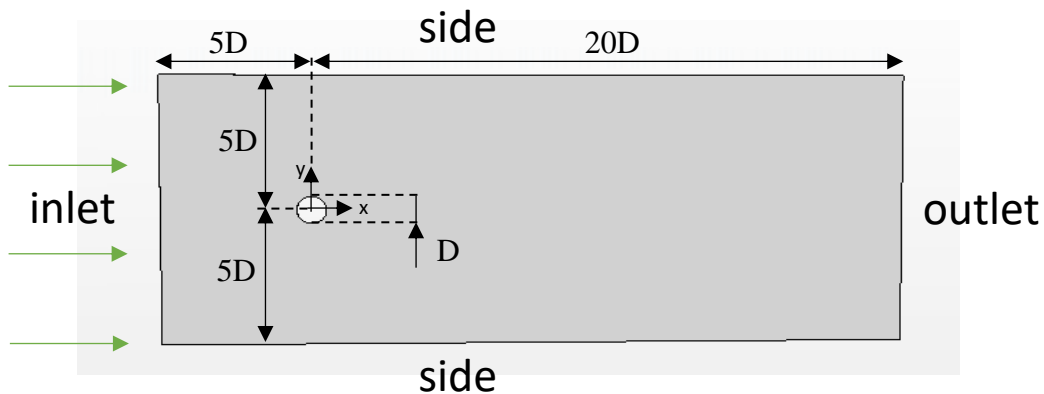


Figure 23: Computational domain

3.2 Initial conditions and boundary conditions

For the two-dimensional analysis, the initial condition is set for the velocity of the uniform free-stream flow: $u = U_\infty$, $v = w = 0$.

The type of boundary conditions used are:

- At the inlet: velocity inlet, i.e. a Dirichlet condition on the velocity component in the streamwise direction and turbulent quantities is applied, whereas the boundary face pressure is extrapolated from adjacent cells using reconstruction gradients;
- At the outlet: since the outlet boundary cannot be set infinitely far from the cylinder, it is not possible to set a Dirichlet boundary condition on the velocity, as for the inlet. A different condition is commonly taken: it is called pressure outlet, i.e. a (gauge) pressure value is specified to be equal to zero, since it can be shown analytically that the energetic pressure modes in the wake decay much faster than the velocity ones.

The boundary face velocity is extrapolated from the adjacent cells using reconstruction gradients.

- At both sides: symmetry plane, i.e. the shear stress is set to zero and the boundary face pressure and velocity are extrapolated from the adjacent cells using reconstruction gradients;
- At the receiver surface: wall, i.e. the velocity is set to be equal to zero on it, and the boundary layer pressure is extrapolated from adjacent cells using reconstruction gradient.

3.3 Mesh

The mesh in STAR-CCM+ has been generated by means of the tool Badge for two-dimensional meshing: the surface lying on the plane $Z=0$ is recognized and the mesh is generated on it.

The polyhedral type mesh has been used on the computational domain because it is relatively easy, efficient and contains almost five times fewer cells than a tetrahedral mesh for a given starting surface. Due to the need of better describe the features of the flow near the wall (i.e., the boundary layer), a finer mesh has been imposed using the prism layer mesh (automatically applied by STAR-CCM+ on boundaries specified as wall): it consists in

subdividing an imposed area in a suitable number of prism layers, with a certain layer stretching. Furthermore, the regions around the receiver and along the wake have been refined to better catch the evolution of the flow: Fig. 24 shows the initial mesh.

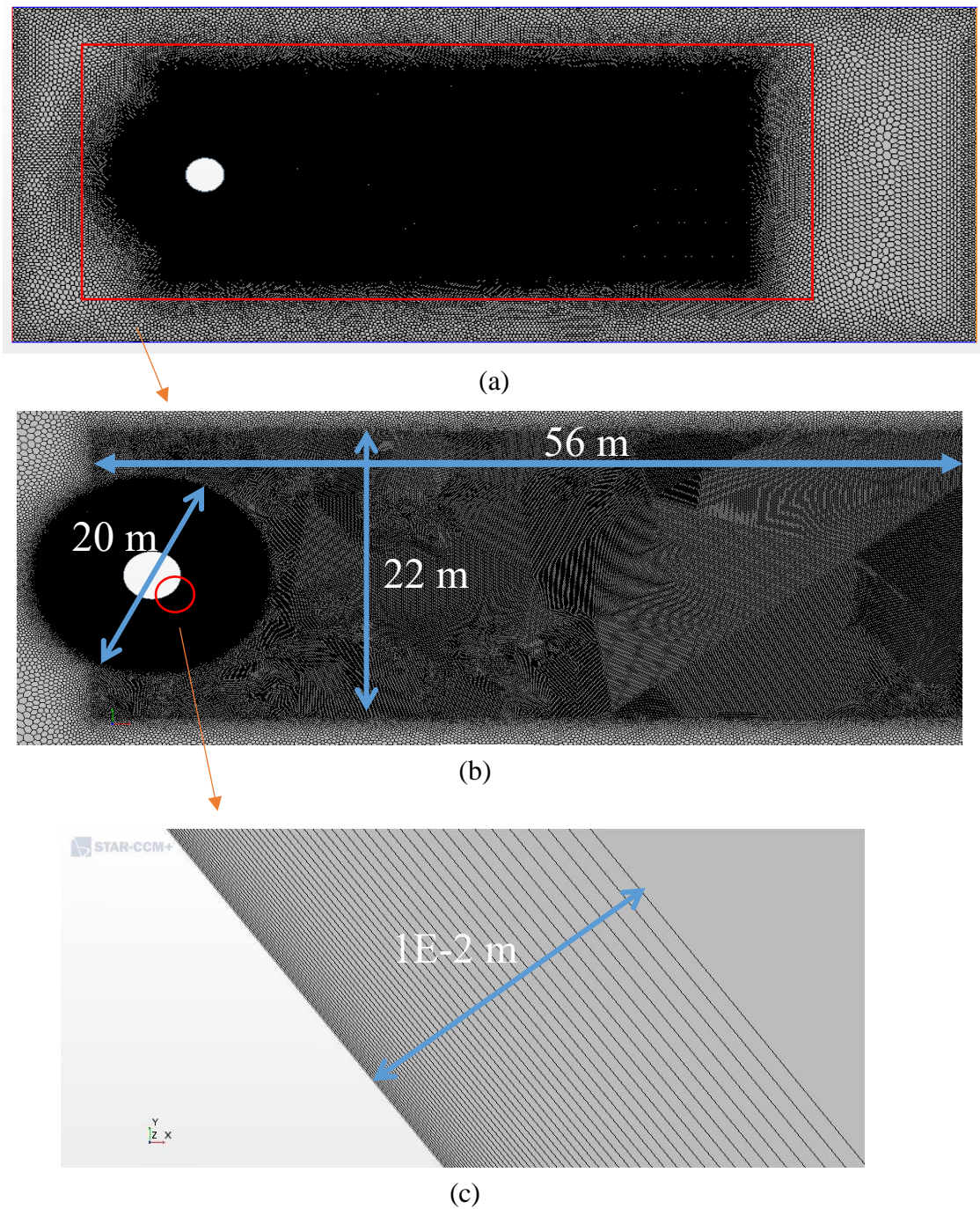


Figure 24: Air, 2-dimensional, initial mesh. (a) Whole domain, (b) Zoom on the two volumetric control regions, (c) Zoom on the prism layers region

The prism layer total thickness has been adjusted with the following criterion, as cited in [10]: the maximum turbulent viscosity should be in the middle of the boundary layer (see Fig 25).

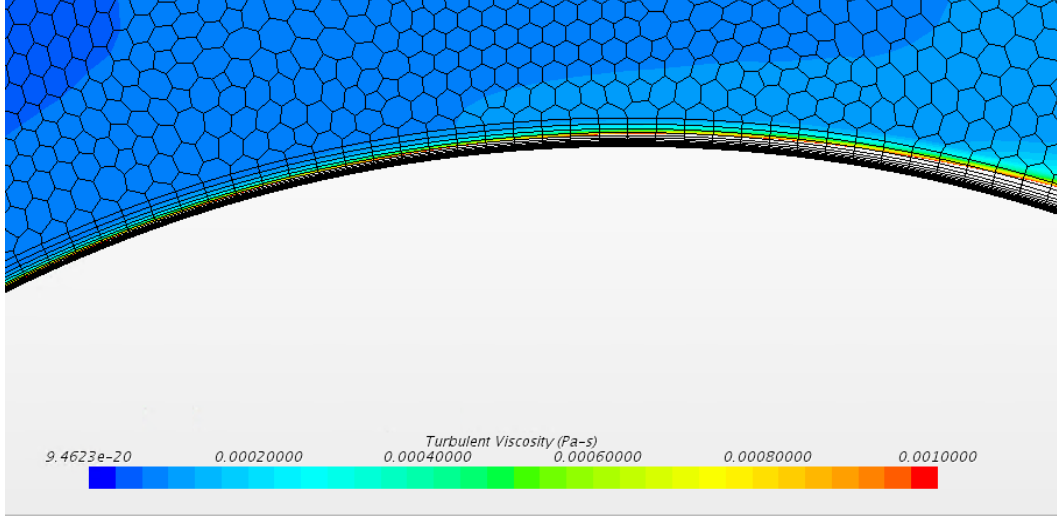


Figure 25: Detail of the 2-dimensional turbulent viscosity field within the prism layer region

Moreover, the prism layer near wall thickness has been calculated by means of the wall- y^+ , given as:

$$y^+ = \frac{u_* y_w}{\nu} \quad (46)$$

where u_* represents the friction velocity at the nearest wall, y_w is the element height (at the nearest wall) in the radial direction and ν in the kinematic viscosity of the fluid. It is a fundamental physical quantity that helps to catch the physics of the viscous sub-layer.

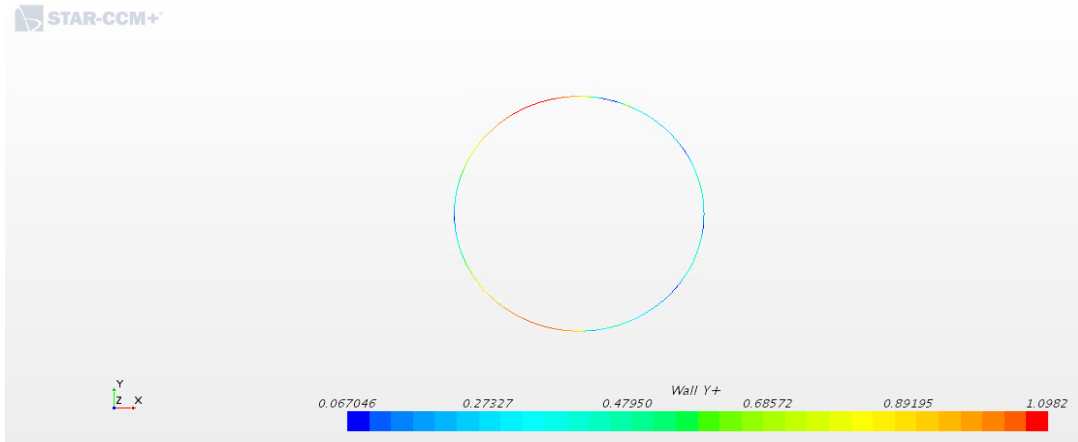


Figure 26: Wall- y^+

For both the turbulence models tested in this thesis (Spalart-Allmaras and SST $k-\omega$), [9] suggests to use the All- y^+ treatment: that is, ensuring $y^+ \leq 1$ (without using wall functions) or

$y^+ \geq 30$ (using wall functions). Because the thermal analysis will impose to have $y^+ \leq 1$, we opted for this choice for the 2D study, having a maximum around 1 and an acceptable minimum (see Fig. 26).

These two criteria about the prism layer total thickness and prism layer near wall thickness have been followed for all the simulations of the thesis.

A summary of the initial mesh is given in TABLE III.

TABLE III: INITIAL SPECIFICATIONS FOR THE EXTERNAL FLOW (WITH CIRCULAR CYLINDER) 2-D MESH

Mesh type	Polyhedral
Base size, [m]	0.5
Target surface size, [-]	100 % base size
Minimum surface size, [-]	50 % base size
Surface growth rate, [-]	1.05
# of prism layers, [-]	50
Prism layer total thickness, [m]	0.01
Prism layer near wall thickness, [m]	5E-05
Base size of circular region around the receiver	10 % base size
Base size of the rectangular region along the wake	25 % base size
# of cells	350k

3.4 Circular cylinder

3.4.1 Verification

Verification step does not confirm if the model is correct or not, but only which is the accuracy of the of the code and make sure the code has no bugs. It will be possible to conclude if the code is good enough and if it has no bugs.

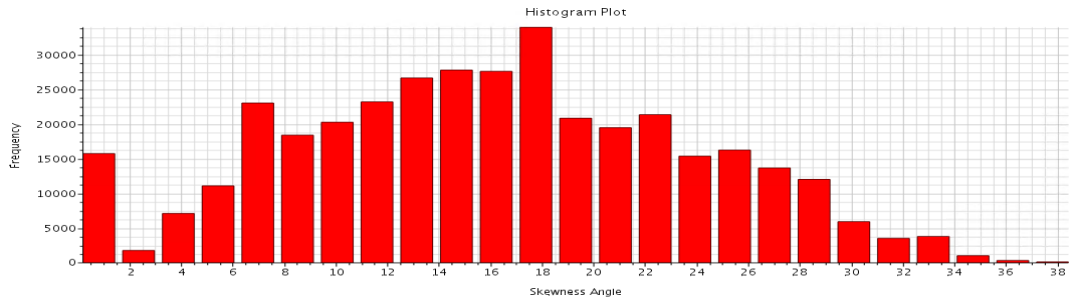
Two types of grid independence studies have been approached, with the $k-\omega$ model for the most critical scenario: one varying the number of prism layers and the other varying the base size; a time-step independence study has been provided too. For each different value of base size considered, a mesh diagnostic has been done because, even though a mesh is valid and the solution is successfully initialized with an appropriate space model, poor mesh quality can negatively affect the final solution.

The quality measurements survey:

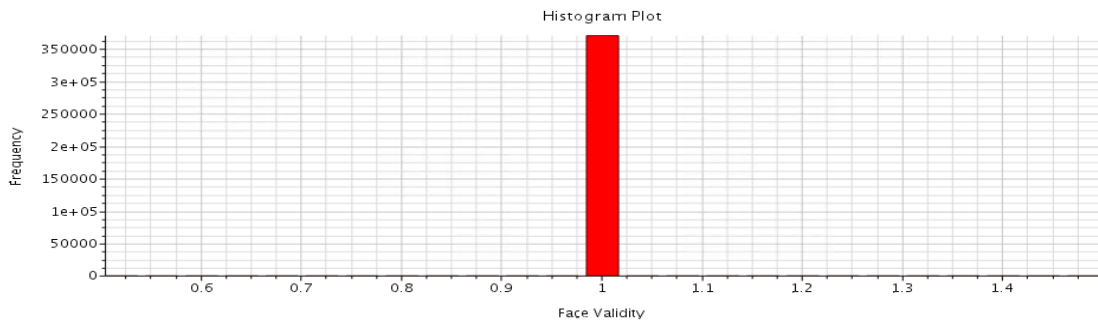
- Skewness angle: a good mesh has the following threshold $\rightarrow \theta_{\max} < 85^\circ$;

- Face validity: a face validity of 1.0 means that all face normal are correctly pointing away from the cell centroid. Values below 1.0 mean that some of the cell faces have normal pointing inward towards the cell centroid, indicating some form of concavity. Values of below 0.5 signify a negative volume cell. Cells with a face validity below 1.0 are considered bad.
- Volume change: a value of 1.0 indicates that the cell has a volume equal to or higher than its neighbors; cells with a volume change of 0.01 or lower are considered bad cells. A large jump in volume from one cell to another can cause potential inaccuracies and instability in the solvers;
- Chevron quality indicator: Chevron cells are marked as 1.0 and considered bad cells. Every other cell is marked as 0.

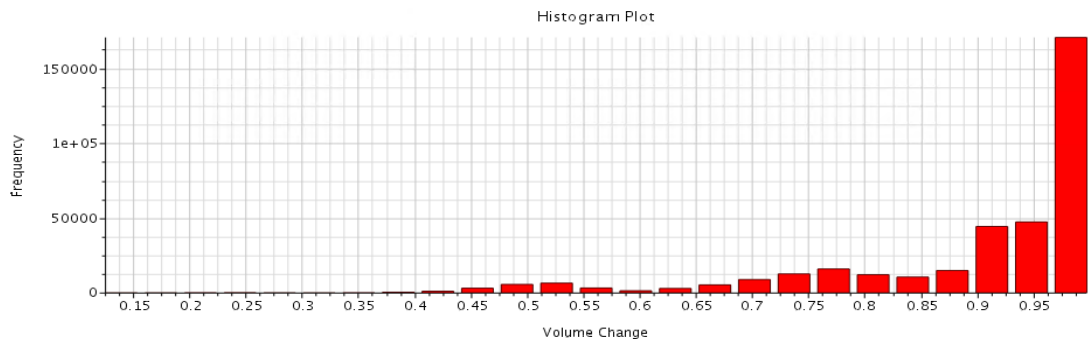
Each of these monitors has been plotted in a histogram plot, as Fig. 27 shows in the next page.



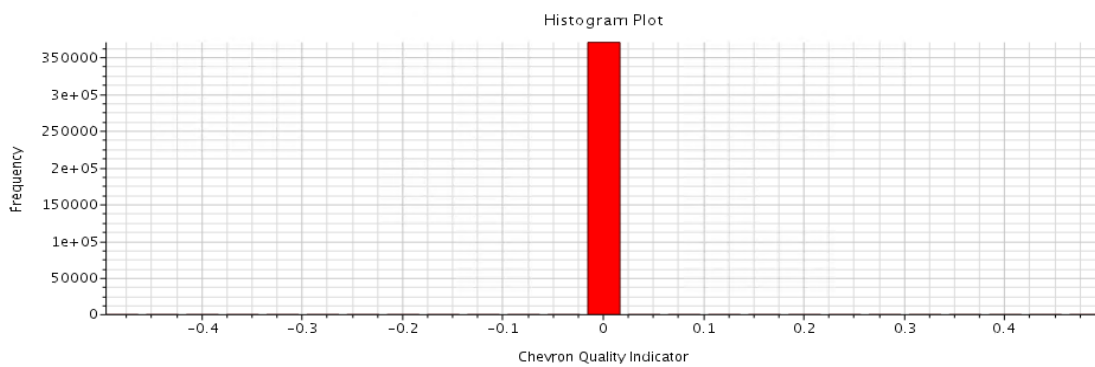
(a)



(b)



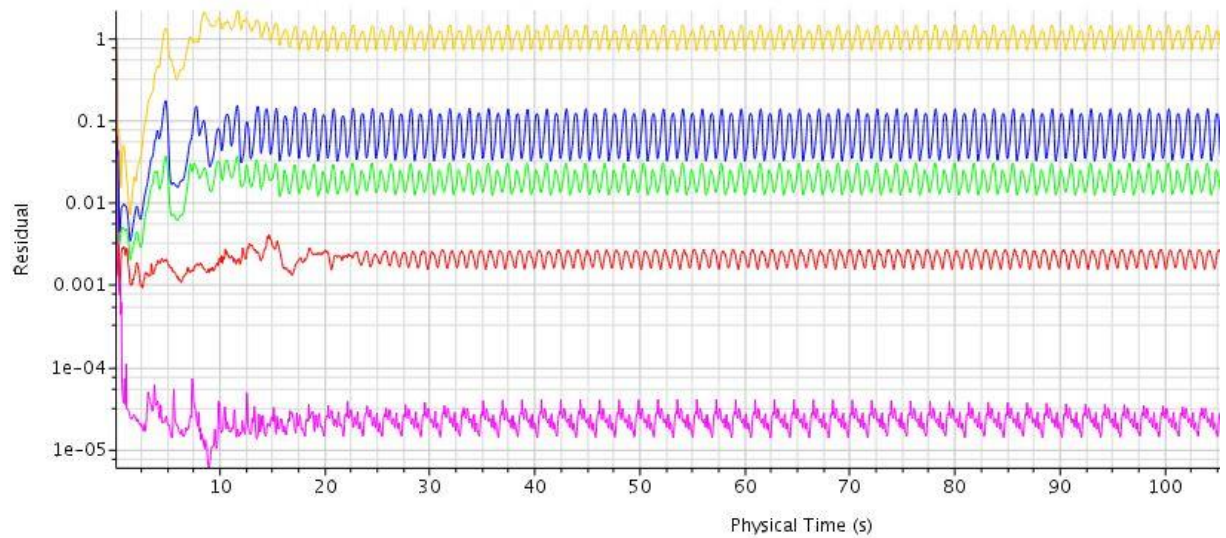
(c)



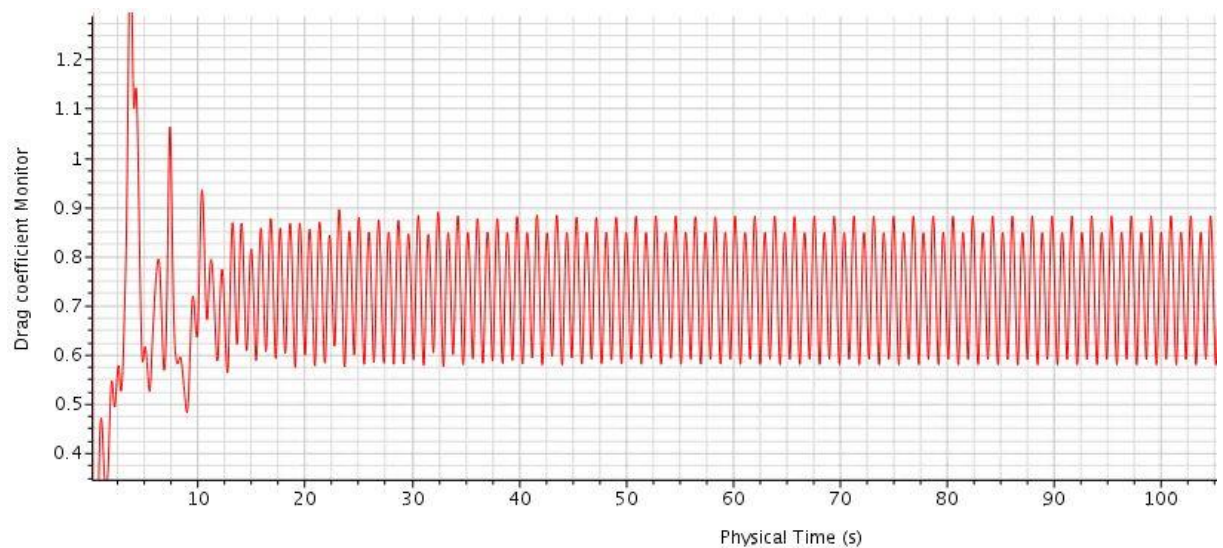
(d)

Figure 27: Air, 2-dimensional mesh quality measurements. (a) Skewness angle (b) Face validity (c) Volume change (d) Chevron quality indicator

Before stopping the simulation to export data, a check on their reliability has been issued through the residuals (see Fig. 28.a) and the drag coefficient (see Fig. 28.b). Once the simulation has been considered statistically stationary, the profile of the drag coefficient in that interval has been postprocessed with Excel, obtaining the time-averaged drag coefficient, and obtaining a plot through Matlab.



(a)

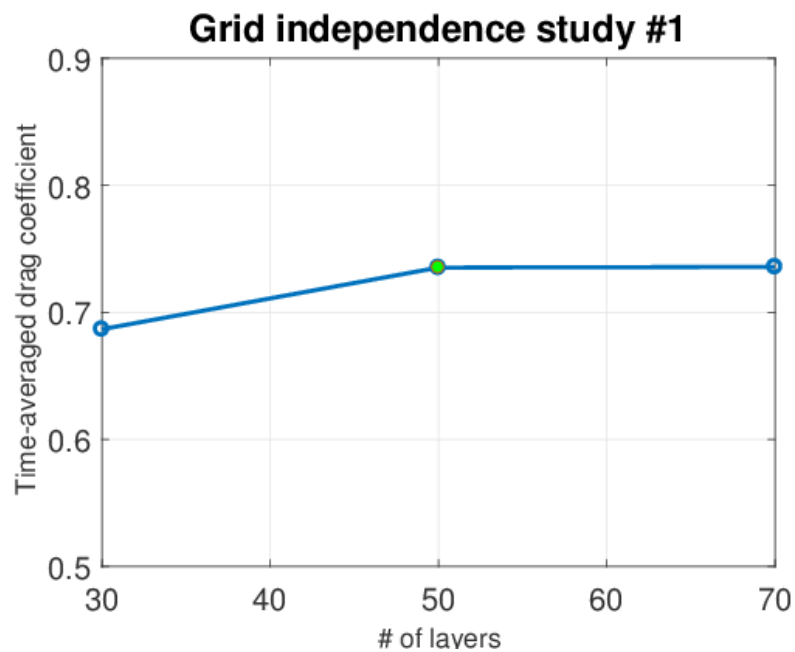


(b)

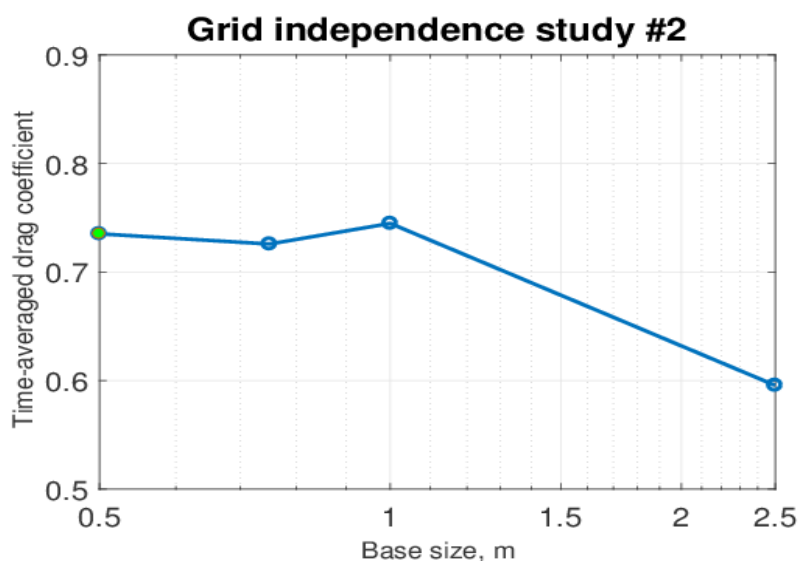
Figure 28: 2-dimensional, hydraulic simulation's monitors. (a) Residuals (b) Drag coefficient

The first grid independence study concerns the number of prism layers: maintaining constant the mesh specifications previously cited in TABLE III and setting an initial time-step of 0.05 s, only the number of prism layers has been modified, obtaining the time-averaged drag coefficient (see Fig. 29.a).

The result is that one with the green circle: 50 layers. The greater number of layers provides the same result, but it is too expensive for the following three-dimensional study.



(a)



(b)

Figure 29: Air, 2-dimensional grid independence study (a) # of layers (b) base size

The second grid independence study concerns the base size: fixing the optimal number of layers just obtained and maintaining constant all the other mesh specifications previously cited in TABLE III, setting an initial time-step of 0. s, only the base size has been modified, obtaining the time-averaged drag coefficient (see Fig. 29.b).

The result is that one with the green circle: 0.5 m. Even if the convergence study is irregular, simulations with smaller grid sizes would not have been feasible with the present computational resources.

Therefore, fixing the optimal number of layers and base size, and maintaining all the other mesh specifications of TABLE III, only the time-step has been modified, providing a time-step independence study (see Fig. 30). Smaller time-steps have not been tested because of the excessive computational time required. The result is that one with the red circle: 0.05 s.

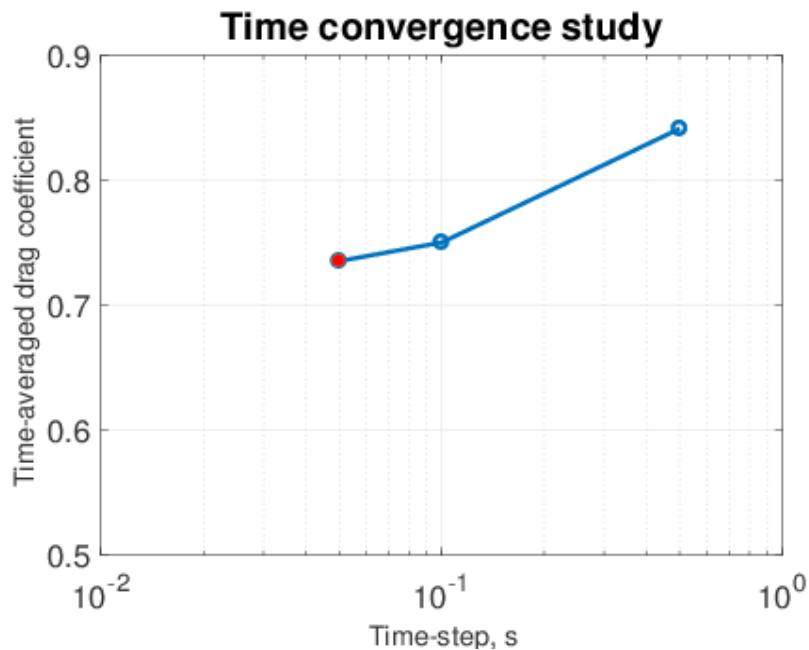


Figure 30: 2-dimensional, external flow, time independence study

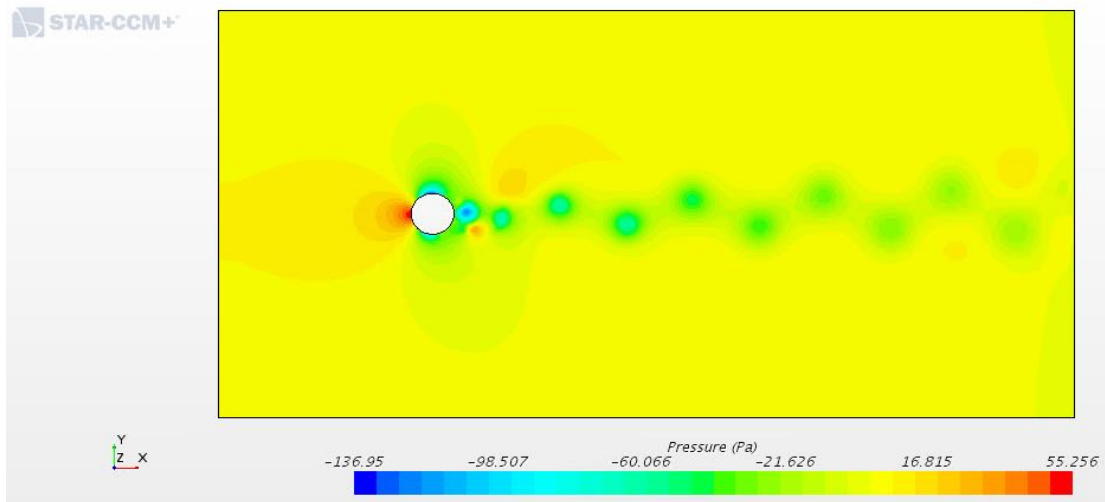
Thus, the final mesh has the following specifications:

TABLE IV: FINAL SPECIFICATIONS FOR THE EXTERNAL FLOW (WITH CIRCULAR CYLINDER) 2-D MESH

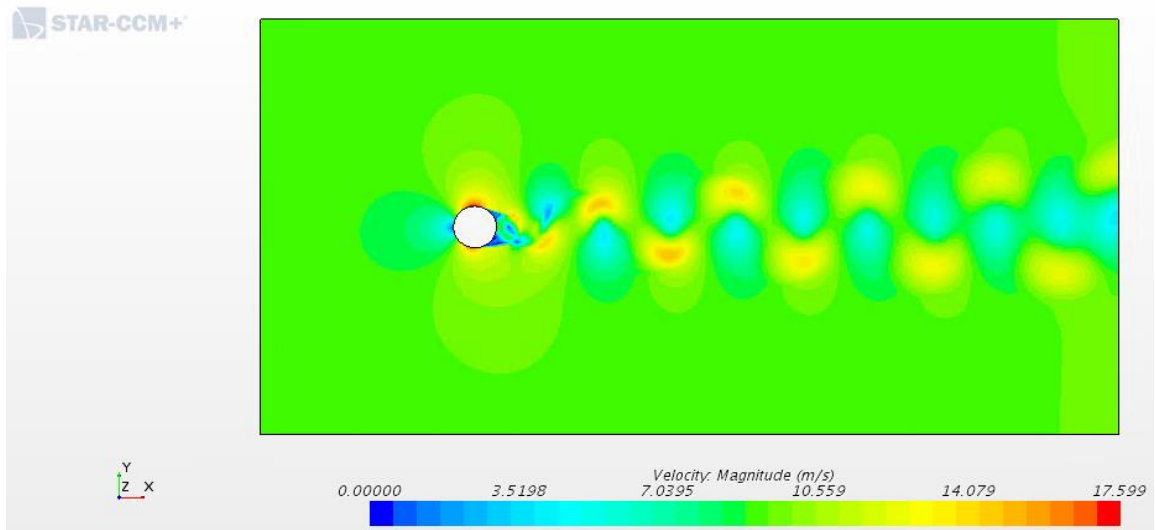
Mesh type	Polyhedral
Base size, [m]	0.5
Target surface size, [-]	100 % base size
Minimum surface size, [-]	50 % base size
Surface growth rate, [-]	1.05
# of prism layers, [-]	50
Prism layer total thickness, [m]	0.01
Prism layer near wall thickness, [m]	5E-05
Base size of circular region around the receiver	10 % base size
Base size of the rectangular region along the wake	25 % base size
# of cells	350k

with a time-step of 5E-02 s and 15 inner iterations per time-step.

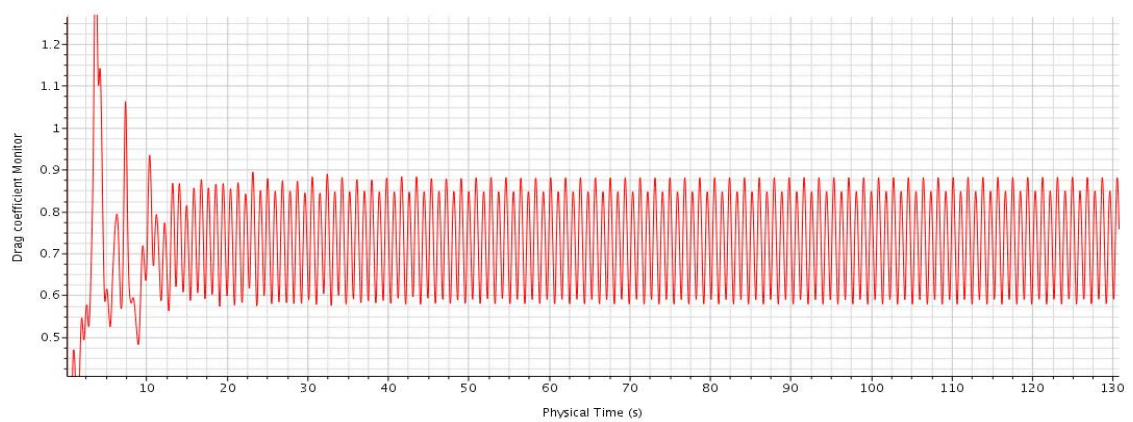
The resulting flow field is shown in the figures in the next page.



(a)



(b)



(c)

Figure 31: 2-dimensional, circular receiver flow field. (a) (Gauge) pressure field at last time-step, (b) Velocity field at last time-step, (c) Drag coefficient

For the purpose of the successive validation, other smaller Reynolds numbers have been tested: changing the Re, the physics of the flow changes too. This required as many time-step independence studies as the number of Re tested (see Fig. 32), maintaining the same mesh, since it was verified for the highest Re.

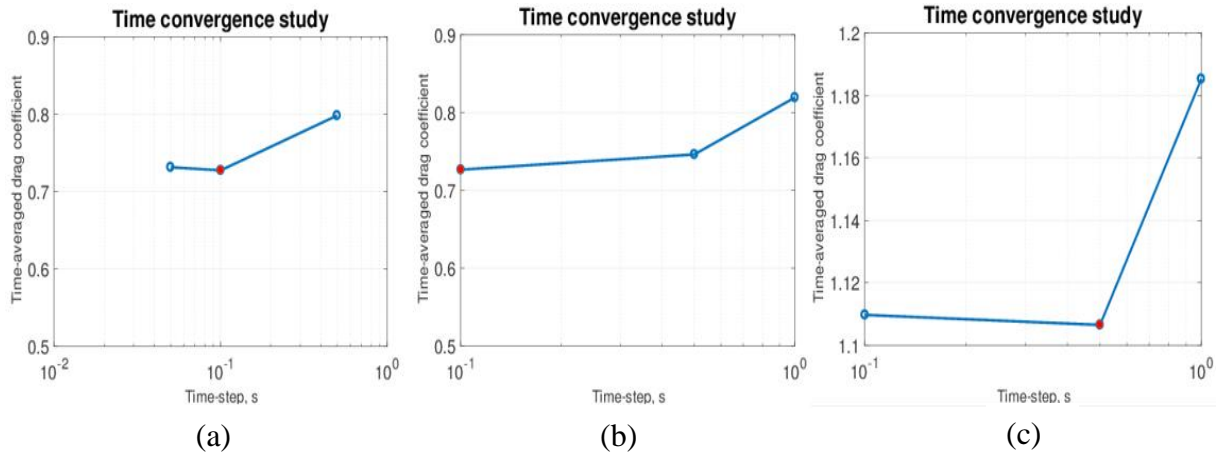


Figure 32: 2-dimensional, circular receiver, time-step independence studies for different Re. (a) $Re = 1.05E+06$ (b) $Re = 4.4E+05$ (c) $Re = 1.0E+05$

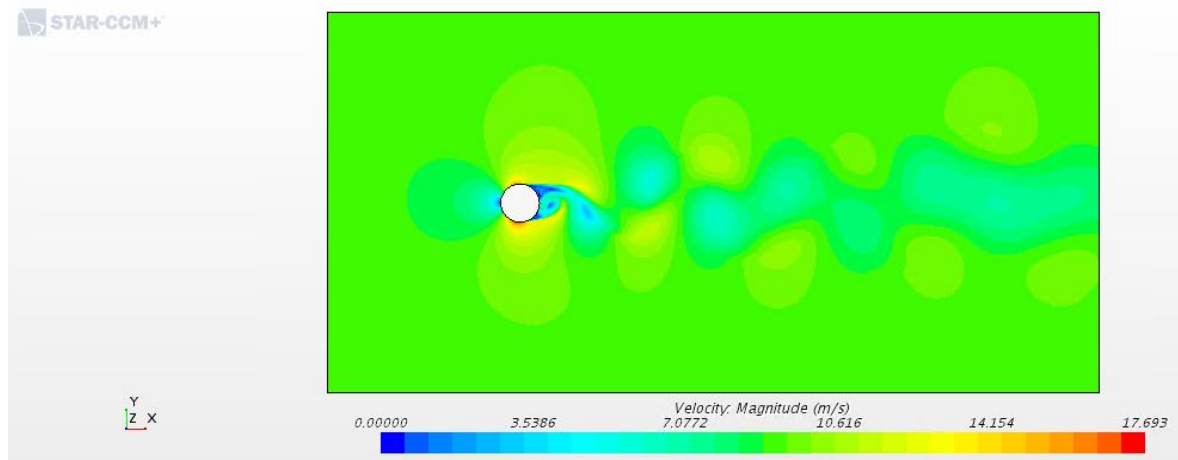
3.5 Polygonal cylinder

Keeping the same domain and optimal mesh, the circular cylinder has been replaced with a 24-sided polygonal cylinder. At this step, the verification has not been pursued because the domain has not been modified; only the prism layer total thickness and the prism layer near wall thickness have been checked according to the rules previously explained.

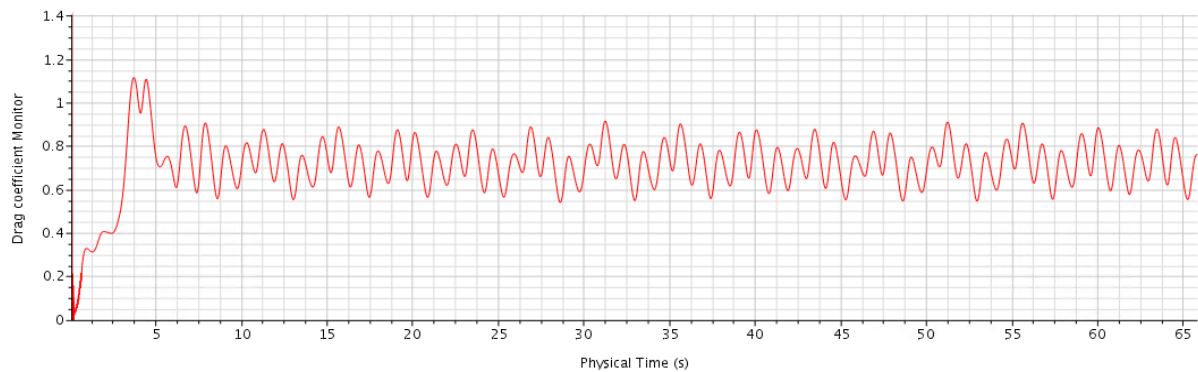
TABLE V: SPECIFICATIONS FOR THE EXTERNAL FLOW (WITH POLYGONAL CYLINDER) 2-D MESH

Mesh type	Polyhedral
Base size, [m]	0.5
Target surface size, [-]	100 % base size
Minimum surface size, [-]	50 % base size
Surface growth rate, [-]	1.05
# of prism layers, [-]	50
Prism layer total thickness, [m]	0.01
Prism layer near wall thickness, [m]	5E-05
Base size of circular region around the receiver	10 % base size
Base size of the rectangular region along the wake	25 % base size
# of cells	350k

The resulting flow field is shown in the figures below.



(b)



(c)

Figure 33: 2-dimensional, polygonal receiver flow field. (a) (Gauge) pressure field at last time-step, (b) Velocity field at last time-step, (c) Drag coefficient

Very few experimental data are available for a 24-sided polygon. However, experiments with polygons with lower number of sides have been made, even if mainly for lower Reynolds numbers: Fig. 34 compares the drag coefficient as function of Re [11] obtained from circular receiver and polygonal receiver with the results of experiments on 8/12/16-sided polygons.

As it can be noticed for moderately Re , data are quite scattered among all cases but, they seem to converge to a single value of drag coefficient when approaching $Re=10^6$: i.e. the polygons tend to behave as a circle (represented by the Achenbach experimental curve) in that range. However, results from SCENARIO #1 seem to not agree with the observation made above, maybe due to a not optimal space/time discretization of the employed CFD model for this Re .

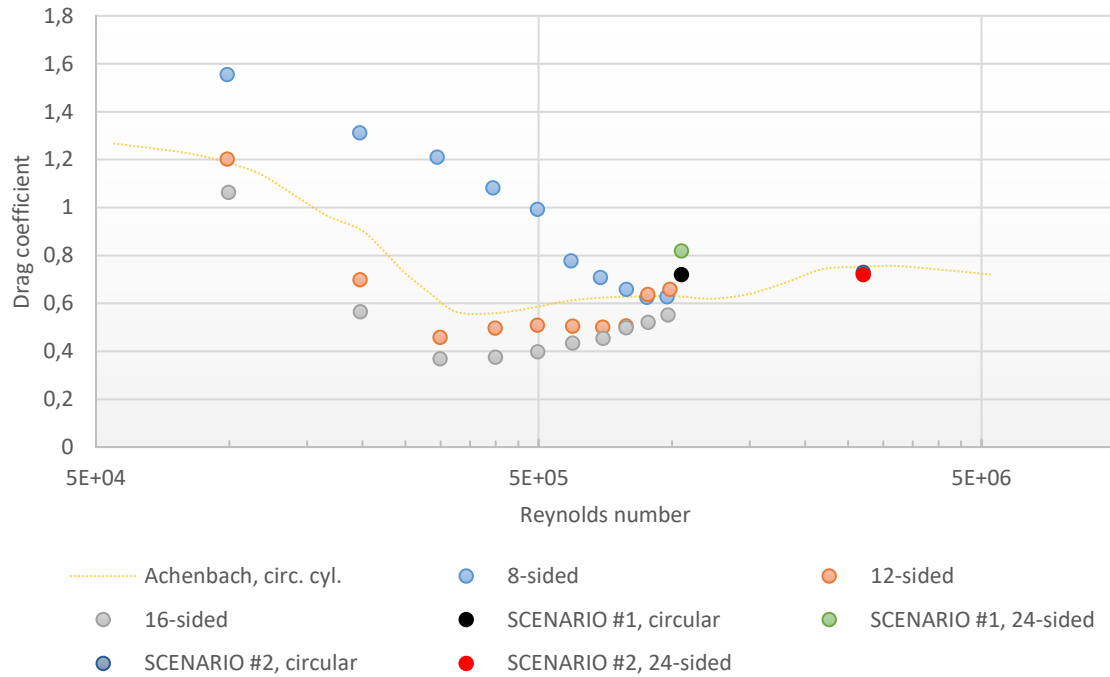


Figure 34: Drag coefficient as function of Reynolds number, for circular and different n -sided polygonal cylinder (adapted from [11])

On the other hand, for SCENARIO #2 circular cylinder's simulation and polygonal cylinder's one achieve almost the same time-averaged drag coefficient (~ 0.72 , even if oscillations are more irregular in the polygonal cylinder's case) and the overlapping of the results obtained until this phase seems to confirm what stated above.

3.6 Benchmark

In this step the model/code/solution is benchmarked against solutions provided by other CFD codes used by recognized and reliable authors within the fluid-dynamic community: here, the quality of the code is tested.

DNS data are not available for this range of Re ; however, data from other less computationally expensive numerical studies are available and it is possible to benchmark our results against those ones.

Looking at Fig. 35, discrepancies between SST $k-\omega$ and S-A results are evident, but however small in the supercritical regime. Moreover, they overpredict the C_D with respect to the other results, above all with respect to URANS $k-\epsilon$.

This might be caused by:

- Different implementation of wall functions, or
- Different initial/boundary conditions

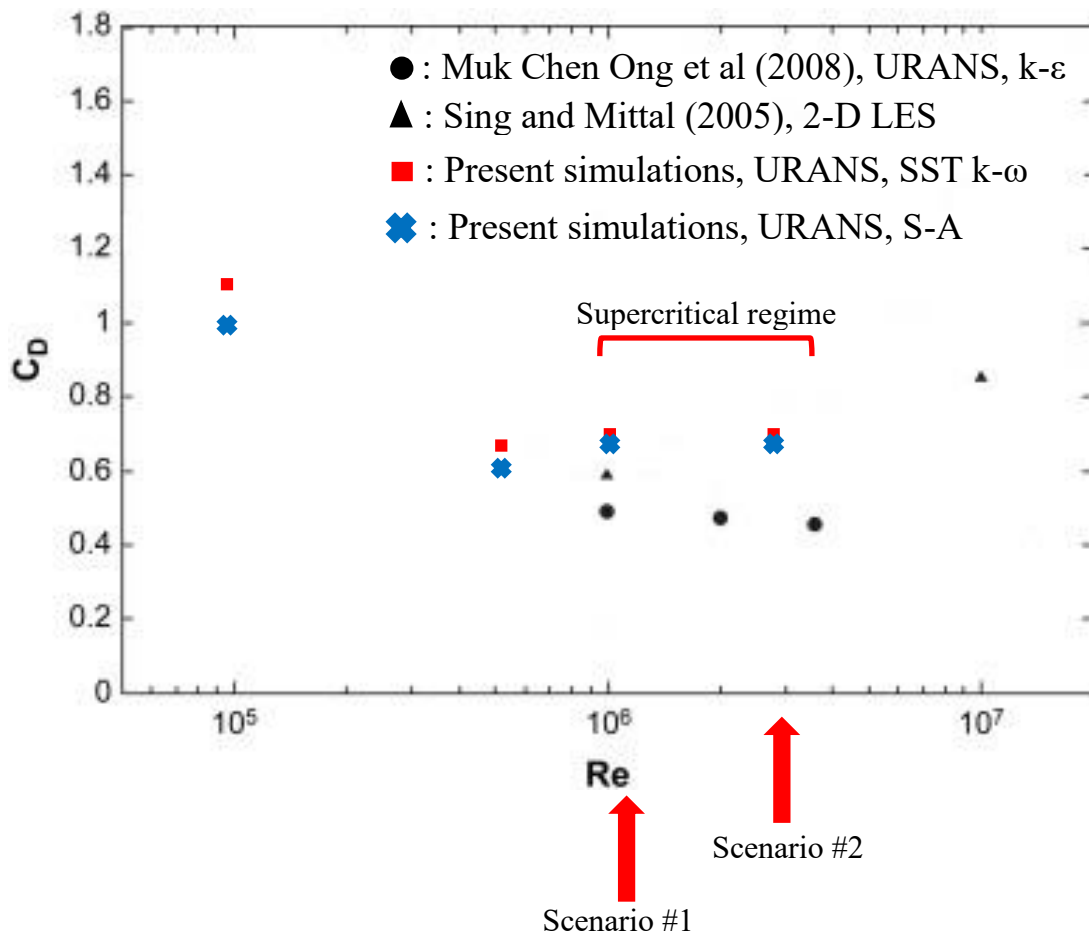


Figure 35: Benchmark of 2-dimensional, circular cylinder results (adapted from [16])

3.7 Validation

The validation phase concerns the comparison between the numerical study and the experimental measurements: here, the quality of the model is investigated.

Adopting the optimal values of mesh and time-step obtained from the previous independence studies, numerical simulations have been approached by changing only the Reynolds number (through imposing the proper free-stream velocity at the inlet). To develop this phase, the Spalart-Allmaras turbulence model has been used also.

As it is possible to observe in Fig. 36, the obtained numerical results and the different experimental curves are compared: a wide scatter of C_D is in the super-critical regime among various experiments, suggesting high sensitivity of the flow to perturbations due to surface

roughness or free-stream turbulence. However, the Achenbach's curve will be the reference curve for this thesis, because of his wide application.

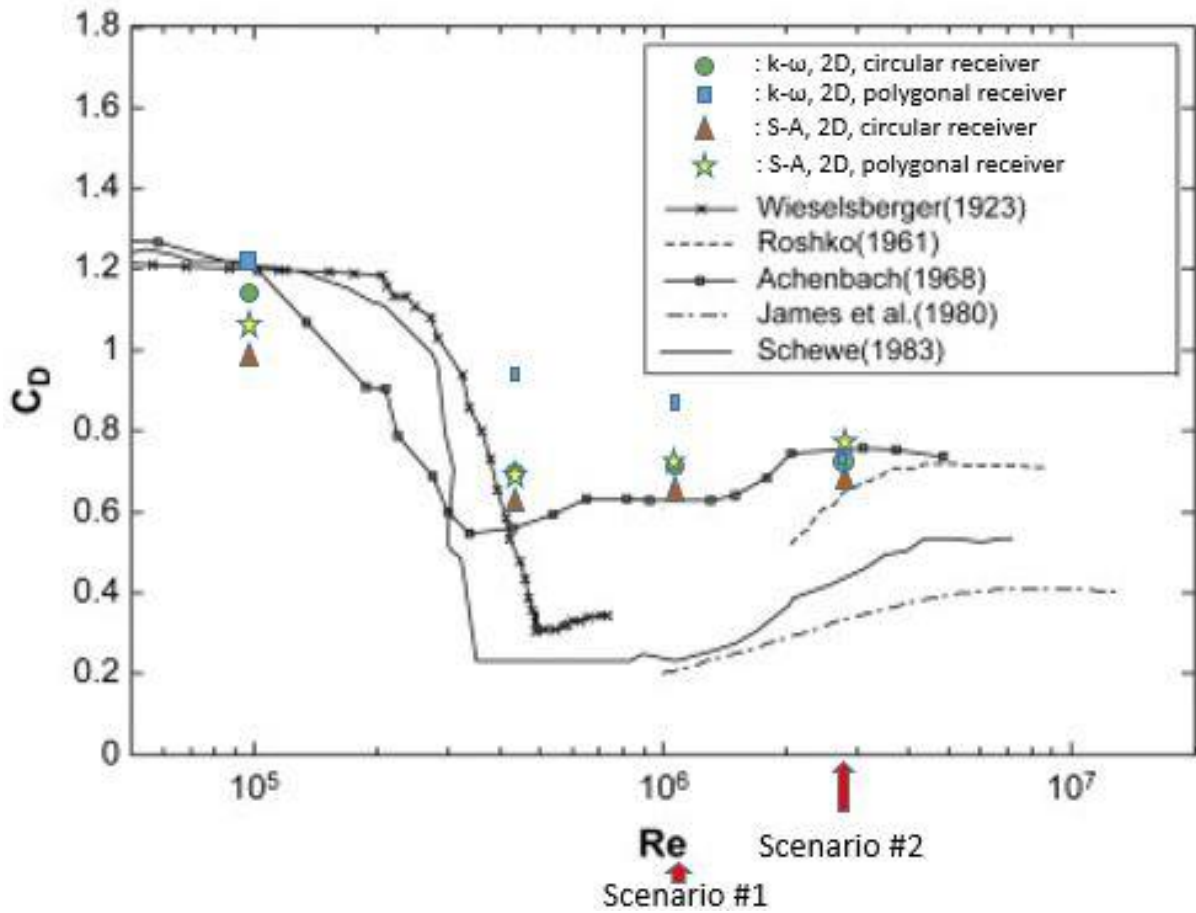


Figure 36: Validation of 2-dimensional results (adapted from [16])

The figure shows that $k-\omega$ turbulence model gives almost total different results between circular and polygonal cylinder and it doesn't capture the drag coefficient decrease in the central range of the Reynolds interval (only for polygonal cylinder). Spalart-Allmaras turbulence model, on the other hand, shows better results, almost following tightly experimental Achenbach's experimental curve (both for circular and polygonal cylinder).

It is important to highlight that the Spalart-Allmaras model is computationally less time-consuming (around half the time) than $k-\omega$, because of the lower number of equations to be solved. This is particularly attractive in the larger calculations performed in 3D analysis.

CHAPTER 4

THREE-DIMENSIONAL STUDY

In the three-dimensional study, both the fluid-dynamic and the thermal fluid-dynamic aspects of the physics are studied.

4.1 Computational domain

The computational domain is created in such a way that the fluid flow around the cylinder is not disturbed by any of the boundaries, i.e., the boundaries should not affect the fluid flow in any way.

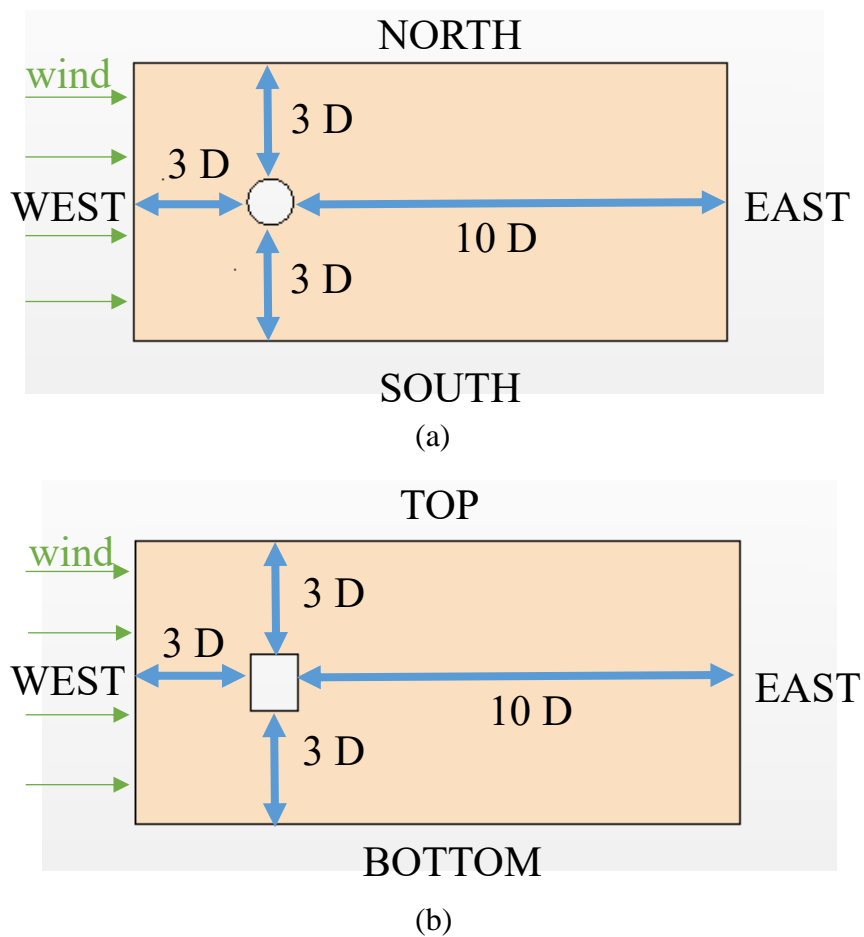


Figure 37: Air, 3-dimensional, computational domain. (a) xy plane (b) xz plane

With respect to the two-dimensional analysis, the domain has been reduced on the equatorial plane. So, considering the origin coincident with the center of the cylinder, the chosen domain size is: 3D upstream, on both sides, above and below the cylinder and 10D downstream (see Fig. 37).

4.2 Initial conditions and boundary conditions

4.2.1 Air

Concerning the external flow, the initial condition is set for the velocity of the uniform free-stream flow: $u = U_\infty$, $v = w = 0$, and for the temperature: $T = T_\infty$.

The type of boundary conditions imposed are:

- West: velocity inlet;
- East: pressure outlet, i.e. a (gauge) pressure value is specified to be equal to zero, since it can be shown analytically that the energetic pressure modes in the wake decay much faster than the velocity ones.

The boundary face velocity is extrapolated from the adjacent cells using reconstruction gradients.;

- North/South: symmetry plane;
- Top/Bottom: Pressure outlet, i.e. this time setting an average (gauge) pressure $p_{\text{avg}} = 0$ as a scalar profile.

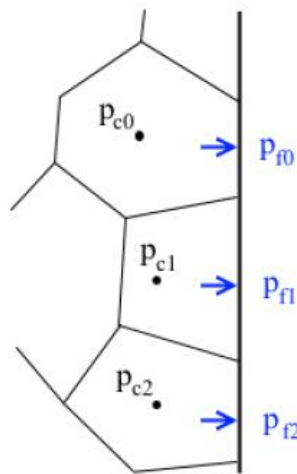


Figure 38: How pressure is adjusted on the faces of pressure outlet boundary [12]

The pressure profile from the cells next to the pressure outlet boundary is adjusted so that the average of that profile is equal to the average pressure value specified. This adjusted profile is then applied to the faces of the pressure outlet boundary:

The pressure at the boundary face of cell i is computed as:

$$p_{fi} = p_{avg} + \beta(p_{ci} - p_{c,avg}) \quad (47)$$

where:

- p_{avg} is the average pressure;
- β is the blending factor used by STAR-CCM+ to smooth out the pressure profile that is extrapolated from cells next to the pressure outlet boundary. The default value is $\beta = 0.5$, and this has been maintained;
- At the receiver surface: wall.

4.2.2 Receiver

Concerning the molten salts within the receiver, the initial condition is set for the velocity:

$u = v = w = 0$, and for the temperature: $T = T_{inlet}$.

The type of boundary conditions imposed are:

- E1/W1 inlet boundaries: mass flow inlet, i.e. a boundary for which the mass flow rate is known;
- Other inlet boundaries: velocity inlet;
- Outlet boundaries: pressure outlet;
- Internal vertical boundaries: wall, adiabatic;
- External vertical boundaries: wall, conducting.

4.3 Mesh

4.3.1 Air

Like the two-dimensional case, the polyhedral type mesh has been used on the computational air domain because it is relatively easy, efficient and contains almost five times fewer cells than a tetrahedral mesh for a given starting surface.

The prism layer total thickness and the prism layer near wall thickness have been with the same criteria of the two-dimensional case.

A summary of the initial mesh is given in TABLE VI.

TABLE VI: INITIAL SPECIFICATIONS FOR THE EXTERNAL FLOW (WITH POLYGONAL CYLINDER) 3-D MESH

	SCENARIO #1	SCENARIO #2
Mesh type	Polyhedral	Polyhedral
Base size, [m]	1.0	1.0
Target surface size, [-]	100 % base size	100 % base size
Minimum surface size, [-]	5 % base size	5 % base size
Surface growth rate, [-]	1.05	1.05
# of prism layers, [-]	30	30
Prism layer total thickness, [m]	0.04	0.04
Prism layer near wall thickness, [m]	1E-04	5E-05
Base size of circular region around the receiver, [-]	10 % base size	10 % base size
Base size of the rectangular region along the wake, [-]	25 % base size	25 % base size
# of cells, [Mcells]	5.8	5.8
Time-step, [s]	0.1	0.05
Inner iterations, [-]	15	15

4.3.2 Receiver

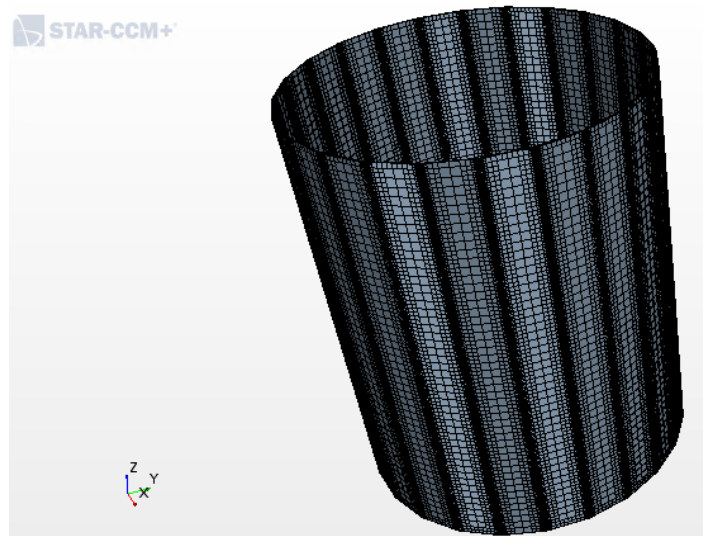
Concerning the molten salts region, the trimmed cell mesher has been adopted, providing an efficient and robust method of producing a high-quality grid for this geometry (see Fig. 39).

Aiming to solve mainly the energy equation, anisotropic mesh has been applied, refining the size along the direction normal to the flow of the molten salts.

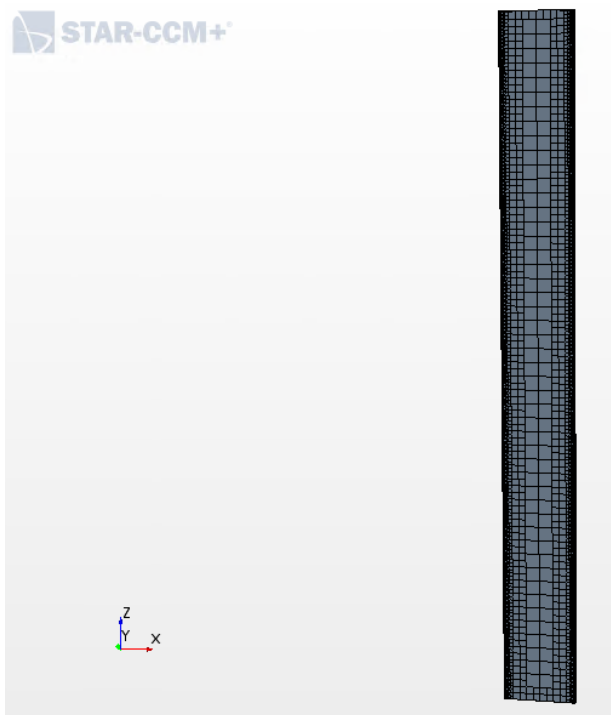
A summary of the initial mesh (on a single panel) is given in TABLE VII.

TABLE VII: INITIAL SPECIFICATIONS FOR THE INTERNAL FLOW 3-D MESH

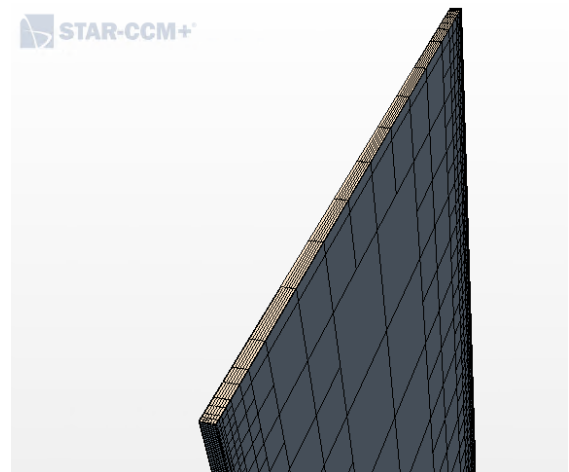
	SCENARIO #1	SCENARIO #2
Mesh type	Trimmed	Trimmed
Base size (along x), [m]	0.5	0.5
Base size (along y), [m]	2.5E-03	2.5E-03
Base size (along z), [m]	1.0	1.0
Target surface size, [-]	100 % base size	100 % base size
Minimum surface size, [-]	5 % base size	5 % base size
# of cells, [Mcells]	≈ 0.166	≈ 0.166
(total) # of cells, [Mcells]	≈ 3.98	≈ 3.98



(a)



(b)



(c)

Figure 39: Initial receiver mesh. (a) Whole receiver, (b) Zoom on a single panel, (c) Zoom on the inlet/outlet of the panel

4.4 Air

4.4.1 Verification

Two types of grid independence studies have been approached: one varying the number of prism layers and the other varying the base size; a time independence study has been provided too, concerning the # of inner iterations per time-step. For each different value of base size considered, a mesh diagnostic has been done because, even though a mesh is valid and the solution is successfully initialized with an appropriate space model, poor mesh quality can negatively affect the final solution.

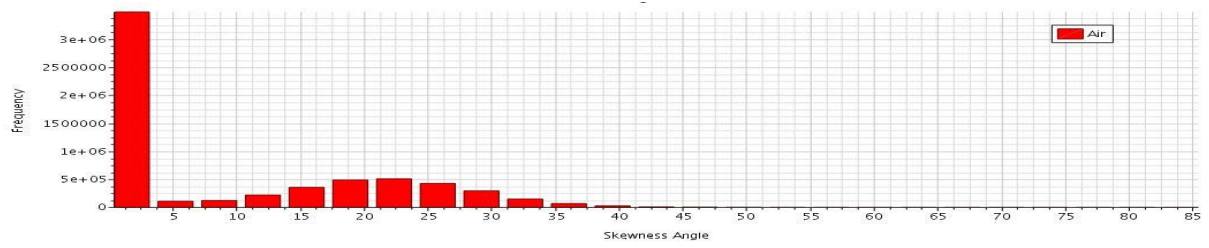
The quality measurements survey the same monitors of the two-dimensional case

- Skewness angle;
- Face validity;
- Volume change;
- Chevron quality indicator;

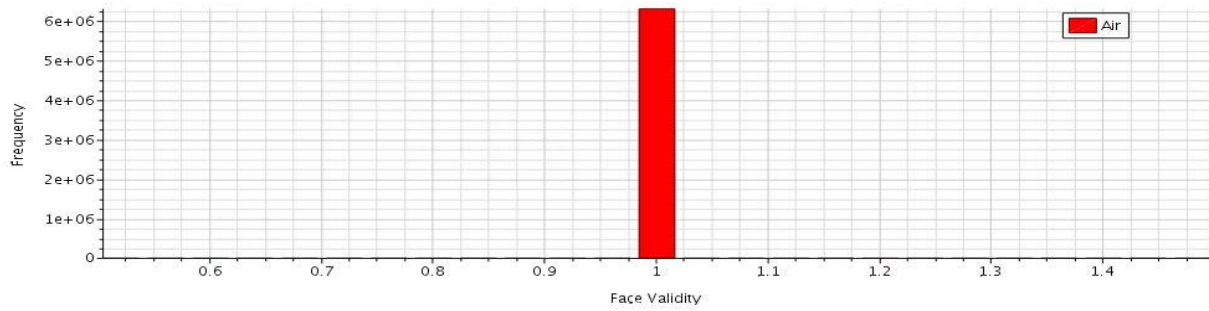
and, in addition:

- Cell quality: only defined for a three-dimensional mesh, a cell with a quality of 1.0 is considered perfect. Instead, a degenerate cell has a cell quality approaching zero. Depending on the physics that has been selected for the analysis, the cell quality of a cell can be low and still provide a valid solution. However, poor cell quality is likely to affect both the robustness and accuracy of the solution.

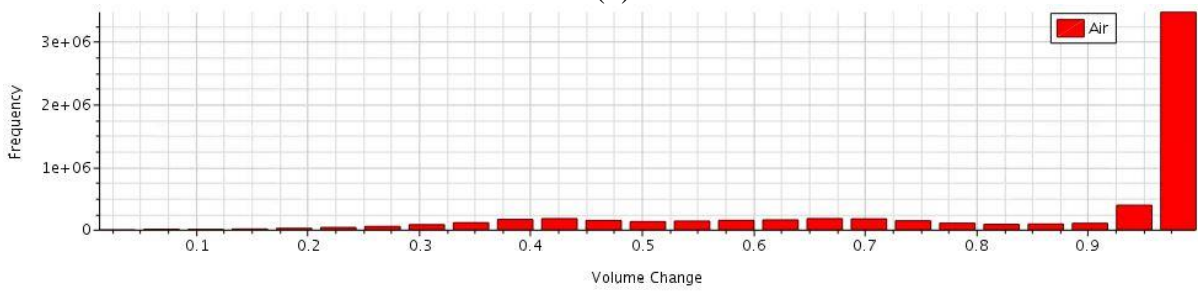
Each of these monitors has been plotted in a histogram plot, as Fig. 40 shows in the next page.



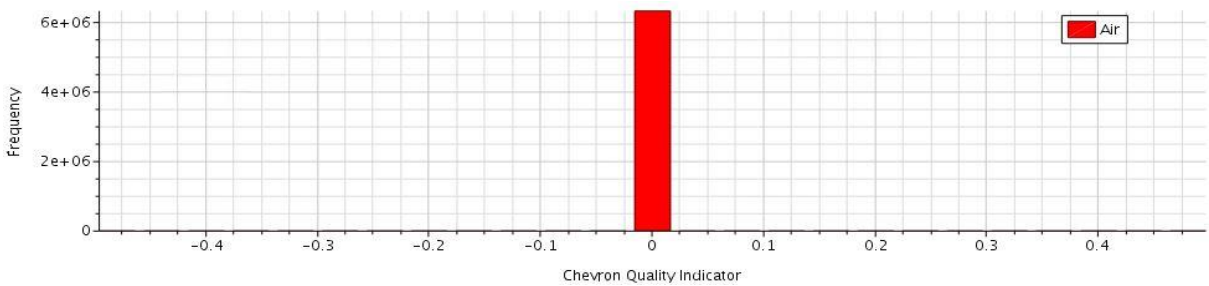
(a)



(b)



(c)



(d)



Figure 40: Air, 3-dimensional mesh quality measurements. (a) Skewness angle, (b) Face validity, (c) Volume change, (d) Chevron quality indicator (e) Cell quality

Before stopping the simulation to export data, a check on their reliability has been issued through the residuals and the drag coefficient. Once the simulation has been considered statistically stationary, the profile of the drag coefficient in that interval has been postprocessed with Excel, obtaining the time-averaged drag coefficient, and obtaining a plot through Matlab. The following convergence study has been developed for the SCENARIO #1 (simulating only the external flow, without any thermic load) because of more available experimental data.

The first grid independence study concerns the number of prism layers: maintaining constant the mesh specifications previously cited in TABLE VI and setting the same time-step of 0.1 s, only the number of prism layers has been modified, obtaining the time-averaged drag coefficient (see Fig. 41).

The result is that one with the green circle: 30 layers. The greater number of layers provides the same result, but it is too expensive for the three-dimensional study.

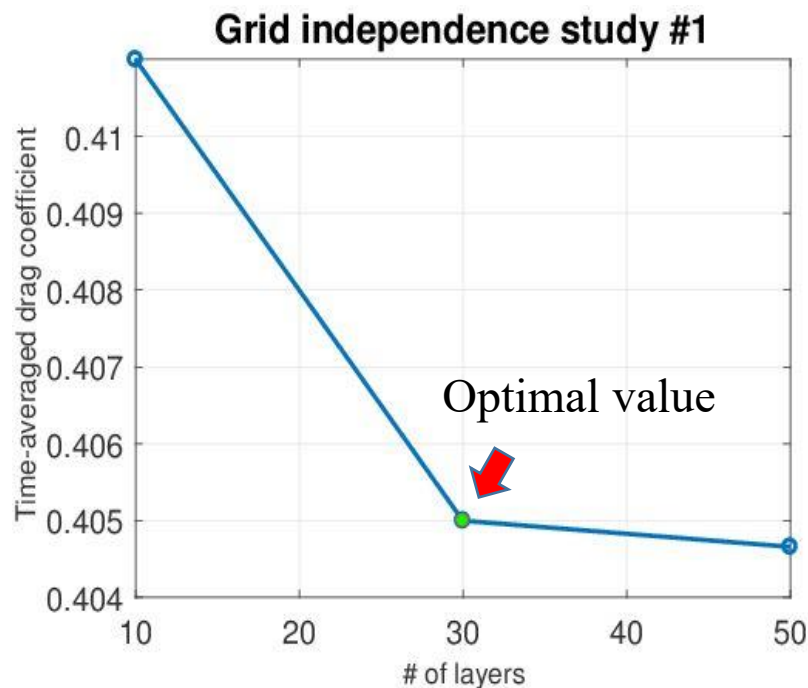
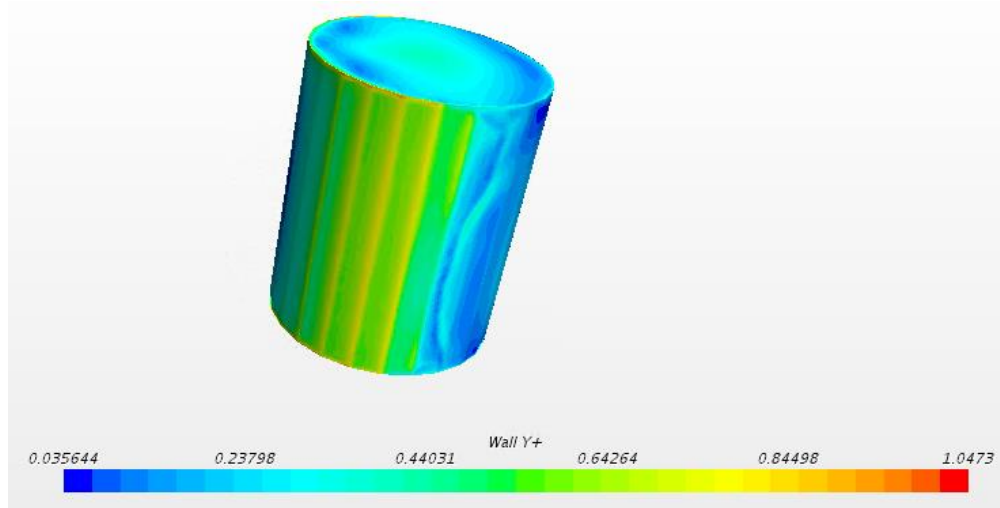
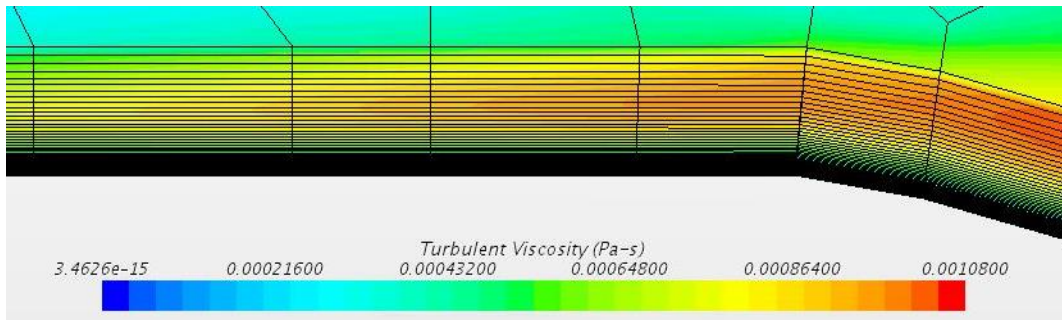


Figure 41: Air, 3-dimensional grid independence study – # of prism layers

Soon after this first step, it is possible to observe the flow details near wall (see Fig. 42): 2-dimensional criteria (about the wall- y^+ and turbulent viscosity) applied to the 3-dimensional case.



(a)



(b)

Figure 42: External flow field details (a) Wall- y^+ (b) Detail of the turbulent viscosity field within the prism layer region

The second grid independence study concerns the base size: fixing the optimal number of layers just obtained and maintaining constant all the other mesh specifications previously cited in TABLE VI, setting the optimal time-step obtained from the two-dimensional study, only the base size has been modified, obtaining the time-averaged drag coefficient.

Increasing the base size (with respect to 1.0), the jump between the last layer and the bulk becomes worse, giving poor and irregular results. On the other hand, decreasing the base size (with respect to 1.0) results in a too big computational cost (base size = 0.75 \rightarrow 13.42 Mcells). So, the base size has not been modified.

Finally, fixing the optimal number of layers and base size, and maintaining all the other mesh specifications of TABLE VI, only the number of inner iterations per time-step have been modified, providing a time independence study.

The three tested simulations (with 5, 10 and 15 inner iterations per time-step) shared:

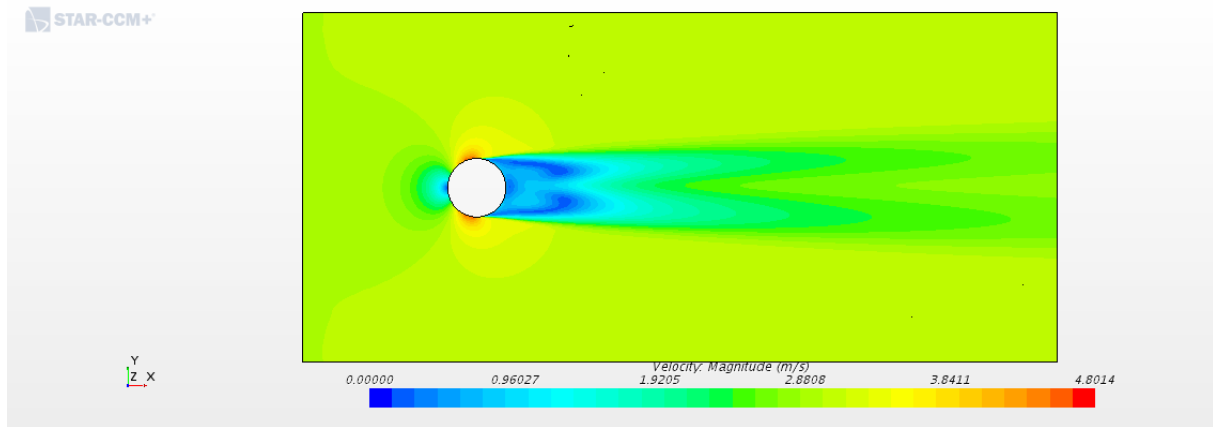
- the same flow field evolution
- the same time-averaged drag coefficient
- the same Δp (between point probes along the centerline)

and they reached convergence after 11000 iterations, approximately. Moreover, the simulation with 5 iterations showed few irregularities in the various monitors, thus I proceeded with the following optimal mesh for the air domain:

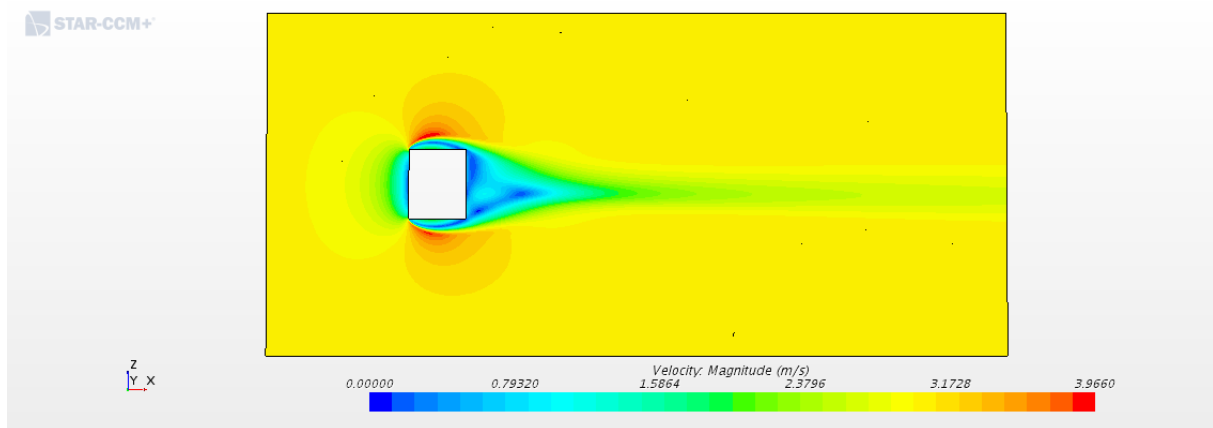
TABLE VIII: FINAL SPECIFICATIONS FOR THE EXTERNAL FLOW (WITH POLYGONAL CYLINDER) 3-D MESH

	SCENARIO #1
Mesh type	Polyhedral
Base size, [m]	1.0
Target surface size, [-]	100 % base size
Minimum surface size, [-]	5 % base size
Surface growth rate, [-]	1.05
# of prism layers, [-]	30
Prism layer total thickness, [m]	0.04
Prism layer near wall thickness, [m]	1E-04
Base size of circular region around the receiver, [-]	10 % base size
Base size of the rectangular region along the wake, [-]	25 % base size
# of cells, [Mcells]	5.8
Time-step, [s]	0.1
Inner iterations, [-]	10

The resulting flow field is shown in the figures below.



(a)



(b)

Figure 43: 3-dimensional velocity field of converged external flow. (a) xy plane (b) xz plane

The velocity field above shown is almost symmetric, but not entirely because of the high Re . The influence of the gravity is observed on the little wake shift downwards (see Fig. 43.b).

4.4.2 **Benchmark and validation**

As for the 2-dimensional analysis, DNS data are not available for this range of Re . However, data from other less computationally expensive numerical studies are available and it is possible to benchmark our results against their ones.

Comparing the time-averaged drag coefficient (for both scenarios), it seems to be in agreement (see Fig. 44) with numerical URANS data by Catalano et al. (2003), but slightly overpredict the C_D with respect to their 3-D LES numerical study.

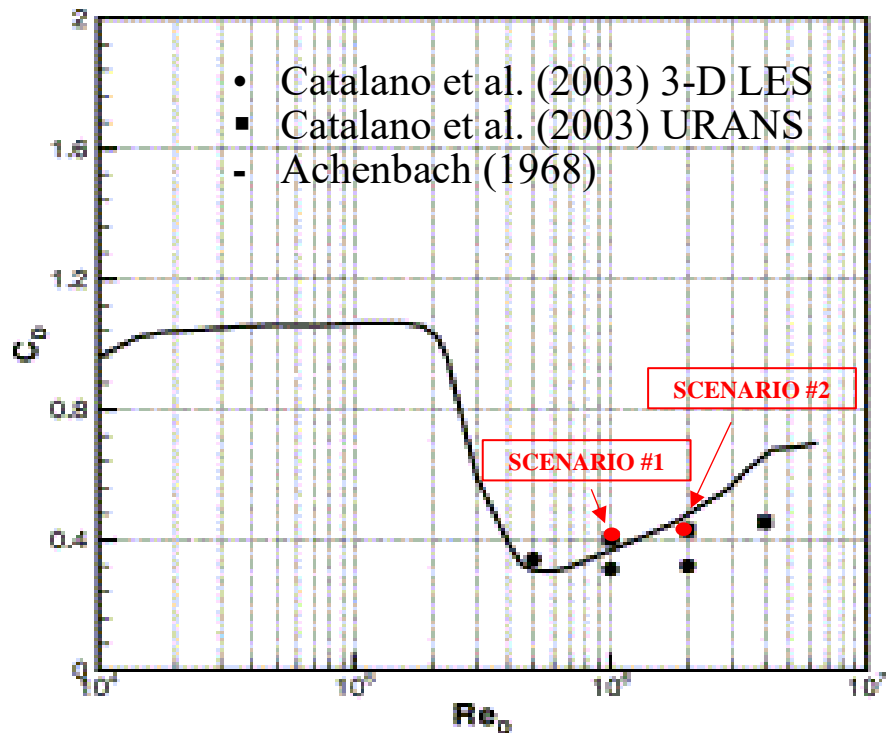


Figure 44: Benchmark of 3-dimensional results – only hydraulic, external flow (adapted from [15])

Moreover, it is possible to validate our results comparing them with experimental results (see Fig. 45). Always considering the time-averaged drag coefficient (for SCENARIO #1), it seems to be in agreement with the experimental data of Wieselberg (from Schlichting) and ESDU, which are the only ones to have made tests until Re useful for this comparison.

The SCENARIO #2 has not been simulated because of lack of experimental data.

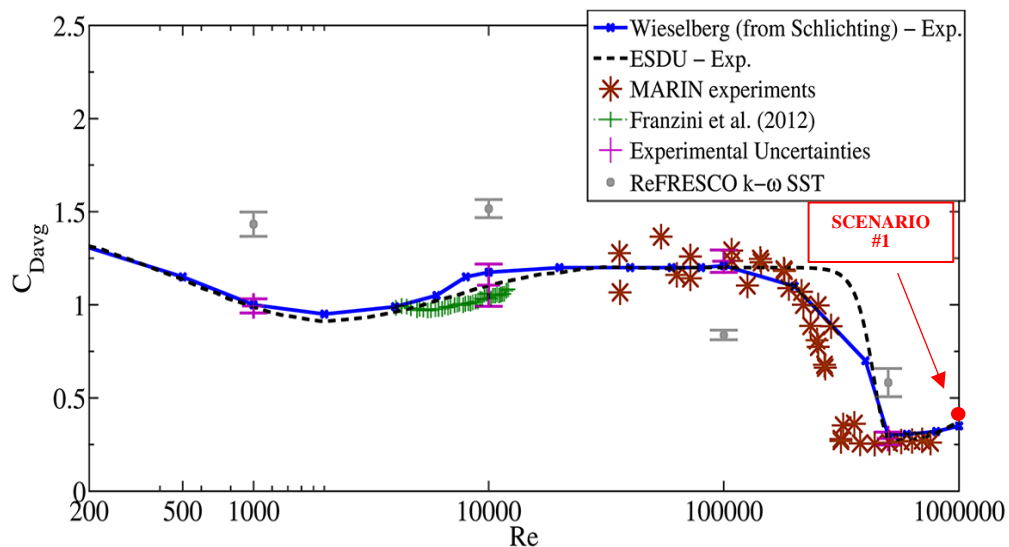


Figure 45: Validation of 3-dimensional results – only hydraulic, external flow (adapted from [38])

4.5 Receiver

4.5.1 Verification

Since the chosen mesh generator for the receiver is the anisotropic trimmed one, the grid independence study has been approached for all the three (x,y,z) directions: firstly, varying the base size along x, then along y and finally along z. For each different value of base size considered, a mesh diagnostic has been adopted, like all the previous studies.

The quality measurements survey the same monitors:

- Skewness angle;
- Face validity;
- Volume change;
- Chevron quality indicator;
- Cell quality.

Each of these monitors has been plotted in a histogram plot, as Fig. 46 shows in the next page.

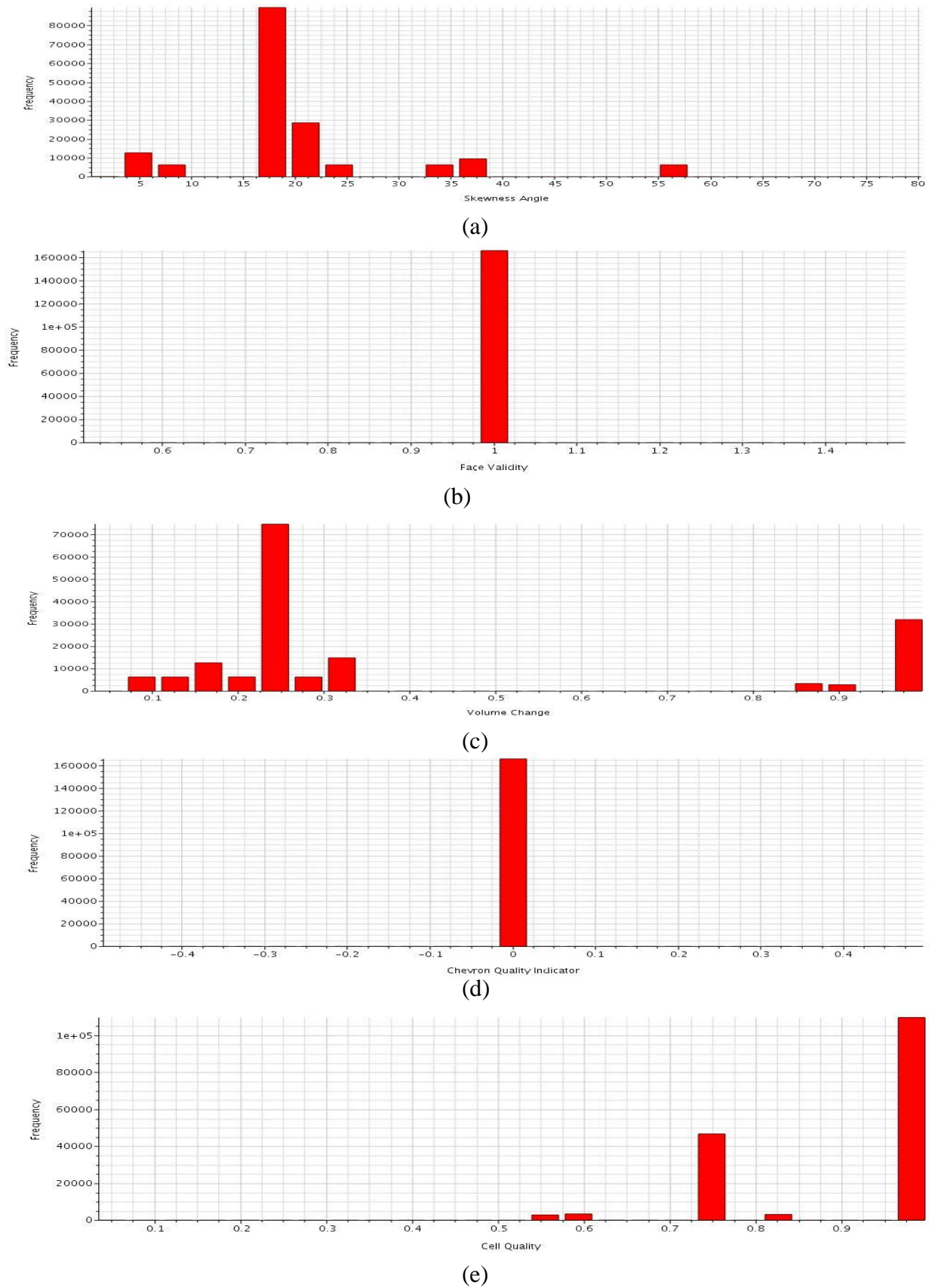


Figure 46: Receiver mesh quality measurements. (a) Skewness angle, (b) Face validity, (c) Volume change, (d) Chevron quality indicator (e) Cell quality

To reduce as much as possible the needed computational time, the grid independence study has been conducted on a single panel, since they share the same geometry.

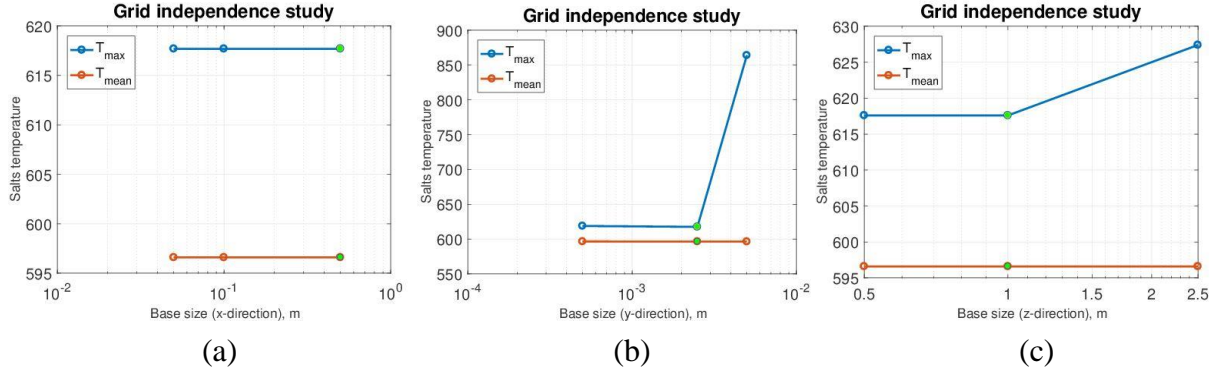


Figure 47: Receiver grid independence study – base size. (a) x-direction (b) y-direction (c) z-direction

Moreover, the simulations did not include the air surrounding, but only the receiver. A thermal condition of volumetric heat load within the channel has been imposed during all the simulations, not being coincident with the real case, but however useful to conduct the verification.

The mean and maximum T within the channel have been monitored (see Fig. 47), showing almost the same average T , but different maximum. Finally, the obtained final mesh coincided with the initial one (see TABLE VII).

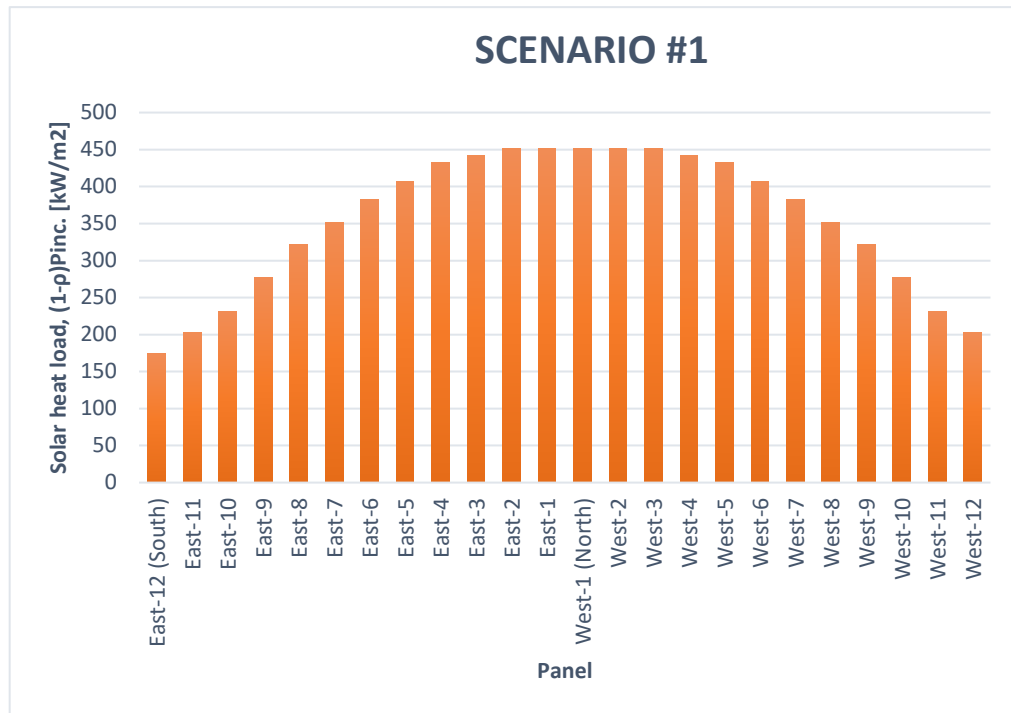
Being a particular case study, no benchmark or validation phase is available.

4.6 Case study

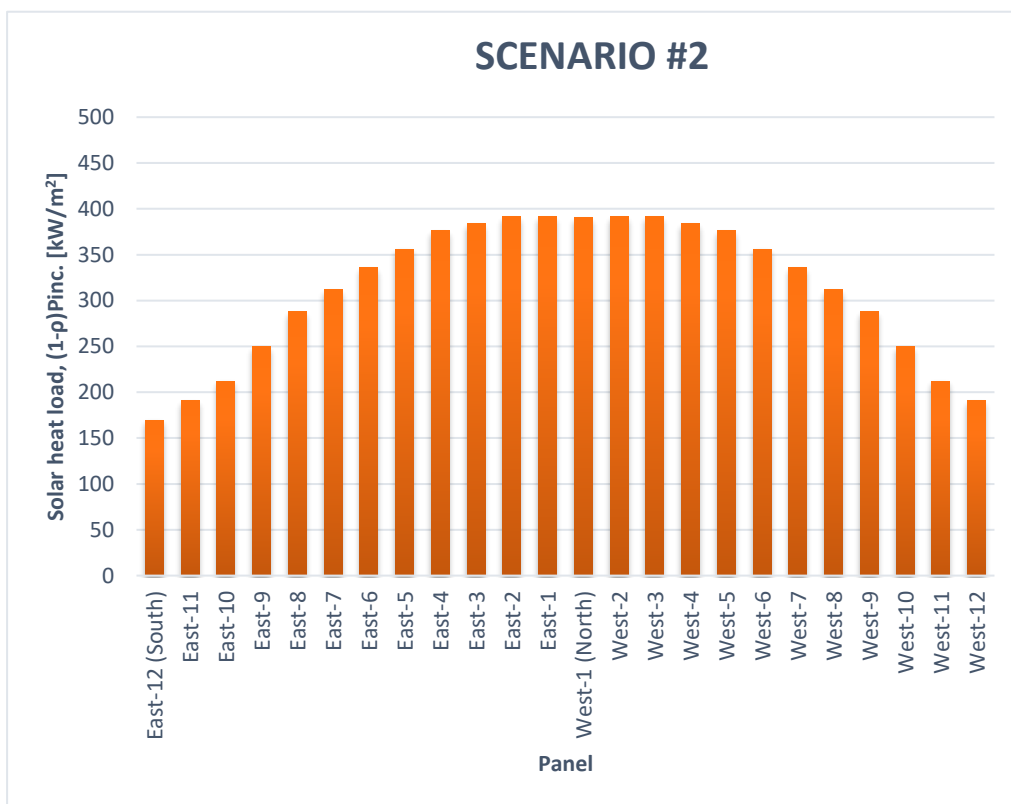
Coupling the molten salts within the receiver and the surrounding environment, both with the optimal meshes previously obtained, the surface solar heat loads provided by Sandia National Laboratory has been imposed as follow:

TABLE IX: INCIDENT RADIATIVE POWER ON RECEIVER SURFACE

	Scenario #1	Scenario #2
$P_{inc.}$, [MW]	≈ 37.1	≈ 30.8



(a)



(b)

Figure 48: Distribution of the radiative load (kW/m^2) on the receiver panels.
 (a) SCENARIO #1 (b) SCENARIO #2

Together with the following radiative properties of the external black Pyromark paint:

TABLE X: RADIATIVE PROPERTIES OF BLACK PYROMARK, EXTERNAL RECEIVER PAINT

$\varepsilon, [-]$	0.94
$\tau, [-]$	0
$\rho, [-]$	0.06

What is mainly expected is an asymmetric behavior (of air temperature and velocity around the receiver), because of the presence of both circuits' outlets in the southern receiver region: due to the highest molten salts' temperature there, that receiver region will be the hottest one, affecting the flow field.

4.6.1 Scenario #1

The converged air flow and temperature fields are shown in Fig. 49 and 50, respectively.

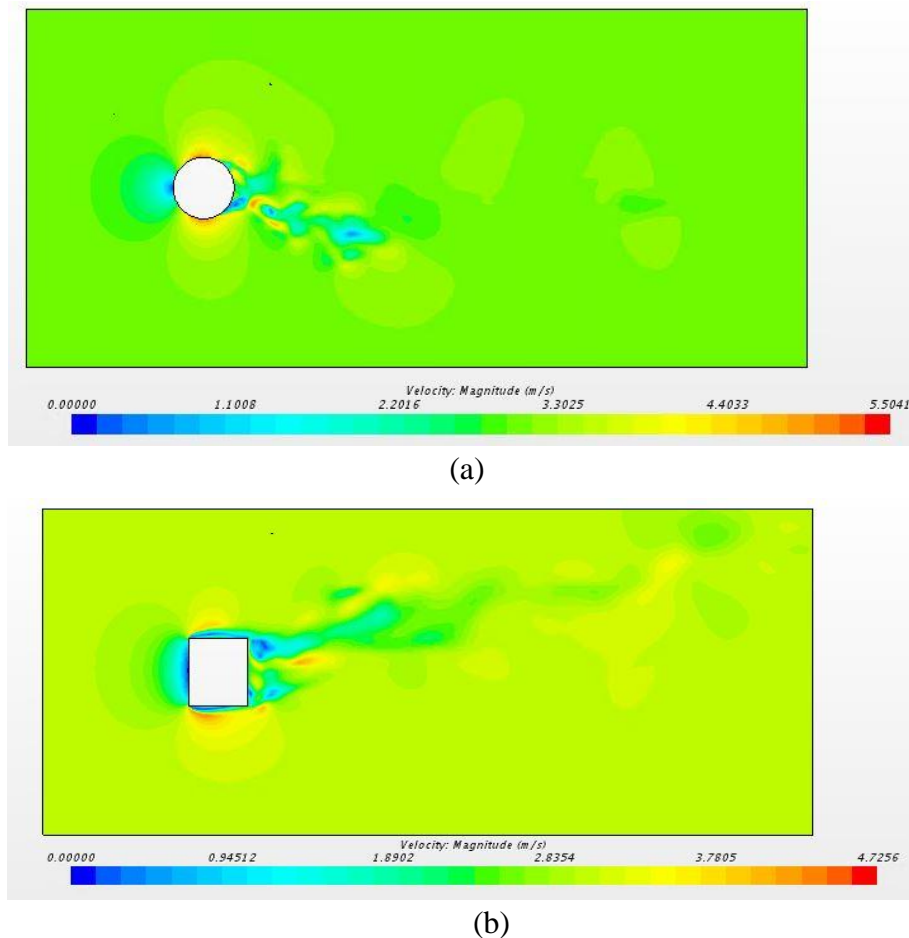


Figure 49: SCENARIO #1, air velocity flow field. (a) equatorial plane (b) vertical west-east plane, passing through the receiver center

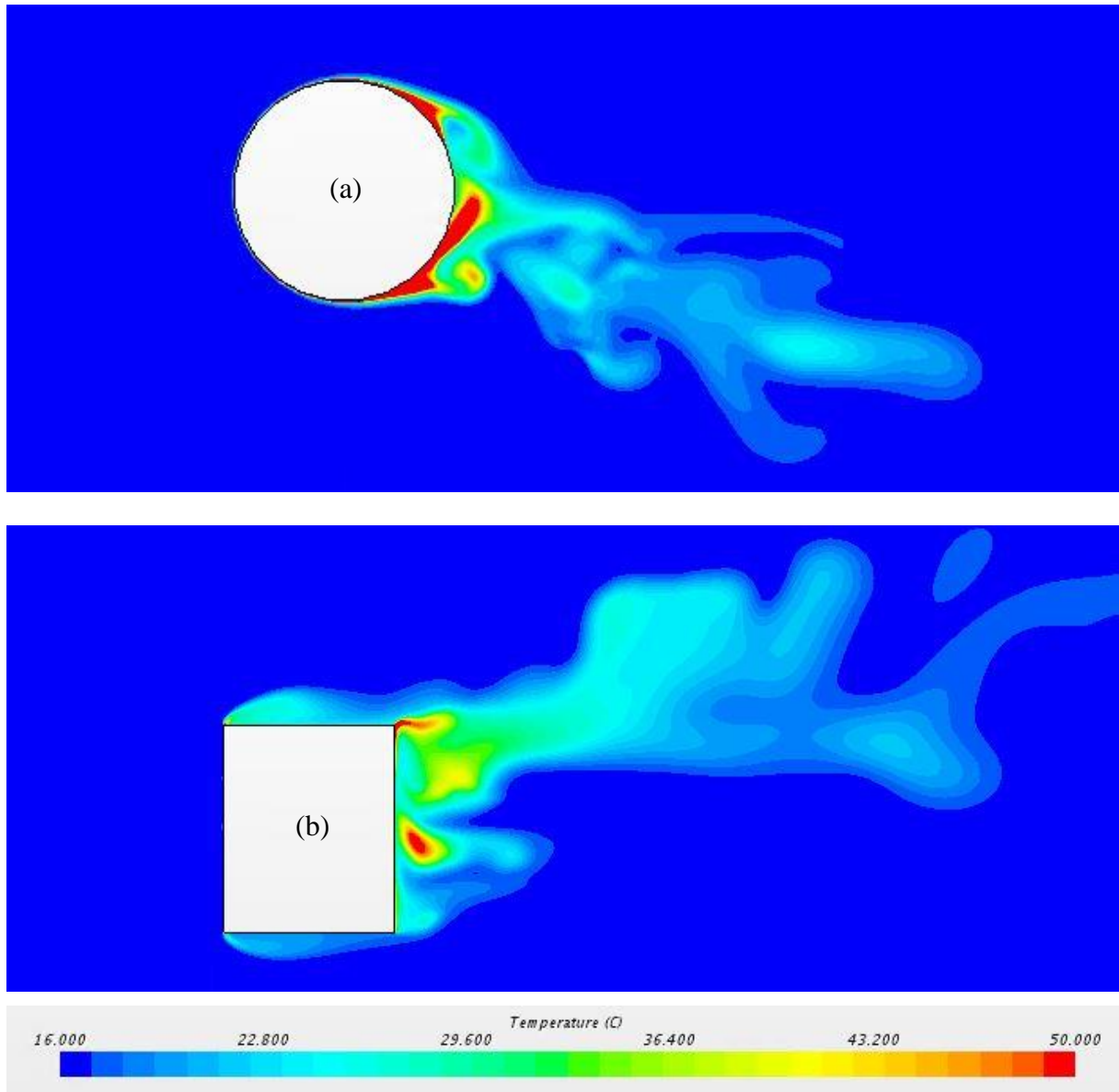


Figure 50: SCENARIO #1, air temperature map. (a) equatorial plane (b) vertical west-east plane, passing through the receiver center

Observing Fig. 49, it is possible to highlight the flow detachment on the sides of the receiver and both at the top and bottom of it.

On the equatorial plane (Fig. 49.a), the flow is not symmetric, possibly due to the physics which govern the phenomena at this high Reynolds number and, especially, for the high receiver superficial thermal gradient between northern and southern regions (see Fig. 51).

Looking at the vertical west-east plane (Fig. 49.b), the buoyancy takes part affecting the wake region, above all in the receiver upper zone.

Concerning the air temperature map of Fig. 50.a (where temperature above 50°C are represented as if they were equal to 50°C, in order to get a graphical appreciation of the gradients), the southern region is characterized by a higher temperature, with respect to the northern one, as previously forecast.

Looking at the vertical plane (Fig. 50.b, with the same graphical settings of Fig. 50.a), the buoyancy takes part affecting the wake region, above all in the receiver upper zone.

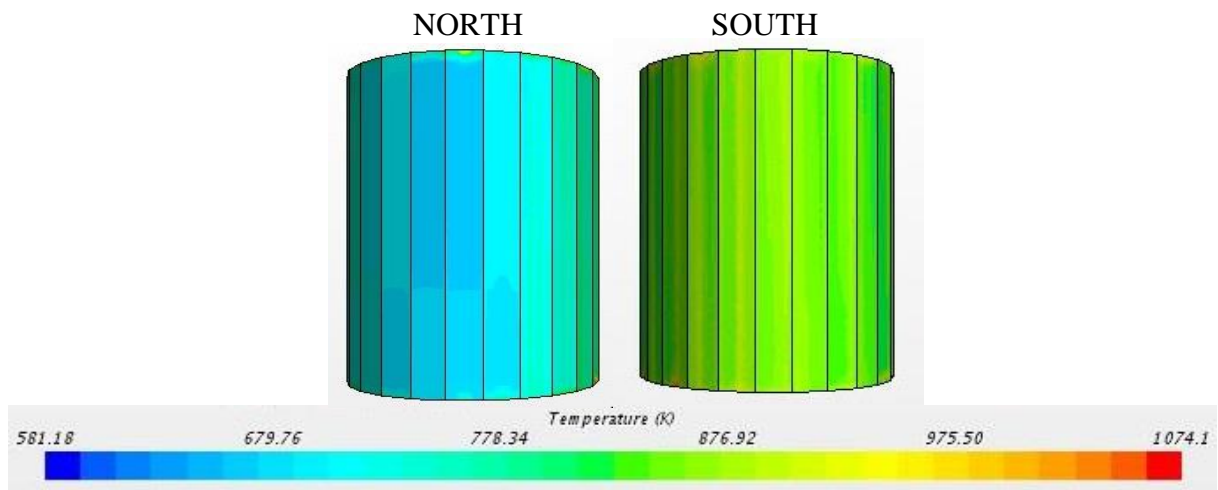
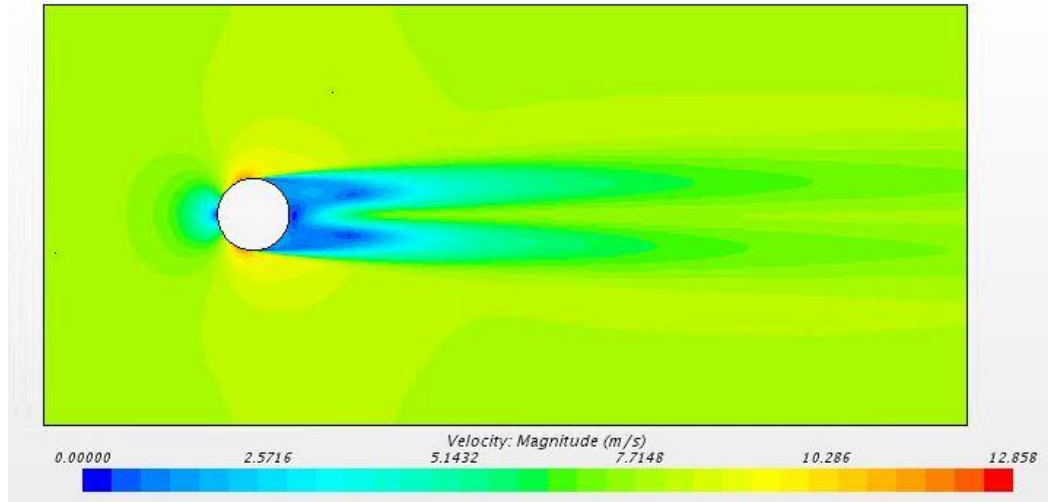


Figure 51: SCENARIO #1, receiver temperature map

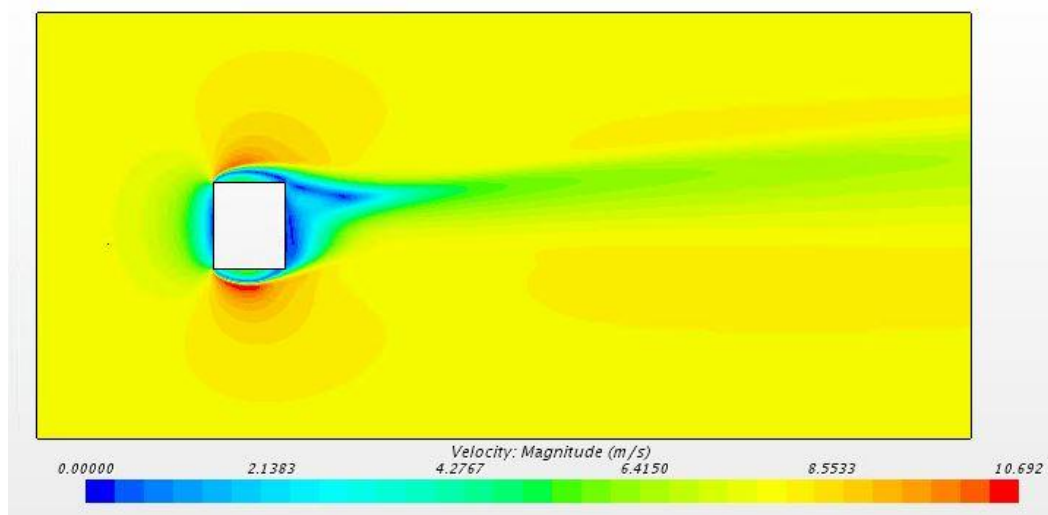
As it is possible to note, quite a high superficial thermal gradient (around 300°C) is present between northern and southern regions.

4.6.2 Scenario #2

The converged air flow and temperature fields are shown in Fig. 52 and 53, respectively.



(a)



(b)

Figure 52: SCENARIO #2, air velocity flow field. (a) equatorial plane (b) vertical west-east plane, passing through the receiver center

Observing Fig. 52, it is possible to note that there is no flow detachment on the sides, at the top and bottom of the receiver, because of the higher Re than the previous one.

On the equatorial plane (Fig. 52.a), the flow is almost symmetric downstream although the high receiver superficial thermal gradient between northern and southern regions (see Fig. 54).

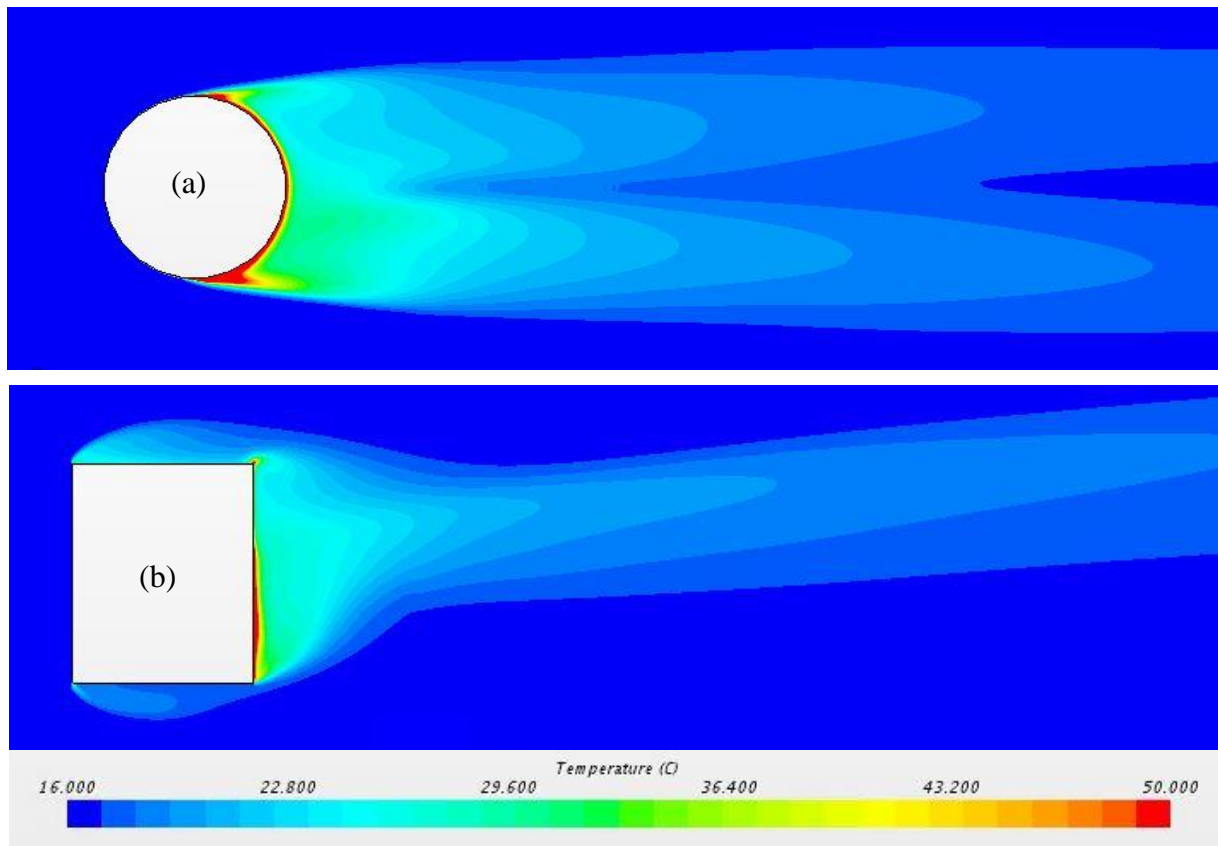


Figure 53: SCENARIO #2, air temperature map. (a) equatorial plane (b) vertical west-east plane, passing through the receiver center

Looking at the vertical west-east plane (Fig. 52.b), the buoyancy tends to lift the wake but, on the other hand, viscous ones preserve it.

Concerning the air temperature map of Fig. 53.a (where temperature above 50°C are represented as if they were equal to 50°C , in order to get a graphical appreciation of the gradients), slightly larger portion of southern region is characterized by a higher temperature, with respect to the northern one.

Looking at the vertical plane (Fig. 53.b, with the same graphical settings of Fig. 53.a), the buoyancy tends to lift the wake but, on the other hand, viscous ones preserve it.

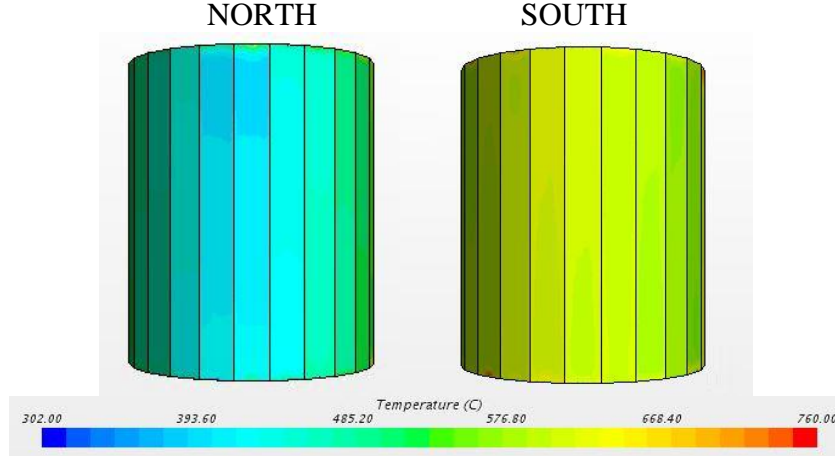


Figure 54: SCENARIO #2, receiver temperature map

As it is possible to note, quite a high superficial thermal gradient (around 310°C) is present between northern and southern regions.

4.7 Results

The convective heat losses determined from the various correlations are calculated as:

$$\bar{Q}_{loss}^{panels} = \bar{h} * A_{tot}^{panels} * (\bar{T}_s - T_{\infty}) \quad (3)$$

where:

- A_{tot}^{panels} is the total area of the side surface of the receiver in the model;
- \bar{T}_s is the receiver surface averaged temperature;

The convective heat transfer coefficient, h , has been evaluated considering two contributions: the natural convection one, h_{nc} , and the forced convection one, h_{fc} .

In presence of combined convection, both the contributions are weighted as follows [5]:

$$\bar{h}, \left[\frac{W}{m^2 \cdot K} \right] = (\bar{h}_{fc}^a + \bar{h}_{nc}^a)^{1/a} \quad (4)$$

where $a = 3.2$ [12].

To obtain the value of h_{fc} firstly, the forced convection Nusselt number, \overline{Nu}_{fc} , is evaluated as:

$$\overline{Nu}_{fc}, [-] = \frac{\bar{h}_{fc} * l}{k_f} \quad (5)$$

where the cylinder diameter represents the characteristic length and the air thermal conductivity, k_f , is evaluated at film temperature, $T_f = \frac{\bar{T}_s + T_{\infty}}{2}$, as suggested [12].

Nusselt number is a dimensionless group equal to the ratio of convective to conductive heat transfer across the boundary, and it depends on the surface roughness (only the Nu_{fc}): taking into account a smooth cylinder, the available correlations are:

$$\overline{Nu}_{fc}, [-] = 0.18 * Re^{0.63} \quad (6)$$

from [13], or the Churchill and Bernstein one:

$$\overline{Nu}_{fc}, [-] = 0.3 + 0.488 * Re^{0.5} \left[1.0 + \left(\frac{Re}{282000} \right)^{0.625} \right]^{0.8} \quad (7)$$

from [5]. Whatever is the chosen correlation, the Reynolds number has to be evaluated at the film temperature, T_f , as suggested [12].

On the other hand, to obtain the value of h_{nc} , the natural convection Nusselt number, \overline{Nu}_{nc} , is evaluated as:

$$\overline{Nu}_{nc}, [-] = \frac{\bar{h}_{nc} * l}{k_{\infty}} \quad (8)$$

where the cylinder height represents the characteristic length and the air thermal conductivity, k_{∞} , is evaluated at the free-stream temperature, as suggested [12], taking into account the effects of the variable properties. The value of \overline{Nu}_{nc} is obtained as follows:

$$\overline{Nu}_{nc}, [-] = 0.098 Gr^{\frac{1}{3}}_H \left(\frac{\bar{T}_s}{T_{\infty}} \right)^{-0.14} \quad (9)$$

In Fig. 55 it is possible to compare CFD converged simulation results with predictive correlations and with on-site, experimental measurements, respectively. The respective error bars are also reported:

- $\pm 50 \%$ is considered on \overline{Nu}_{fc} , as proposed [12];
- $\pm 40 \%$ is considered on \overline{Nu}_{nc} , as proposed [12];
- $\pm 40 \%$ is considered on the exponent a , as proposed [12];
- $\pm 20 \%$ is considered on the on-site, experimental measurements.

The experimental heat loss, evaluated as the difference between the radiative contribution and the molten salts enthalpy increase, comprising the radiative, convective and conductive contributions, is compared in Fig. 55.a/c with the total heat loss resulting from simulation,

including only the radiative and convective ones. Taking into account that the real conductive heat losses is appraised being between 0.5% and 1% of the incident power [14], that is ≈ 0.18 - 0.36 MW, CFD result well agree with on-site measurements, within the error bar, for both scenarios.

Then, convective heat loss obtained from correlations is compared with the computed one (equal to the surface integral of the heat flux from the receiver to the air, subtracted of the radiative part) in Fig. 55.b/d: CFD result well agree with the employed correlations, within the error bar, for both scenarios.

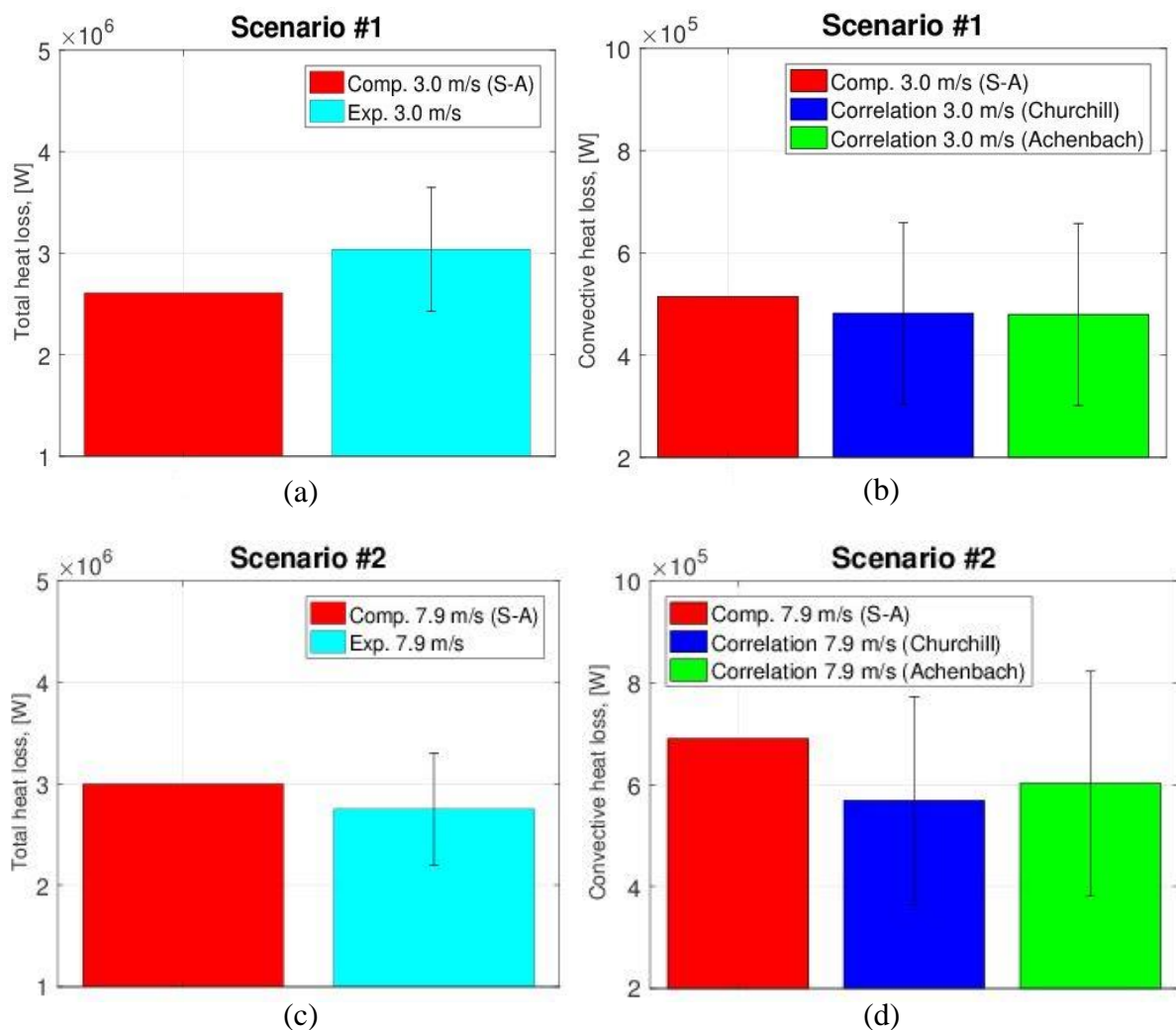


Figure 55: SCENARIO #1. (a) Experimental total heat loss, compared to total heat loss computed (b) Computed convective heat loss compared to prediction from correlations SCENARIO #2. (c) Experimental total heat loss, compared to total heat loss computed (d) Computed convective heat loss compared to prediction from correlations

The forced convection contribution is not so negligible in scenario #1 since \bar{h}_{fc} (≈ 4.5 W/(m²*K)) is only half of \bar{h}_{nc} (≈ 9 W/(m²*K)) and, combined with the power 3.2 in Eq. (4), the forced convection contribution results to be 10% of the total.

On the other hand, concerning scenario #2, forced convection contribution is comparable with natural on since \bar{h}_{fc} (≈ 9 W/(m²*K)) is almost equal to \bar{h}_{nc} (≈ 9 W/(m²*K)), confirming the convection type predicted at the beginning of the thesis.

CHAPTER 6

CONCLUSIONS AND PERSPECTIVE

Verification and validation of a geometrically simplified CFD model of the Solar Two central tower receiver have been discussed, being able to compute statistically stationary convective heat losses ($\approx 1.5\%$ and 2.2% of the total incident power on receiver surface) and total ones for scenario #1 and #2, respectively.

The obtained results are in agreement with those of employed correlations (for convective losses) and with those of on-site measurements (for total losses).

With a view to further developments, it should be interesting to realize a more exhaustive CFD model, considering the structure above and below the receiver, for both scenarios, influencing the thermo-hydraulic field from the absorber downwards along the wake.

APPENDICES

Appendix A

DRAG ON THE CYLINDER

A complete dissertation about forces acting on a cylinder in crossflow can be found in [6].

The force exerted by an object located in a fluid in motion has two components: in the direction of the flow and normal to it, respectively. The former is called drag, D : it is a combination of normal (due to pressure) and tangential (due to viscous effects) forces with respect to the flow direction:

$$D, [N] = \int dF_x = \int p \cos \theta dA + \int \tau_w \sin \theta dA = D_p + D_f \quad (\text{A.1})$$

where θ identifies the orientation of the surface.

Thus, the body shape, the distribution of τ_w and p along the surface are needed to integrate Eq. (A.1). Considering that it is often difficult to obtain those detailed information, the following dimensionless form is preferred:

$$C_D, [-] = \frac{D}{\frac{1}{2} \rho U_\infty^2 A} \quad (\text{A.2})$$

Where A is the characteristic area of the object, or rather, most often, the frontal area: it is the projected area seen by a person looking toward the object from a direction parallel to the upstream velocity, U_∞ .

As it is possible to observe, the drag force is composed of two components: the friction drag, D_f , and the pressure drag, D_p . The first one is that part of the drag directly due to the shear stress, τ_w , but not only: the orientation of the surface element (indicated by the factor $\sin \theta$) on which it acts is important too. The dimensionless form is the friction drag coefficient, C_{Df} :

$$C_{Df}, [-] = \frac{D_f}{\frac{1}{2} \rho U_\infty^2 A} = \frac{\int \tau_w \sin \theta dA}{\frac{1}{2} \rho U_\infty^2 A} \quad (\text{A.3})$$

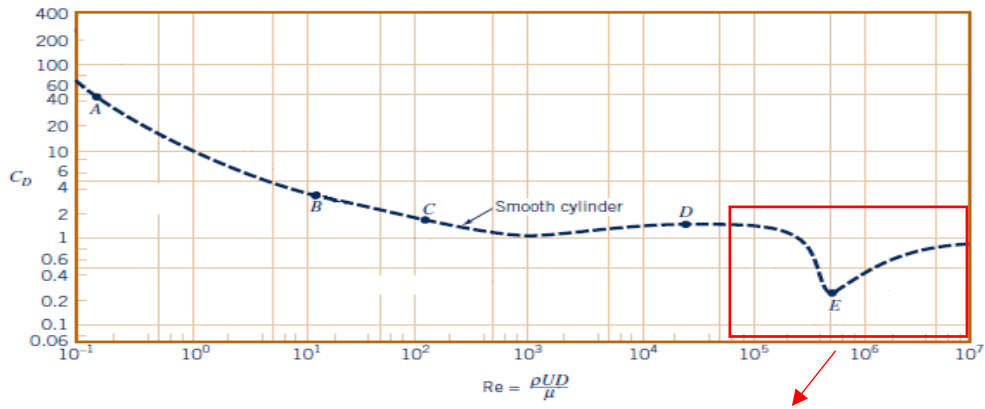
Its value is a function of Reynolds number, Re_l , and relative surface roughness, ε/l .

On the other hand, the pressure drag is that part directly due to the pressure (that is, to normal stresses), p , on the object, but not only: the orientation of the surface element (indicated

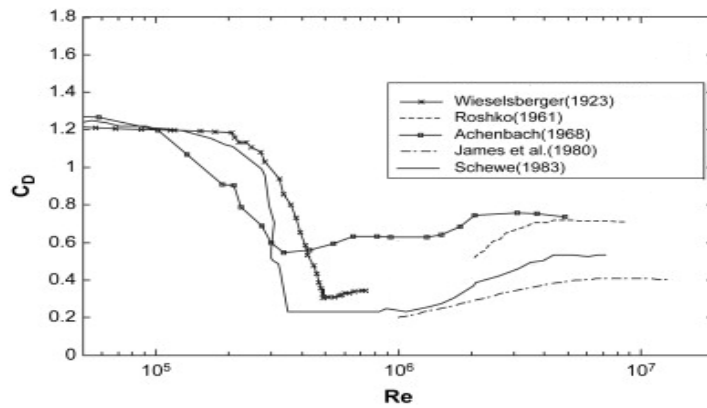
by the factor $\cos \theta$) on which the pressure force acts is important too. The dimensionless form is the pressure drag, C_{Dp} :

$$C_{p, [-]} = \frac{D_p}{\frac{1}{2} \rho U_\infty^2 A} = \frac{\int p \cos \theta dA}{\frac{1}{2} \rho U_\infty^2 A} = \frac{\int C_p \cos \theta dA}{A} \quad (\text{A.4})$$

Where $C_p = (p - p_\infty)/(\rho U_\infty^2/2)$ is the pressure coefficient: it is important to note that the intensity of the reference pressure does not influence directly the drag because the net pressure force on a body is zero if the pressure is constant on its surface. However, the pressure drag strongly depends on the shape of the object.



(a)



(b)

Figure 56: (a) Drag coefficient as a function of Reynolds number for a 2-dimensional, smooth circular cylinder (adapted from [6]), (b) Experimental references for drag coefficient in the turbulent region (adapted from [16])

The component of the force normal to the flow is called lift, L , and it is experienced only by those objects not symmetrical or those not producing a symmetrical flow field. It is defined as:

$$L, [N] = \int dF_y = - \int p \sin \theta dA + \int \tau_w \cos \theta dA \quad (A.5)$$

or, in dimensionless form:

$$C_L, [-] = \frac{L}{\frac{1}{2} \rho U_\infty^2 A} \quad (A.6)$$

We will focus only on the drag force.

The most important parameter on which the drag coefficient is dependent is the Reynolds number (see Figure 53.a): an abundance of such two-dimensional drag coefficient data (in the turbulent region, above all) is available in literature (such as [15], [9] or [17]) and the figure below (Figure 53.b) is an example.

At low Reynolds number (see point A in Figure 19.a), there is a balance between viscous and pressure forces: the drag on the cylinder is expected to be function of the free-stream velocity, U_∞ , the diameter, D , and the dynamic viscosity, μ . Thus:

$$D, [N] = f(U_\infty, D, \mu) \quad (A.7)$$

and, from dimensional analysis:

$$D, [N] = C \mu D U_\infty \quad (A.8)$$

with C being a constant depending on the shape of the body; for circular cylinder, $C \cong 3$. In dimensionless form:

$$C_D, [-] = \frac{D}{\frac{1}{2} \rho U_\infty^2 A} = \frac{2C \mu D U_\infty}{\frac{1}{2} \rho U_\infty^2 A} = 2C \frac{\mu}{\rho U_\infty D} = \frac{2C}{Re} \quad (A.9)$$

At moderate Reynolds number, the drag coefficient starts to decrease with Reynolds number (see point B and C of Fig. 19.a) with a law different from the previous one and, at $Re = 10^3$, the C_D value becomes constant, until $Re = 10^5$. As mentioned before, at this Reynolds number, the boundary layer starts being turbulent and the drag force experiences a sudden decrease: the turbulent boundary layer travel further along the cylinder surface into adverse pressure gradient on the backside of the cylinder before separation occurs. The consequence is a smaller pressure drag. As soon as the boundary layer is totally turbulent, C_D increases again.

Appendix B

HEAT LOSSES UNDERGONE BY THE CYLINDER

A complete dissertation about heat losses can be found in [5].

An object located in a fluid in motion is subjected to two kind of thermal losses: radiative and convective.

Assuming a nonparticipating medium (i.e., no effect on the transfer of radiation between surfaces), the radiative exchange between two or more surfaces depends strongly on the surface geometries and orientations, as well as on their radiative properties and temperatures. Other important assumption made for this work is to neglect the dependence of the radiative properties from temperature, orientations and wavelength.

Defining the irradiation quantity, G , as the rate at which radiation is incident upon a surface per unit are [W/m^2], three main phenomena can occur (see Fig. 54):

- Reflection: a fraction of the irradiation is reflected by the surface, characterized by the dimensionless quantity ρ (reflectance):

$$\rho, [-] = \frac{G_{ref}}{G} \quad (\text{B.1})$$

- Absorption: a fraction of the irradiation is absorbed by the surface, characterized by the dimensionless quantity α (absorptance):

$$\alpha, [-] = \frac{G_{abs}}{G} \quad (\text{B.2})$$

- Transmission: a fraction of the irradiation is transmitted by the surface, characterized by the dimensionless quantity τ (transmittance):

$$\tau, [-] = \frac{G_{tr}}{G} \quad (\text{B.3})$$

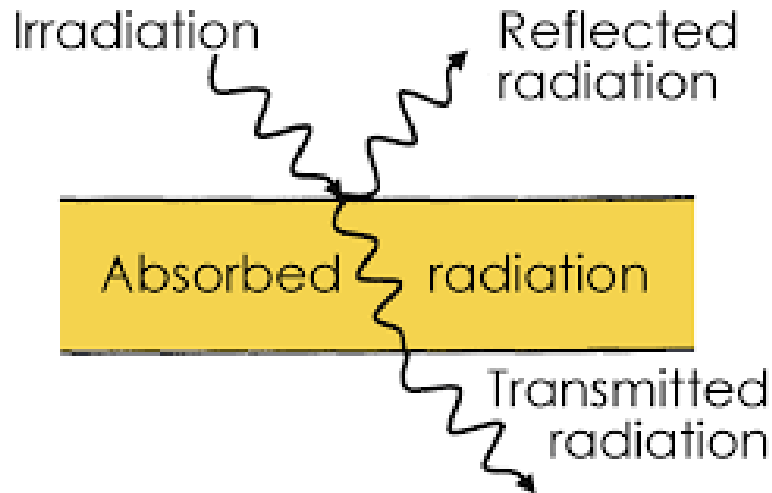


Figure 57: Interactions of radiation with semitransparent medium [37]

Approximating surfaces as blackbodies, the radiative exchange is simplified because there is no more the reflected and transmitted component, but all the incident radiation is absorbed and emitted. As blackbody, the emission follows the Stefan-Boltzmann law:

$$E_b, \left[\frac{W}{m^2} \right] = \sigma T^4 \quad (B.4)$$

where the Stefan-Boltzmann constant, σ , is equal to $5.670E-8 \text{ Wm}^2/\text{K}^4$.

Discussing of radiative exchange between surfaces, it is mandatory to introduce the concept of shape factor (or view factor, see Fig. 55), F_{ij} , defined as the fraction of the radiation leaving surface i that is intercepted by surface j :

$$F_{ij}, [-] = \frac{1}{A_i} \int_{A_i} \int_{A_j} \frac{\cos \theta_i \cos \theta_j}{\pi R^2} dA_i dA_j \quad (B.5)$$

Where:

- A_i and A_j are arbitrarily oriented surfaces
- θ_i and θ_j are polar angles formed by the line of length R , which connects the two surfaces.

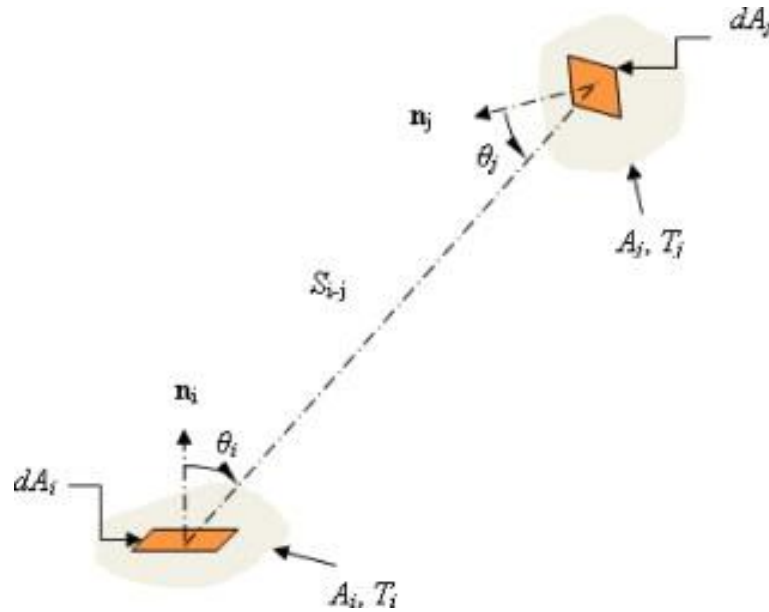


Figure 58: View factor associated with radiation exchange between elemental surfaces of area dA_i and dA_j [36]

Relationships which characterize the view factors are the reciprocity relation:

$$A_i F_{ij} = A_j F_{ji} \quad (\text{B.6})$$

and the summation rule:

$$\sum_{j=1}^N F_{ij} = 1 \quad (\text{B.7})$$

Thus, having N surfaces maintained at different temperatures, the net transfer of radiation from surface i due to exchange with the remaining surfaces may be expressed as:

$$q_i, [W] = \sum_{j=1}^N A_i F_{ij} \sigma (T_i^4 - T_j^4) \quad (\text{B.8})$$

On the other hand, the convective exchange can be subdivided in:

- Natural convection exchange: originating when a body force acts on a fluid in which there are density gradients (commonly due to temperature gradients), producing a buoyancy force, which induces free convection currents;
- Forced convection exchange: originating from an external forcing condition (like a fan or a pump), combined with the presence of a temperature gradient.

To determine which kind of convection is predominant, two dimensionless group are needed: the Reynolds and Grashof numbers, already discussed in the previous chapter.

If we consider an object of arbitrary shape, with a certain surface A_s at temperature T_s , submerged in a fluid with a certain velocity, V , and temperature, $T_\infty \neq T_s$, convection will occur. The total heat transfer rate, q , is expressed as:

$$q, [W] = (T_s - T_\infty) \int_{A_s} h dA_s = \bar{h} A_s (T_s - T_\infty) \quad (\text{B.9})$$

Where h and \bar{h} , $[W/m^2/K]$, are the local and average convection coefficient, respectively.

Depending on the flow regime, laminar or turbulent, it is possible to obtain the convective heat transfer coefficient by means of exact analytical solutions or experimental correlations about the Nusselt number, Nu . It is a dimensionless group defined as:

$$Nu = \frac{hL}{k_f} \quad (\text{B.10})$$

or:

$$\overline{Nu} = \frac{\bar{h}L}{k_f} \quad (\text{B.11})$$

which provides a measure of the convection heat transfer occurring at the surface.

Appendix C

UNSTEADY REYNOLDS-AVERAGE NAVIER-STOKES HEAT LOSSES UNDERGONE BY THE CYLINDER

A complete dissertation about URANS can be found in [18].

Within the expression of URANS, the central quantity that has to be modeled is the Reynolds stress tensor $\overline{u'_i u'_j}$, that is a symmetric positive defined matrix:

$$R = \begin{pmatrix} \overline{u'_1 u'_1} & \overline{u'_1 u'_2} & \overline{u'_1 u'_3} \\ \overline{u'_2 u'_1} & \overline{u'_2 u'_2} & \overline{u'_2 u'_3} \\ \overline{u'_3 u'_1} & \overline{u'_3 u'_2} & \overline{u'_3 u'_3} \end{pmatrix} \quad (C.1)$$

On-diagonal terms represent the normal stress, whereas the off-diagonal terms represent the shear stresses.

Now, the turbulent kinetic energy, k , and the anisotropic component of Reynold stresses, a_{ij} , are defined as follows:

$$k = \frac{1}{2} \overline{u'_i u'_i} = \frac{1}{2} (\overline{u'^2_1} + \overline{u'^2_2} + \overline{u'^2_3}) = \frac{1}{2} Tr(R) \quad (C.2)$$

$$a_{ij} = \overline{u'_i u'_j} - \frac{2}{3} k \delta_{ij} \quad (C.3)$$

So:

$$\overline{u'_i u'_j} = a_{ij} + \frac{2}{3} k \delta_{ij} = \underbrace{\begin{pmatrix} \overline{u'^2_1} - \frac{2}{3}k & \overline{u'_1 u'_2} & \overline{u'_1 u'_3} \\ \overline{u'_2 u'_1} & \overline{u'^2_2} - \frac{2}{3}k & \overline{u'_2 u'_3} \\ \overline{u'_3 u'_1} & \overline{u'_3 u'_2} & \overline{u'^2_3} - \frac{2}{3}k \end{pmatrix}}_{\text{anisotropic term}} + \underbrace{\begin{pmatrix} \frac{2}{3}k & 0 & 0 \\ 0 & \frac{2}{3}k & 0 \\ 0 & 0 & \frac{2}{3}k \end{pmatrix}}_{\text{isotropic term}} \quad (C.4)$$

Therefore, the final goal is to model the anisotropic part only. It is possible to rewrite:

$$\rho \frac{\partial \overline{u'_i u'_j}}{\partial x_j} + \frac{\partial \bar{p}}{\partial x_i} = \rho \frac{\partial a_{ij}}{\partial x_j} + \frac{\partial \left(\bar{p} + \frac{2}{3} \rho k \right)}{\partial x_i} \quad (C.5)$$

and, substituting in the original expression of URANS:

$$\rho \frac{\partial \bar{U}_i}{\partial t} + \rho \bar{U}_j \frac{\partial \bar{U}_i}{\partial x_j} = \rho g_i + \frac{\partial}{\partial x_j} \left(-\rho a_{ij} + 2\rho v \bar{S}_{ij} - \left(\bar{p} + \frac{2}{3} \rho k \right) \delta_{ij} \right) \quad (C.6)$$

A widely-used model in URANS is based on Bussinesque hypothesis where the anisotropic tensor, a_{ij} , is modeled with an eddy viscosity, v_T ,

$$-\rho a_{ij} = -\rho \overline{u'_i u'_j} + \frac{2}{3} \rho k \delta_{ij} = \rho v_T \left(\frac{\partial U_i}{\partial x_j} + \frac{\partial U_j}{\partial x_i} \right) = 2\rho v_T \bar{S}_{ij} \quad (C.7)$$

Thus, defining the effective viscosity as:

$$v_{eff.}(x, t) = v + v_T(x, t) \quad (C.8)$$

Eq. (C.6) can be rewritten as follows:

$$\frac{\bar{D}}{\bar{D}t} \bar{U}_i = g_i + \frac{\partial}{\partial x_j} \left[v_{eff.} \left(\frac{\partial}{\partial x_j} \bar{U}_i + \frac{\partial}{\partial x_i} \bar{U}_j \right) \right] - \frac{1}{\rho} \frac{\partial}{\partial x_i} \left(\bar{p} + \frac{2}{3} \rho k \right) \quad (C.9)$$

In doing so, the modelling effort has been moved from the anisotropic component of Reynolds stresses to the turbulent viscosity, v_T . Various approaches can be used:

- the uniform viscosity model: its applicability is extremely limited;

or, by dimensional analysis, writing $v_T = l^* \cdot u^*$ (with l^* being a length and u^* being a velocity):

- the mixing length model: specifying $l^* = l_m$ (i.e., the mixing length), and $u^* = l_m \frac{\partial \bar{U}}{\partial y}$, yields $v_T = l_m^2 \cdot \left| \frac{\partial \bar{U}}{\partial y} \right|$. It is still quite incomplete because this model requires the presence of a main flow gradient (for example, it does not work for decaying grid turbulence) and the mixing length, l_m , changes with the geometry of the flow and it should be specified each time.

Kolmogorov and Prandtl suggested another expression of the velocity, u^* , in order to overcome the limitation of the previous model, that is:

$$u^* = ck^{1/2} \quad (C.10)$$

with c being a constant and, with $l^* = l_m$:

$$v_T = ck^{1/2} l_m \quad (C.11)$$

A model transport equation for k (one-equation model), modelling k as follows:

$$\begin{aligned}
\frac{\bar{D}k}{\bar{D}t} = & \underbrace{-\frac{\partial}{\partial x_j} \left(\frac{1}{2} \overline{u'_i u'_i u'_j} \right) - \frac{1}{\rho} \frac{\partial \overline{u'_i p}}{\partial x_j}}_{\text{Transport term, } T} + \underbrace{v \frac{\partial^2 k}{\partial x_j^2}}_{\text{Production term, } P} - \underbrace{\overline{u'_i u'_j} \frac{\partial \bar{U}_i}{\partial x_j} - v \overline{\left(\frac{\partial u'_i}{\partial x_j} \right)^2}}_{\text{Dissipation term, } \varepsilon} = -\nabla \cdot T + P - \varepsilon
\end{aligned} \tag{C.12}$$

The transport and dissipation terms are in unclosed form; thus, they should be modelled. At high Re, $\varepsilon \sim u_0^3/l_0$, with u_0 and l_0 being the velocity and lengthscale of the energy-containing motions, respectively. Based on dimensional arguments, we have:

$$\varepsilon = c_D \frac{(c^{1/2})^3}{l_m} \tag{C.13}$$

where c_D is a model constant.

Combining Eqs. (C.11) and (C.13), yields:

$$v_T = c \cdot c_D \frac{k^2}{\varepsilon} \tag{C.14}$$

The transport term is modelled with a gradient-diffusion hypothesis:

$$T = -\frac{v_T}{\sigma_k} \nabla k \tag{C.15}$$

where σ_k is the turbulent Prandtl number, usually set to 1. Therefore, it is possible to finally rewrite the model transport equation for k as:

$$\frac{\bar{D}k}{\bar{D}t} = \nabla \cdot \left(\frac{v_T}{\sigma_k} \nabla k \right) + P - \varepsilon \tag{C.16}$$

To resume, the procedure amounts to:

- specify the mixing length, l_m ;
- solve the model transfer equation for $k(x, t)$;
- obtain the turbulent viscosity, v_T , by Eq. (36);
- obtain the Reynolds stresses by Eq. (29);
- solve the URANS.

The greatest drawback of the model remains: the mixing length, l_m , must be specified.

To overcome this inconvenient, various more advanced model have been introduced, such as Spalart-Allmaras (a one-equation model) or k- ε , k- ω (i.e., two equation models, where k is taken as one of the variables, but different are the choices for the second) and just a pair of them will be analyzed for the purpose of this thesis.

C.1 The Spalart-Allmaras turbulence model

This one-equation model solves a single model transport equation for the kinematic eddy turbulent viscosity, ν_T , and it was initially elaborated for aerospace application [8]. Later, it proved to give good results in applications with boundary layers subjected to separation and to adverse pressure gradient and with turbomachines.

Being a one-equation model for ν_T , it represents the lowest level at which a model can be complete: if the accuracy were the main standard of judgement for selecting the model to use, the choice would tend to models with a higher level of representation; however, a trade-off between cost and ease of use is important in CFD.

The model equation is:

$$\frac{\bar{D}\nu_T}{\bar{D}t} = \nabla \cdot \left(\frac{\nu_T}{\sigma_\nu} \nabla \nu_T \right) + S_\nu \quad (\text{C.17})$$

Where σ_ν is a constant and S_ν is a user-defined source term, depending on the molecular and turbulent viscosity, ν and ν_T , the turbulent viscosity gradient, $|\nabla \nu_T|$, the distance to the nearest wall, l_w , and on the rate of rotation (or mean vorticity), Ω_{ij} .

This model is not suited to application involving jet-like free-shear region: mainly because it is unable to account for the decay of ν_T in isotropic turbulence (where $\overline{u_1'^2} = \overline{u_2'^2} = \overline{u_3'^2}$), implying that, in homogeneous turbulence (where $\frac{\partial \overline{u_i' u_j'}}{\partial x_j} = 0$ and $\frac{\partial \overline{u_i' p'}}{\partial x_j} = 0$), ν_T is unaffected by irrotational mean straining.

C.2 The k- ω turbulence model

This is one of the most common two-equation model, solving two model transport equations: Eq. (C.16) for the turbulent kinetic energy, k , and an additional one for ω , which is the specific rate of dissipation of k , defined as:

$$\omega = \frac{\varepsilon}{k} \quad (\text{C.18})$$

Forming three dimensional quantities:

$$(\text{lengthscale}) L = \frac{k^{3/2}}{\varepsilon} = \frac{k^{1/2}}{\omega} \quad (\text{C.19})$$

$$(\text{timescale}) \tau = \frac{k}{\varepsilon} = \frac{1}{\omega} \quad (\text{C.20})$$

$$v_T = \frac{k^2}{\varepsilon} = \frac{k}{\omega} \quad (\text{C.21})$$

it is possible to complete this two-equation model, without being dependent on flow specifications such as the mixing length, l_m , anymore.

As for the k- ε model, the exact equation for ω is not derived but it is best viewed as being entirely empirical:

$$\frac{\bar{D}\omega}{\bar{D}t} = \nabla \cdot \left(\frac{v_T}{\sigma_\omega} \nabla \omega \right) + C_{\omega 1} \frac{P\omega}{k} - C_{\omega 2} \omega^2 \quad (\text{C.22})$$

where σ_ω , $C_{\omega 1}$ and $C_{\omega 2}$ are empirical constants.

The above formulation is the original model developed by Wilcox and others [19]. It is well suited to boundary-layer flows, particularly in the treatment of the viscous near-wall region and of the effects of the streamwise pressure gradients. However, the treatment of non-turbulent free-stream boundaries (where $\omega = 0$) can be cumbersome because a non-physical boundary condition would be imposed about an ω , making the flow very sensitive to the specified value.

A proper solution to this problem has been developed by Menter [20], proposing a version of k- ω that could yield the best behavior of k- ε and k- ω combined. The model equation is:

$$\frac{\bar{D}\omega}{\bar{D}t} = \nabla \cdot \left(\frac{v_T}{\sigma_\omega} \nabla \omega \right) + C_{\omega 1} \frac{P\omega}{k} - C_{\omega 2} \omega^2 + \left(\frac{2v_T}{\sigma_\omega k} \nabla \omega \cdot \nabla k \right) f \quad (\text{C.23})$$

With f being a blending function: equal to zero when approaching the walls, and equal to unity far from walls.

CITED LITERATURE

- [1] Vant-Hull L. L., Izygon M. E. and Pitman C. L. (1993), "Results of a Heliostat Field: Receiver Analysis for Solar Two," Solar Engineering 1993, A. Kirkpatrick and W. Worek eds., ASME Book No. H00785, pp. 413-419.
- [2] Pacheco, J. E., Ed., "Final test and evaluation results from the Solar Two project," SAND2002-2010, January 2002.
- [3] Kolb G. J., (1993), "Development of a Control Algorithm for a Molten-Salt Solar Central Receiver in a Cylindrical Configuration," Solar Engineering 1992, Proceedings of the 1992 ASME JSES KSES International Solar Energy Conference, April 1992, Maui, HI.
- [4] Zanino R., Bonifetto R., Christian J. M., Ho C. K. and Savoldi Richard L., "Effects of RANS-Type turbulence models on the convective heat loss computed by CFD in the solar two power tower," *Energy Procedia*, vol. 49, pp. 569-578, 2014.
- [5] Incropera F. P., Foundations of heat transfer (6th edition), Singapore: Wiley, 2013.
- [6] Munson B. R., Okiishi T. H., Huebsch W. W. and Rothmayer A. P., Fluid Mechanics (7th edition), Singapore: Wiley, 2013.
- [7] Zdravkovich M. M., Flow Around Circular Cylinders Volume 1: Fundamentals, 1997.
- [8] Spalart, P. R. and Allmaras, S. R., "A One-Equation Turbulence Model for Aerodynamic Flows" AIAA Paper 92-0439, 1992.
- [9] (2016) CD-adapco, «User Guide -Star-CCM+ Versione 11.04».
- [10] [Online]. Available: https://www.sharcnet.ca/Software/Ansys/17.2/en-us/help/flu_th/flu_th_sec_turb_near_wall_overview.html. [Accessed 9/09/2016].
- [11] Mehta K. C., Ritchie D. L. and Oler W., "Wind drag coefficient for octagonal cylinders," by the department of civil engineering Texas TECH university, March 1990.
- [12] Siebers D. and Kraabel J., "Estimating convective energy losses from solar central receivers," SAND 84-8717, April 1984.
- [13] Achenbach E., "The effect of surface roughness on the heat transfer from a circular cylinder to the cross flow of air," *Int. J. Heat Mass Transfer*. 1997; 20:359-69.
- [14] Christian J. and Ho C., "CFD simulation and heat loss analysis of the solar two power tower receiver," *Proceedings of ASME 2012 6th International Conference on Energy Sustainability & 10th Fuel Cell Science, Engineering and Technology Conference (ESFuelCell2012), July 23-26, 2012, San Diego, CA, USA*.

CITED LITERATURE (continued)

- [15] Catalano P. and Wang M., "Numerical simulation of the flow around a circular cylinder at high Reynolds numbers," *Elsevier*, 2003.
- [16] Chen O. M. and Utnes T., "Numerical simulation of flow around a smooth circular cylinder at very high Reynolds numbers," *Elsevier*, 2009.
- [17] Yuce M. I. and Kareem D. A., "A Numerical Analysis of Fluid Flow Around Circular and Square Cylinders," *JOURNAL AWWA*, 2016.
- [18] Pope S. B., *Turbulent flows*, Cambridge University Press.
- [19] Wilcox D. C., *Turbulence Modeling for CFD*, 1998.
- [20] Menter F. R., "Two-Equation Eddy-Viscosity Turbulence Models for Engineering Applications," August 1994.
- [21] [Online]. Available: <http://s3platform.jrc.ec.europa.eu/concentrated-solar-power>. [Accessed 29/09/2016].
- [22] [Online]. Available: https://www.volker-quaschnig.de/fotos/psa/index_e.php. [Accessed 29/09/2016].
- [23] [Online]. Available: <http://www.wisions.net/technologyradar/technology/parabolic-trough-power-plant>. [Accessed 29/09/2016].
- [24] Häberle A., "Encyclopedia of Sustainability Science and Technology," pp 6031-6037, Springer New York.
- [25] [Online]. Available: <http://www.solaflect.com/solar-solutions/suspension-heliostat>. [Accessed 2/10/2016].
- [26] Schiel W., Hunt B. and Keck T., "Solar Thermal Power Plants For Central Or Distributed Electricity Generation," June 2004.
- [27] [Online]. Available: <http://www.aalborgcsp.dk/projects/concentrated-solar-power/solar-tower-receiver-for-csp-tower-in-turkey.aspx>. [Accessed 2/10/2016].
- [28] [Online]. Available: http://www.buch-der-synergie.de/c_neu_html/c_04_34_sonne_hochtemperatur_ofen_chemie.htm. [Accessed 2/10/2016].
- [29] [Online]. Available: <http://www.thefifthstate.com.au/columns/spinifex/the-transition-from-fossil-to-renewable-energy/75484>. [Accessed 3/10/2016].
- [30] [Online]. Available: <http://www.computerworld.com/article/3031659/sustainable-it/worlds-largest-solar-plant-goes-live-will-provide-power-for-11m-people.html>. [Accessed 3 October 2016].
- [31] Kolb G. J., "Suction-recirculation device for stabilizing particle flows within a solar powered solid particle receiver," 7 feb 2012.

CITED LITERATURE (continued)

- [32] Zheng Z.-J., Li M.-J. and He Y.-L., "Optimization of Porous Insert Configuration in a Central Receiver Tube for Heat Transfer Enhancement," *Energy Procedia*, Aug 2015.
- [33] Fork D. K., Fitch J., Ziaei S. and Jetter R. I., "Life Estimation of Pressurized-Air Solar-Thermal Receiver Tubes," *J. Sol. Energy Eng*, October 19, 2012.
- [34] [Online]. Available: http://www.dlr.de/sf/en/desktopdefault.aspx/tabid-10693/18599_read-43284/. [Accessed 5/10/2016].
- [35] Blevins R. D., *Flow Induced Vibration*, 2nd Edn., Van Nostrand Reinhold Co., 1990.
- [36] T Walker., Xue S.-C. and Barton G. W., "Numerical Determination of Radiative View Factors Using Ray Tracing," *J. Heat Transfer*, April 28, 2010.
- [37] [Online]. Available: <http://nothingnerdy.wikispaces.com/THE+NATURE+OF+EM+WAVES+AND+LIGHT+SOURCES>. [Accessed 8/11/2016].

Curriculum vitae

PERSONAL INFORMATION Simone Pastura



📍 Corso Lione, 24, 10141 Torino (Italy)

☎ (+39) 3880597451

✉ simone_pastura@hotmail.it

💬 Skype simone.pastura

Sex Male | Date of birth 29/01/1994 | Nationality Italian

WORK EXPERIENCE

16/10/2017–Present

Manufacturing Engineer Intern

AvioAero (a GE Aviation business), Rivalta di Torino (Italy)

Rotating components: focus on the shrouds production cell of GENx-1B and 2B and GE 9x Low-Pressure Turbines.

02/11/2016–05/05/2017 Research Assistant at University of Illinois at Chicago

Modeling and simulation of wake vortex interaction in UAV swarm:

- conduct literature survey of current UAVs and their technical specifications. Study the wake interaction of a pair of UAVs and tests of analytical and semi-empirical models;
- results' post-processing by Matlab, with final estimation of separation distance for wake safety.

03/11/2014–16/03/2015 Math tutor

"A. Peyron - Re Umberto I" mid-grade school, Torino (Italy)

- daily teaching activity to groups of 10-12 student, filling mathematical gaps and strengthening related competences. Interact with the respective teachers, giving a feedback by brief summaries and marks.

01/10/2014–31/07/2016 Boarding school delegate

Collegio Universitario R. Einaudi, Torino (Italy)

03/2015–07/2015 Keeper assistant

Collegio Universitario R. Einaudi, Torino (Italy)

EDUCATION AND TRAINING

01/2016–12/2017 Master of Science in Mechanical Engineering, GPA: 4/4

University of Illinois at Chicago, Chicago (United States)

- Thesis: "CFD Modeling of the Solar Two Central Tower System Receiver"

07/2015–07/2017 Master of Science in Energy and Nuclear Engineering, final degree mark: 110/110

Politecnico di Torino, Torino (Italy)

- Thesis: "CFD Modeling of the Solar Two Central Tower System Receiver"

07/2012–07/2015 Bachelor degree in Energy Engineering, final degree mark: 104/110

Politecnico di Torino, Torino (Italy)

- Thesis: "Analisi delle modalità d'incentivazione economica per interventi impiantistici di miglioramento dell'efficienza energetica"

2007–2012 **Scientific high school diploma , final diploma mark: 100/100**

Liceo Scientifico O.M. Corbino, Siracusa (Italy)

PERSONAL SKILLS

Mother tongue(s) Italian

Other language(s)

	UNDERSTANDING		SPEAKING		WRITING
	Listening	Reading	Spoken interaction	Spoken production	
English	C1	B2	C1	C1	B2
Diploma in English language (FCE Cambridge, IELTS 6.5) B2 1 year spent in Chicago					
Levels: A1 and A2: Basic user - B1 and B2: Independent user - C1 and C2: Proficient user <u>Common European Framework of Reference for Languages</u>					

Communication skills **Mediation and interculturalism:** skills acquired working in a global dimension such as being math tutor with childs from different parts of the world, or such as being delegate of students from different parts of the world, and list their complaints and mediate between them and the management committee. My 10-months stay in Chicago contributed too.

Organisational / managerial skills - **Team work and leadership:** abilities acquired during work experiences like being the boarding school delegate, or during various academic projects. Needed collaboration between different figures;
 - **Autonomy and reliability:** abilities acquired during work experiences like being a Research Assistant at the UIC, or during various academic projects. A well defined work plan and method was required to obtain reliable results within a deadline;
 - **Flexibility and adaptivity:** abilities acquired during work experiences or academic projects, keeping calm in the face of difficulties, dealing with changing priorities/workloads and anticipating/responding positively to changing environments.

Digital skills

SELF-ASSESSMENT				
Information processing	Communication	Content creation	Safety	Problem solving
Independent user	Independent user	Basic user	Independent user	Independent user

Digital skills - Self-assessment grid

Programming languages known: C++, Matlab

Software applications: SolidWorks, FreeFem++, STAR-CCM+, Comsol, Aspen, Polysun

Other skills

- Enjoy sports like swimming, football, parkour and adrenaline experiences such as parachuting and bunjee jumping. Play transverse flute and cajon;
 - Love to travel and experience different cultures, fascinated by nature. Member of the ACI (Azione Cattolica Italiana).

Driving licence AM, A1, B

ADDITIONAL INFORMATION

Certifications "LEED Green Associate" (released by U.S. Green Building Council, on March 2017)

Processing of personal data In compliance with the Italian legislative Decree no. 196 dated 30/06/2003, I hereby authorize you to use and process my personal details contained in this document.